

# MRI-BASED STRAIN MAPPING FOR CARTILAGE REPAIR ASSESSMENT

**Sameer Sajid**

Submitted in Partial Fulfillment of the Requirements  
for the Degree of

*MASTER OF SCIENCE*

Approved by:

David Corr, Ph.D., Committee Chair  
Deva Chan, Ph.D.  
Qun Wan, Ph.D.



*Department of Biomedical Engineering*  
Rensselaer Polytechnic Institute  
Troy, New York

[May 2021]  
Submitted April 2021

© Copyright 2021

By  
Sameer Sajid

All Rights Reserved

# TABLE OF CONTENTS

LIST OF TABLES .....	vi
LIST OF FIGURES .....	vii
ACKNOWLEDGEMENTS .....	xii
ABSTRACT .....	xiii
1. INTRODUCTION .....	1
1.1 Knee Articular Cartilage .....	1
1.1.1 Zonal Structure and Mechanical Properties .....	2
1.1.2 Cartilage Depth-Dependency & Mechanical Response.....	3
1.2 Articular Cartilage Pathology.....	5
1.2.1 Matrix Damage .....	5
1.3 Cartilage Pathology Treatment.....	8
1.3.1 Clinical Treatment .....	8
1.3.2 Tissue Engineering Approaches .....	8
1.4 Cartilage Repair Imaging & Assessment .....	9
1.4.1 Repair Criteria.....	9
1.4.2 Clinical Repair Assessment .....	10
1.4.3 Tissue Engineering Repair Assessment .....	11
2. PROBLEM STATEMENT AND SPECIFIC AIMS .....	15
2.1 Specific Aim 1.....	15
2.1.1 Specific Aim 1A .....	15
2.1.2 Specific Aim 1B.....	15
2.2 Specific Aim 2.....	15
2.2.1 Specific Aim 2A .....	15
2.2.2 Specific Aim 2B.....	16
3. SPECIFIC AIM 1 .....	17
3.1 Aim 1A – Viscoelastic Parameter Estimation.....	17
3.1.1 Rationale .....	17
3.1.2 Cartilage Explantation .....	17
3.1.3 Sample Preparation .....	18
3.1.4 Cyclic Loading Device .....	19
3.1.5 Multi Frame Imaging & Signal to Noise Ratio Measurement.....	19
3.1.6 Viscoelastic Modeling .....	22
3.1.7 Monte Carlo Simulations .....	22
3.1.8 Aim 1A Discussion .....	25
3.2 Aim 1B – Spatial Strain Distribution Analysis .....	26
3.2.1 Rationale .....	26
3.2.2 Agarose Phantoms .....	27

3.2.1	Strain Analysis .....	28
3.2.2	Results .....	30
3.2.3	Aim 1B Discussion .....	32
4.	SPECIFIC AIM 2 .....	34
4.1	Aim 2A Methods .....	35
4.1.1	Spatial Analysis of Strains .....	35
4.1.2	Finite Element Model .....	37
4.1.3	Data Processing .....	40
4.1.4	Data Analysis .....	40
4.2	Aim 2A Results .....	43
4.2.1	Displacements .....	43
4.2.2	Strain Mapping .....	44
4.2.3	Spatial Analysis .....	46
4.2.4	Correlation and Plots .....	51
4.3	Aim 2A Discussion .....	55
4.4	Aim 2B Methods .....	57
4.4.1	Rationale .....	57
4.4.2	Finite Element Models .....	58
4.4.3	2D Slice Interpolation and Strain Calculation .....	62
4.4.4	Spatial Analysis of Data .....	63
4.5	Aim 2B Results .....	66
4.5.1	Displacements .....	66
4.5.2	Strain Mapping of Repair Scenarios .....	71
4.5.3	Correlation of Strain Maps and Spatial Analysis .....	77
4.6	Aim 2B Discussion .....	85
5.	DISCUSSION .....	88
5.1	Limitations and Shortcomings .....	88
5.2	Improvements and Potential Directions .....	89
5.3	Significance and Impact .....	91
5.3.1	Study Significance .....	91
5.3.2	Tissue Engineering Impact .....	91
5.4	Future Work .....	92
5.4.1	Phantom & Repair Model Validation .....	92
5.4.2	Spatiotemporal Strain Analysis of Cartilage Repair .....	92
6.	CONCLUSION .....	94
	REFERENCES .....	96
	APPENDICES .....	105
	Appendix A Process Verification .....	105
	Appendix B Supplemental Files .....	115
	B.1 Permissions for Section 1.1 .....	115

B.2	Permissions for Section 1.1.1 .....	115
B.3	Permissions for Section 1.2.1 .....	115

## LIST OF TABLES

Table 1: Scan results, average SNR per frame. SNR was computed as the mean of the ROI divided by the standard deviation of the noise.....	21
Table 2: Sensitivity and specificity of statistical tests in evaluating depth-dependent material properties. Statistically significant results were compared to a logical map of known differences in agarose concentration.....	32
Table 3: Literature value ranges for damaged and healthy cartilage (Kleemann et al., 2005; Little, Bawolin, & Chen, 2011; Mow & Guo, 2002) , Values considered for healthy, healthy properties are bolded.....	39
Table 4: Young’s modulus and Poisson’s ratio for each model. The model with healthy-level parameters is bolded.....	39
Table 5: Pearson's correlation values for the mean ratio of each analysis method VS the stiffness ratio. Strong correlations are in bold green and red colors, for positive and negative correlations respectively. Color intensity fades with decreasing correlation strength. Values between below -0.50 and above 0.50 were considered strongly correlated. Values with absolute value 0.95 or greater were considered nearly perfectly correlated.....	51
Table 6: Optimal models as determined by the mean ratio-stiffness ratio curve. The optimal model along the curve yielded the value closest to 1, or a minimum/maximum. Each mean ratio’s ability to assess stiffness ratio was evaluated through the proximity of the optimal model to 100% and the degree of correlation/curve shape. If value met one of these criteria, it was highlighted orange. If it met both, it was highlighted blue.....	55
Table 7: Parameters varied within repair tissue for FE model. Bolded values are considered healthy-level.....	62
Table 8: Pearson's correlation values for each strain type and spatial analysis heuristic VS stiffness ratio. Strong correlations are in bold orange and blue for negative and positive correlation, respectively. Color intensity fades with weaker correlation. Strong correlations were considered below -0.50 and above 0.50. Near perfect correlations were considered below -0.95 and above 0.95.....	78
Table 9: Pearson's correlation values for each strain type and spatial analysis heuristic VS maximum traction.....	78
Table 10: The best evaluators of stiffness ratio highlighted in blue. The optimal model based on each curve was determined through a match with the intact model. If that optimal model was close to 100%, the true optimal repair case, and yielded a near-perfect linear correlation, then it was considered a successful evaluator. Methods meetings the first criteria but not the second are highlighted orange.....	84

## LIST OF FIGURES

Figure 1: Diagram of the knee. Sagittal and coronal cross-sections are shown through the center of the joint. Cartilage covers the femoral condyles and the tibial plateau. Modified and reprinted under Shutterstock standard license..... 2

Figure 2: Full depth cross-section of articular cartilage showing the zonal depth-dependent structure. The left side shows the relative distribution of cells, while the right shows the orientation of the collagen fibers. Reprinted from (Buckwalter et al., 1994) with permission from Wolters Kluwer Health, Inc. .... 3

Figure 3: Progressive cartilage matrix damage for OARSI grades 1-5. Diagram on the left shows an idealized example of the damage, which starts with surface disruption, before proceeding through the depth of the tissue. Right shows histological examples, stained with Safranin O and Alcian Blue, demonstrating proteoglycan loss and matrix disruption. Reprinted from (Pritzker et al., 2006) with permission from Elsevier. .... 7

Figure 4: Cartilage explantation locations. Explants were 8mm in diameter, and cut down to 4mm height. .... 18

Figure 5: Sample holder layout with cartilage explant installed. Loading was applied with a flat tip indenter in the direction of the arrow. .... 19

Figure 6: The synchronization of the loading device with the multi-frame image acquisition and displacement encoding. Displacement encoding was applied before the load, and frames were acquired after a mixing time of 150ms. .... 20

Figure 7: Loaded FISP image with highlighted regions for ROI mask and noise mask. .... 21

Figure 8: Parameter estimation for  $c$ , intensity constant. Convergence was observed at 60dB, or  $1 \times 10^6$ . .... 23

Figure 9: Parameter estimation for relaxation constant  $\tau_1$ . Convergence was observed at 65dB or  $3.162 \times 10^6$ . .... 24

Figure 10: Parameter estimation for relaxation  $\tau_2$ . Convergence was observed at 70dB or  $1 \times 10^7$ . .... 25

Figure 11: Arrangement and naming scheme for the agarose phantoms..... 28

Figure 12: Representative process, using uniform 2% gel. Smoothed displacements are used to compute principal strains, which are divide into deformed grids for analysis. Each cell in the grid for a given phantom was compared to that cell of every other phantom..... 30

Figure 13: Kolmogorov-Smirnov analysis shown for uniform 2% VS uniform 4%. Strain distribution analysis showed 6 cells that were statistically significant, highlighted in red. Colored grid corresponds to p-values for comparison. Statistically significant cells are at the bottom of the scale and are colored dark blue. .... 31

Figure 14: Mann-Whitney U analysis shown for EP1 of uniform 2% VS uniform 4%. Mean analysis shows 13 statistically significant cells, highlighted in red. Colored grid corresponds to p-values for comparison. ....	31
Figure 15: Model layout, showing position of the inclusion (blue) relative to the healthy tissue (lime green). Assumptions of half-symmetry are made, and the model is cut in half. The left side of the model is the center of the tissue, the inner edge, while the right is the outer edge. The indenter (purple) indents the tissue on the articulating surface of the modeled explant. All dimensions are in millimeters. ....	38
Figure 16: Fully loaded models. The inclusion (blue), varied in stiffness ratio, ranging from 30% of healthy stiffness (softest), 100% (matching healthy), and up to 150% (above healthy). ....	40
Figure 17: Displacement treatment process shown with transverse (left) and axial (right) displacements from the 100% stiffness model. Interpolated displacements are injected with noise, and then smoothed. Displacements are in millimeters. ....	42
Figure 18: FE model mask, shown for the 100% stiffness ratio model. The light grey in the center denotes the inclusion, while the dark grey is the healthy tissue. Dotted white lines indicate the ROIs. The first ROI covers the inclusion (inner dotted line) while the second ROI (outer dotted line) is the bordering region. Analysis was performed on the ratio of the means from each ROI, termed the mean ratio. ....	43
Figure 19: Transverse (A) and axial (B) displacements of representative models. Displacements are in millimeters. Analysis ROIs are shown. The inner dotted line covers the inclusion, the outer covers 5 pixels of the surrounding tissue. ....	44
Figure 20: $E_1$ of representative models. Analysis ROIs are shown. The inner dotted line covers the inclusion, the outer covers 5 pixels of the surrounding tissue. ....	45
Figure 21: $E_2$ of representative models. Analysis ROIs are shown. The inner dotted line covers the inclusion, the outer covers 5 pixels of the surrounding tissue. ....	45
Figure 22: Maximum shear of representative models. Analysis ROIs are shown. The inner dotted line covers the inclusion, the outer covers 5 pixels of the surrounding tissue. ....	46
Figure 23: VMR maps of all strains, for representative models. Analysis ROIs are shown. The inner dotted line covers the inclusion, the outer covers 5 pixels of the surrounding tissue. ....	47
Figure 24: Lacunarity analysis for all strains, for representative models. Analysis ROIs are shown. The inner dotted line covers the inclusion, the outer covers 5 pixels of the surrounding tissue. ....	48
Figure 25: Moran's I of all strains, for representative models. Analysis ROIs are shown. The inner dotted line covers the inclusion, the outer covers 5 pixels of the surrounding tissue. ....	49

Figure 26: Gradient mapping of all strains, for representative models. The outer 3 pixels were excluded from gradient analysis to avoid edge bias. Analysis ROIs are shown. The inner dotted line covers the inclusion, the outer covers 5 pixels of the surrounding tissue..... 50

Figure 27: E1 mean ratio plots for all analysis methods..... 52

Figure 28: E2 mean ratio plots for all analysis methods..... 53

Figure 29: Maximum shear mean ratio plots for all analysis methods. .... 54

Figure 30: Model remeshing, smoothing, and defect insertion. (A) The raw, unsmoothed geometry imported from (Rodriguez-Vila et al., 2017). (B) The remeshed and smoothed model. (C) The same model as (B) but with a full-depth defect..... 59

Figure 31: (A) The patient-based FE model layout. A thin rigid body (lime green) models the femur, which applies load to the femoral and tibial cartilage (purple). (B) Positioning of 9 slices, done medial to lateral direction, relative to the defect. (C) Coronal slice of the model through the repair tissue center, shown as example only. (D) Zoomed-in sagittal slice, corresponding to slice #5 from (B). Tissue inclusion (blue) is centered at point of contact between healthy femoral and tibial tissue (purple). Slice interpolation was performed for entire combined femoral and tibial areas, but analysis was performed only within the indicated ROI..... 60

Figure 32: Interpolation of FE model. Repair cartilage is white, femoral cartilage is light grey, and tibial cartilage is dark grey. Analysis region was scaled down from full image, and is shown in the highlighted area..... 63

Figure 33: Displacement processing. Interpolated displacements are injected with noise,  $\sigma = 0.0061\text{mm}$  (Figure A.7), and then smoothed. Representative transverse and axial displacements are shown on 100%-10MPa and Intact models..... 64

Figure 34: Masks and analysis ROIs shown for all slices of representative models. ROI comprises the region encompassed by white dotted lines, which overlaps the boundary between the repair cartilage (light grey) and healthy femoral cartilage (medium grey). Left column shows the 100% stiffness ratio-1000MPa model. Middle column shows the intact model, overlaid with the same ROI. Right column shows the intact model again, but overlaid with repair tissue from the 100%-1000MPa model and the same ROI. Invalid points resulting from this approximation were excluded from analysis. .... 65

Figure 35: Representative transverse displacement maps of the stiffness ratio, all slices. Transverse displacements were concentrated along the healthy-repair interface (dotted black line) and increased with stiffness ratio. .... 68

Figure 36: Representative axial displacement maps of the stiffness ratio, all slices. Axial displacements were concentrated on the point of contact between the femoral and tibial tissue, and decreased with stiffness ratio. Interface is shown as a dotted black line. .... 69

Figure 37: Representative transverse displacement maps of maximum traction, all slices. No changes were observed across the model range. Interface is shown as a dotted black line.....	70
Figure 38: Representative axial displacement maps of maximum traction, all slices. No changes were observed across the model range. Interface is shown as a dotted black line.....	71
Figure 39: $E_1$ of representative stiffness ratio models, all slices. Repair interface is shown as a dotted white line.....	72
Figure 40: $E_2$ of representative stiffness ratio models, all slices. Repair interface is shown as a dotted black line.....	73
Figure 41: Maximum shear strains of representative stiffness ratio models, all slices. Repair interface is shown as a dotted white line.....	74
Figure 42: $E_1$ of representative traction models, all slices. Repair interface is shown as a dotted white line.....	75
Figure 43: $E_2$ of representative traction models, all slices. Repair interface is shown as a dotted white line.....	76
Figure 44: Maximum shear strains for representative traction models, all slices. Repair interface is shown as a dotted white line. ....	77
Figure 45: Plot of stiffness ratio against $E_1$ mean heuristic values.....	79
Figure 46: Plot of stiffness ratio against $E_2$ mean heuristic values.....	80
Figure 47: Plot of stiffness ratio against maximum shear heuristic values.....	81
Figure 48: Logarithmic plot of maximum traction against $E_1$ heuristic values. ....	82
Figure 49: Logarithmic plot of maximum traction against $E_2$ heuristic values. ....	83
Figure 50: Logarithmic plot of maximum traction against maximum shear heuristic values. ....	84
Figure A.1: Isometric view of the MRI-safe cyclic loading device. The entire device bolts to the front of an MRI scanner through the aluminum frame. The plastic components extend into the magnet where a sample holder lies at isocenter. ....	105
Figure A.2: Top view of the cyclic loading device. The location of the LVDT and accessories is shown, and were used during system validation. The load from the device is applied from an indenting rod, which extends through the hollow support tube, and applies a compressive load to a sample inside the sample holder.....	106
Figure A.3: System controls. The NI DAQ and VI control the entire system through the pressure regulator, relays for the pneumatic valves, and the trigger box for the MRI system. ..	106

Figure A.4: Virtual instrument (VI) used to operate the system. The VI controls the loading cycles through the four parameters on the left side- "Start Extension", "Extension Duration", "Retraction Delay", "Retraction Duration". The applied load is controlled through the "Regulator Set Pressure" parameter. The remaining controls and readouts are used for data logging and ensuring the system is working correctly..... 107

Figure A.5: Loading plateau average movement, cycle-to-cycle variation over 384 loading cycles. System movement was within one-half pixel width (50 $\mu$ m), the acceptable limit of movement..... 108

Figure A.6: Pressure-load linearity diagram for the cyclic loading device. Confidence intervals of the applied force during the load plateaus were computed, and shown to be within the permissible range with an excellent fit for linearity. .... 109

Figure A.7: Principal strains computed for the Sylgard 527 phantom using 50 cycles of a 5x5 Gaussian filter. Parts of the phantom surface were not analyzed due to pockets of air creating signal voids, hence the irregular shape. Phantom scans were repeated 9 times. Unsmoothed displacement data was used to analyze scanner noise. Pooled standard deviation of the noise equaled 0.0061mm, and was used to inject noise into simulated displacement maps. .... 109

Figure A.8: Idealized Green-Lagrange strains for simulated data, for a 256x256 pixel image. Data shown are true strains. .... 110

Figure A.9: Precision and bias of 64-pixel image. Precision and bias strain were for displacements and strains using simulated displacement maps injected with Gaussian noise through 100 Monte Carlo iterations (Deva D. Chan, Toribio, & Neu). Standard deviation was 0mm for perfect strain maps (no added noise), and 0.0061mm for simulated scanner noise (Figure A.7). Minimum bias for the noisy image was observed at 10 cycles for displacements, but 20 cycles for strains..... 111

Figure A.10: Precision and bias of 128-pixel images. Minimum bias of the noisy image was observed at 20 cycles for displacements and 50 cycles for strains..... 112

Figure A.11: Precision and bias of the 256-pixel images. Minimum displacement bias of the noisy image was at 50 cycles for displacements, with no clear minimum for strain..... 113

Figure A.12: Precision and bias of the 256-pixel images, extended up to 1000 smoothing cycles. Minimum bias of the noisy image was at 50 cycles for displacements, and 200 cycles for strains. 200 smoothing cycles will smooth the pixel impulse response across the entire ROI. While this minimizes overall strain, it may over smooth important features where local bias is more important. Thus, we limit smoothing for 256x256 images to 50 cycles..... 114

## ACKNOWLEDGEMENTS

I acknowledge my sugar and tea addictions in their respective contributions to this thesis and the ensuing lifelong habits. Through their grace, I have avoided the dark path of the coffee drinker.

This project would not have been possible without the patience and guidance of my advisor, Dr Deva Chan.

My close friends have all been thoughtful and kind, and always willing to listen. They have all helped me in their own ways and have been a part of my journey.

I also acknowledge my family for their unconditional love and support, and continued encouragement even in the bleakest moments. I am eternally grateful.

Finally, I would like to thank my partner, Brittany, for her calming presence and companionship. The last two years would have been impossible without her. I look forward to spending a lifetime together.

Now, where the *devil* are my slippers?

## ABSTRACT

Current cartilage repair strategies fall short of therapeutic repair due to a lack of true tissue integration. As cutting-edge tissue engineering (TE) approaches advance toward recapitulation of the depth-dependent healthy tissue structure, repair assessment methods have not kept pace. Most *in vitro* TE studies employ destructive, singleton measurements that ignore spatially-dependent mechanical information, or they examine through-thickness mechanics by altering boundary conditions. Clinical research employs *in vivo* qualitative morphological assessment that ignores mechanical function entirely. There is a need for non-destructive, full-depth assessment of tissue mechanics.

MRI is the current gold standard for assessing cartilage repair *in vivo* due to excellent tissue contrast and ability to visualize tissue morphology. MRI-based strain mapping can visualize changes associated with cartilage tissue defects and has been performed *in vivo*. However, the ability of MRI-based strains to evaluate cartilage repair has not been assessed. This was done through four key features of cartilage repair; tissue viscoelasticity, depth-dependent material properties, repair stiffness match, and interface mechanics.

Here, I assessed the ability of MRI-based strain mapping in evaluating these features of cartilage repair. As TE methods move toward recapitulating tissue viscoelasticity, I attempted to fit full-depth tissue deformations to a quasi-linear viscoelastic model of cartilage; however, adequate fits required infeasible SNR and temporal resolution.

Previous studies have examined depth-wise strain distribution as a correlate for depth-dependent material properties. I analyzed the strain distribution of MRI-based strain maps from depth-dependent agarose phantoms, from previously published work. While the strain

distribution was more specific than mean strain in detecting differences in agarose concentration, it proved less sensitive. Thus, MRI-based mean strains were considered for the remaining work.

Successful cartilage repair must feature a close match of material properties. While tissue viscoelasticity match represents the ideal repair scenario, many TE studies focus their effects on recapitulating Young's modulus first. I built a finite element (FE) of cartilage tissue featuring an inclusion of altered stiffness. I then synthesized MRI imaging-derived displacement maps using the model to simulate MRI-based strain mapping. I also analyzed strain map topography through texture-based spatial analysis techniques. I found that the mean ratio of the compressive strains of the inclusion versus the surrounding tissue strain was nearly perfectly correlated with the change in stiffness, with some correlation with spatial analyses heuristics. Additionally, MRI-based strains qualitatively visualized the regions of altered stiffness.

Finally, I also assessed interface mechanics in a patient-based FE model of knee cartilage. I created a defect in the femoral tissue and filled it with repair tissue of varying material properties and interface strength. I examined the effects of the material stiffness and interface strength on the MRI-based strains and spatial analyses of the interface, compared to those of an intact model. I found that all strains were highly correlated with material stiffness match, but did not change at all based on interface strength.

I conclude that MRI-based strains should be considered for cartilage repair evaluation. The mean strains of both the interface and regions of altered material properties correlated with mechanical stiffness changes. As a result, MRI-based strain mapping has clear qualitative value in assessing relative mechanical property differences.

# 1. INTRODUCTION

This chapter introduces the anatomy and physiology of articular cartilage, common pathologies, and current strategies for cartilage repair. I also cover current methods for cartilage repair assessment and their weaknesses. This establishes the motivation for new repair assessment methods and their requirements.

## 1.1 Knee Articular Cartilage

Articular cartilage is an avascular, non-innervated, load-bearing tissue present in diarthrodial joints that allows for smooth articular motion(Fox, Bedi, & Rodeo, 2009). In the knee, this tissue covers the femoral condyles, trochlear groove, patella, and tibial plateau, and serves to distribute load and allows for smooth joint articulation (Figure 1).

Articular cartilage has important characteristics that enhance joint mobility. The articulating surface has a very thin coat of a protein named lubricin, a type of proteoglycan (PG) that provides lubrication for the joint surface sliding against each other(Schumacher, Block, Schmid, Aydelotte, & Kuettner, 1994). To bear load, this cartilage has a specialized biochemical composition and structure. 70% of the tissue dry weight is made of type II collagen. This collagen forms a crosslinked, depth-dependent ultrastructure, vital to the cartilage, and will be discussed later. The remainder of the cartilage largely comprises a bottle-brush structure of negatively-charged glycosaminoglycans (or GAGs) such as chondroitin sulfate or keratin sulfate. These GAGs are all bound to a core protein to create a PG with a densely-packed structure called aggrecan(Roughley & Mort, 2014). The PGs are all connected to a hyaluronic acid (HA) backbone via link proteins, creating the bottle-brush structure. The GAGs within the PGs are negatively-charged, they attract water molecules. This causes the matrix to swell with water,

providing much of the instantaneous stiffness response. Chondrocytes are responsible for collagen and PG turnover and are distributed unevenly throughout the matrix(Fox et al., 2009).

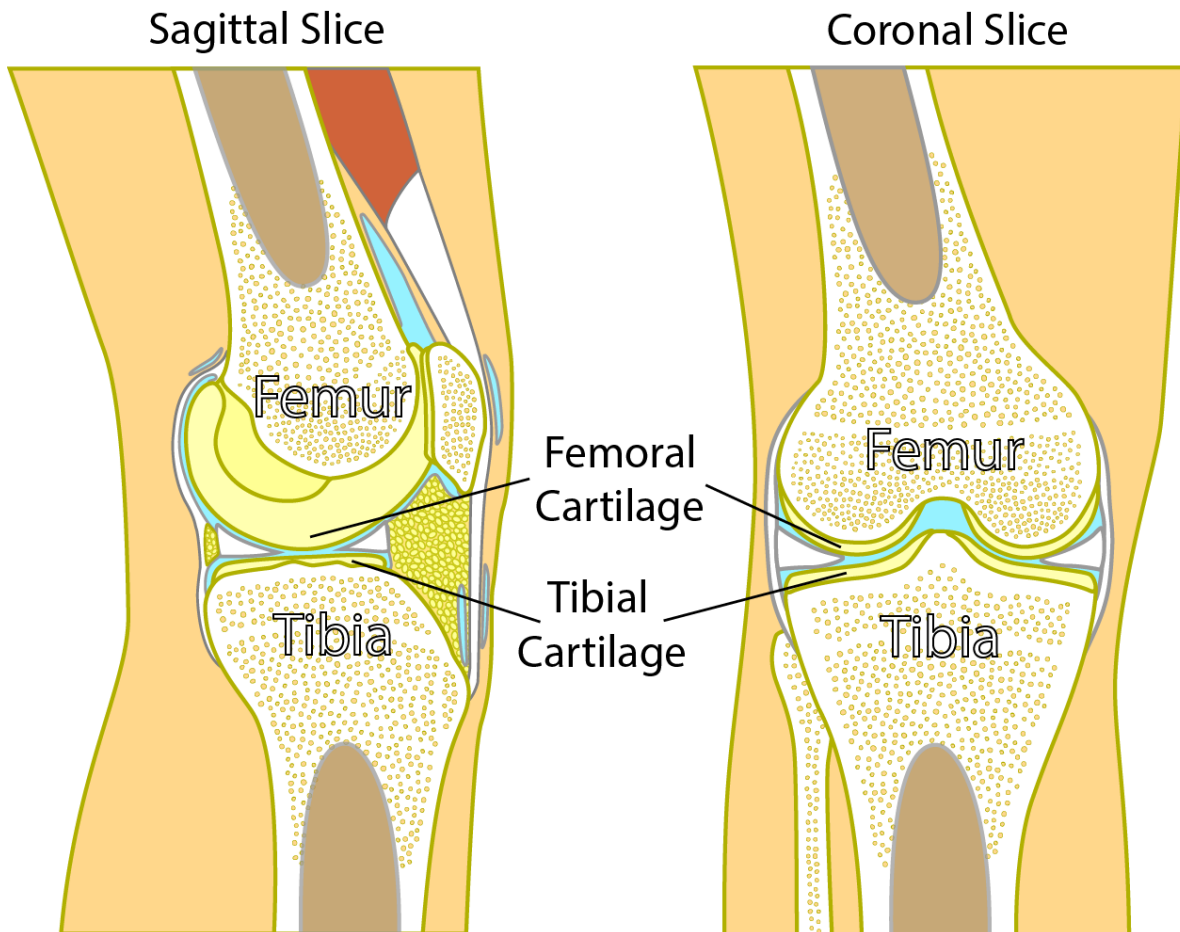


**Figure 1: Diagram of the knee. Sagittal and coronal cross-sections are shown through the center of the joint. Cartilage covers the femoral condyles and the tibial plateau. Modified and reprinted under Shutterstock standard license.**

### **1.1.1 Zonal Structure and Mechanical Properties**

Cartilage has a zonal structure by depth with three distinct layers (Figure 2)(Buckwalter, Mow, & Ratcliffe, 1994).

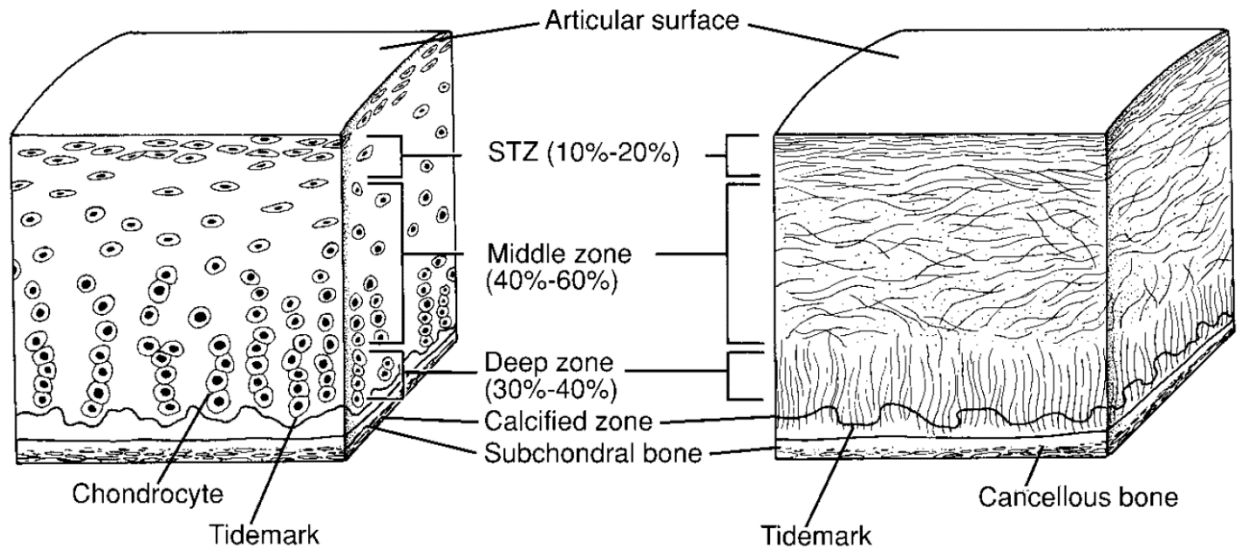


**Figure 2: Full depth cross-section of articular cartilage showing the zonal depth-dependent structure. The left side shows the relative distribution of cells, while the right shows the orientation of the collagen fibers. Reprinted from (Buckwalter et al., 1994) with permission from Wolters Kluwer Health, Inc.**

The first 10%-20 of tissue depth is considered the superficial zone (SZ). This area is characterized by heavily crosslinked, tangentially-oriented collagen fibers, with a low PG content but the highest density of chondrocytes. The majority of the tissue, roughly 40-60% by volume, is considered the middle zone (MZ). The MZ has an amorphous collagen ultrastructure with a high PG content. Chondrocytes are present in a uniform, low density within the MZ (Fox et al., 2009). The lowest layer of cartilage is the deep zone (DZ), which is the lowest 20-30% of the tissue. The DZ is hallmarked by vertically-aligned cartilage fibers perpendicular to the articulating surface, densely packed together. This region has the highest concentration of PGs per unit volume within cartilage is sparsely populated with cells. This region also features a calcified layer that is pivotal in anchoring the cartilage tissue to the subchondral bone beneath (Redler, Mow, Zimny, & Mansell, 1975).

### 1.1.2 Cartilage Depth-Dependency & Mechanical Response

Cartilage has a complex, depth-dependent response to loading. The water content of the tissue resists much of the initial compressive load on a timescale less than 50ms, resulting in an extremely high instantaneous stiffness(Oloyede, Flachsmann, & Broom, 1992). When exposed to cyclic physiological loading, the tissue experiences cumulative strain dependent on the collagen matrix(C. Y. Huang, Soltz, Kopacz, Mow, & Ateshian, 2003; Moger et al., 2009). As both the water content and collagen matrix ultrastructure vary by depth, material properties of the tissue vary similarly.

Within the SZ, the tangential structure of collagen ultrastructure and relatively low PG content results in low stiffness in compression, but strong tensile properties. This orientation of the collagen fibers coupled with the osmotic pressure creates these tensile properties. The degree of crosslinking within the SZ protects the tissue below from excessive shear strains, and its integrity is vital to preventing cascading matrix damage(Desrochers, Amrein, & Matyas, 2012; Rolauffs et al., 2010). The natural crimping of this heavily crosslinked, collagenated zone generates strain-dependent mechanical stiffness(Ahsanizadeh & Li, 2015). The SZ also has the overall lowest PG content as well as lowest concentration of PGs within the entire tissue depth, unlike the chondrocyte density(Fox et al., 2009). The integrity of the SZ has also been shown to control surface diffusion(DiDomenico & Bonassar, 2018), the degree of matrix swelling, as well as the time & strain-dependent stiffness response(Ahsanizadeh & Li, 2015; Rolauffs et al., 2010) of the tissue as a whole.

On the other hand, MZ and DZ comprise most of the cartilage by volume. The MZ has the highest water content, which is responsible for its initial resistance to compression. As a result, this region is responsible for most of the initial stiffness, especially before the loading

plateau(Antons et al., 2018). The DZ's combination of densely-packed, vertically-aligned fibers and high PG density result in very high compressive stiffness.

As a result of this heterogenous and zonal structure, cartilage experiences a complex, depth- and time-dependent response to loading(Griffin et al., 2014; Hayes & Bodine, 1978; C.-Y. Huang, Mow, & Ateshian, 2001; Mak, 1986). Compressive strains are highly concentrated in the SZ within the first 50-100 milliseconds of loading, but then propagate to the MZ. Relatively few strains are concentrated in the DZ under physiological loading when compared to the SZ or MZ(Erne et al., 2005). This differential strain concentration can be attributed to the differences in collagen ultrastructure, as well as the difference in PG content by depth. As the water initially resists compression, it is pushed through the matrix, shifting the load onto the solid material as the loading reaches a quasi-static equilibrium(Erne et al., 2005; Moger et al., 2009).

## **1.2 Articular Cartilage Pathology**

### **1.2.1 Matrix Damage**

Cartilage lacks a direct blood supply, instead exchanging nutrients and waste via diffusion through the articulating surface into the synovial fluid, and through the DZ into the subchondral bone. Although this mechanism permits some nutrient exchange, it is very slow, so the chondrocytes have a low metabolic rate compared to other cells(Ulrich-Vinther, Maloney, Schwarz, Rosier, & O'Keefe, 2003). This results in a relatively slow turnover of cartilage matrix, which is acceptable under normal physiological conditions. However, after injury such as physical trauma or persistent overexertion, the cartilage surface begins to degrade(Kim, Lee, & Kim, 2007; Rolaufts et al., 2010). Previous studies have reported reduced chondrocyte viability and matrix damage following mechanical overload *in vitro*(Jeffrey, Gregory, & Aspden, 1995). Mechanical overload is associated with the matrix damage, which leads to cascading matrix

collapse(Brown et al., 2012) and the release of matrix metalloproteinases proteinases and growth factors that ultimately degrade the tissue(Guan et al., 2015; Im et al., 2007). Such markers of inflammation have been found even without injury, from persistent overexertion such as marathon running(Kim et al., 2007). The net result is cascading matrix damage from a focal injury (Figure 3). Cartilage damage is typically concentrated on the central surfaces of the femoral and tibial condyles where contact stresses are highest- most often on the medial side(Karataglis, Green, & Learmonth, 2006). When this damage is coupled with chondrocytes' low metabolic rate, the cells cannot maintain the level of matrix deposition needed to turnover and create new tissue(van Haften, Ito, & van Donkelaar, 2017). Because the tissue lacks innervation, no pain is felt from this early degeneration, leaving few warning signs to a person suffering from low levels of cartilage damage. This damage often progresses to full-depth focal defects(Houck et al., 2018). Severe full-depth focal damage often leads to osteoarthritis (OA) within the joint(Houck et al., 2018; Spahn & Hofmann, 2014). For a review of the pathophysiological, psychological, or economic impacts of OA, the interested reader is directed to the following reviews, respectively(Mobasheri & Batt, 2016; Puig-Junoy & Ruiz Zamora, 2015; Willett et al., 2019). While OA still lacks curative treatment, focal repair options are available as stopgap measures until a joint replacement becomes absolutely necessary.

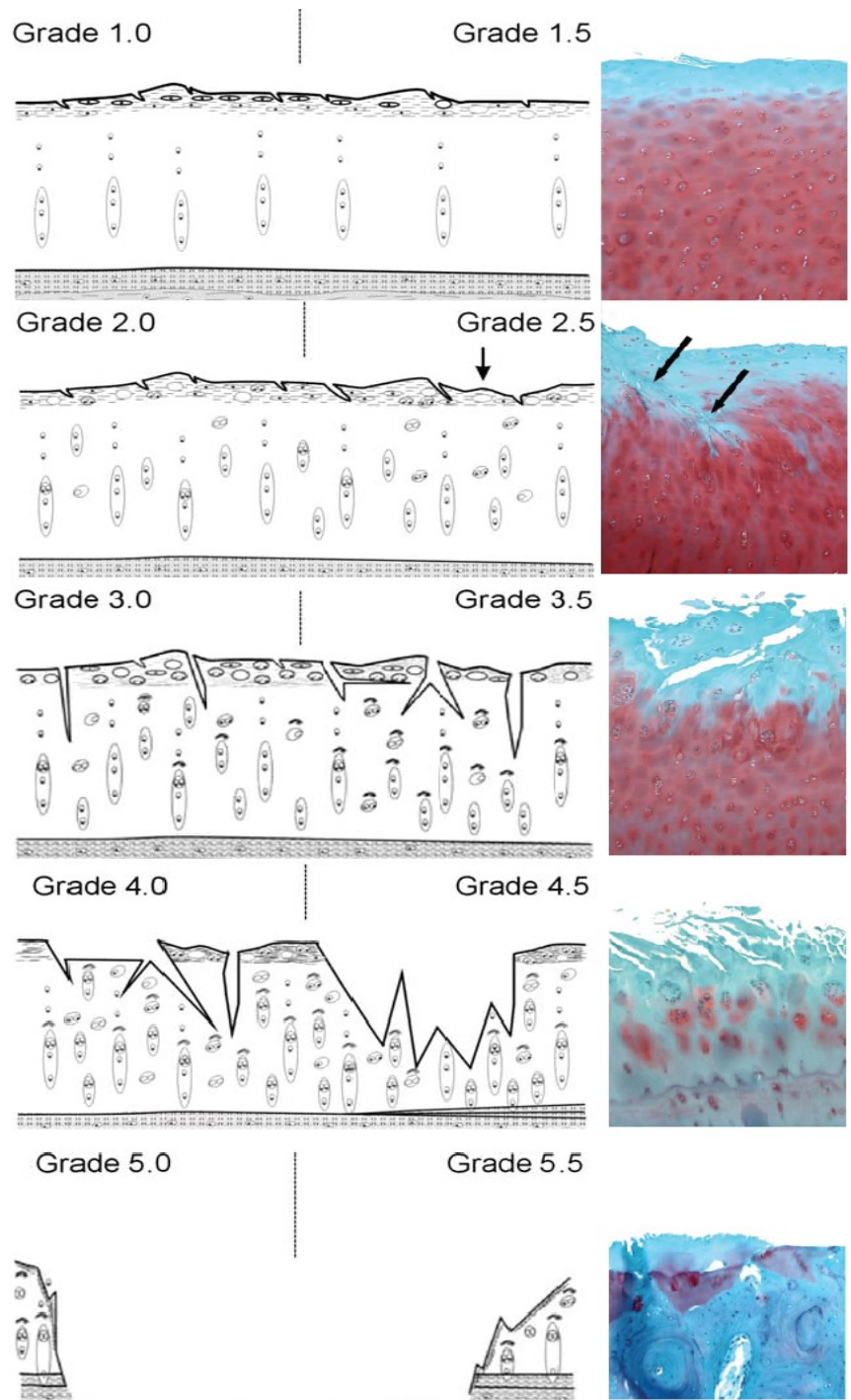


**Figure 3: Progressive cartilage matrix damage for OARSI grades 1-5. Diagram on the left shows an idealized example of the damage, which starts with surface disruption, before proceeding through the depth of the tissue. Right shows histological examples, stained with Safranin O and Alcian Blue, demonstrating proteoglycan loss and matrix disruption. Reprinted from (Pritzker et al., 2006) with permission from Elsevier.**

## **1.3 Cartilage Pathology Treatment**

### **1.3.1 Clinical Treatment**

OA is a whole joint disorder, and as such, has a complex set of causes that vary from patient to patient. Because of this, there is no curative treatment for OA as a whole. Fortunately, treatment options do exist for cartilage damage. Current clinical repair methods include simple cartilage replacement techniques that serve to fill in the defect area with substitute tissue. Older methods such as microfracture create isotropic fibrocartilage instead of organized hyaline tissue. Newer methods such as autologous chondrocyte implantation seed the defect site with a cultured mass of chondrocytes, covered by a layer of thin tissue(Crawford, DeBerardino, & Williams, 2012). Both of these repair methods are associated with similar, good patient-related outcomes(Ossendorff et al., 2019), but deterioration appears to be inevitable, resulting in a long-term decline(Gobbi, Karnatzikos, & Kumar, 2014). In either of these cases, the repair tissue is softer than healthy tissue(Milano et al., 2010; Vasara et al., 2005), and lacks its depth-dependent viscoelasticity. While these methods have been shown to be better than no treatment at all, they fundamentally lack the foundation for integrative, full-depth repair.

### **1.3.2 Tissue Engineering Approaches**

Many of the cutting-edge techniques being developed for focal cartilage repair involve a tissue engineering (TE)-based approach. Cells are grown and seeded onto a biomimetic scaffold, then treated with some combination of growth factors and mechanical stimulation to enhance the construct properties(Howard, Buttery, Shakesheff, & Roberts, 2008). This general approach shows excellent promise as a design philosophy as it allows for finer control over the proliferating cell type as well as the structure of the matrix. Furthermore, novel 3D printing methods allow for the creation of a cell-seeded, tissue scaffold that exhibits similar depth-

dependency to healthy tissue in terms of cellular density and tissue geometry(Ainola et al., 2015; Bracaglia et al., 2017). The addition of cyclic mechanical stimulation and growth hormones improve construct properties dramatically at the end of the culture time, matching or exceeding healthy stiffness while also showing clear signs of tissue integration(Theodoropoulos, DeCroos, Petrerá, Park, & Kandel, 2016). All these techniques show great promise in creating repair cartilage with matching mechanical properties, but as the field advances, equivalent progress in repair assessment has not been made.

## **1.4 Cartilage Repair Imaging & Assessment**

### **1.4.1 Repair Criteria**

Appropriate cartilage repair has several major criteria that must be considered for any given repair method. The first is the material's biomechanical behavior; its ability to sustain load. In order for a repair to be successful, it must have a matching ability to bear load to the surrounding healthy tissue. While it may be obvious why an excessively soft or stiff tissue cannot serve as an adequate replacement, it is less obvious why it must match in terms of both the depth-dependent viscoelastic response, and the time-dependent one. As the knee undergoes cyclic compression and shear through each phase of the gait, the tissue receives some amount of loading each cycle. Eventually, the tissue will reach a quasi-steady-state (QSS) and effectively form a loading plateau that experiences some amount of cumulative strain(Eckstein, Tieschky, Faber, Englmeier, & Reiser, 1999; Lad et al., 2016). Not only is it important for the repair tissue to match the total amount of cumulative strain, but also the same cumulative strain concentration by depth, as well as per cycle. If this depth-dependent and time-dependent viscoelastic behavior is not captured, excessive interface micromotions and shear strains can appear between the boundaries of the repair tissue at each loading cycle, ultimately preventing tissue integration.

The second criterion deals with the strength of the repair interface, mainly of the collagen ultrastructure. For the chondrocytes to deposit collagen II and physically connect the matrices of the repair and host tissue, several things must be true. There must be no gap present between the host or repair tissue. It is intuitive to see why a physical gap along the repair interface will prohibit linking of the collagen networks as the cells cannot physically join the two extracellular matrices. Additionally, the repair tissue must also have viable chondrocytes or stem cells expressing chondrocyte-like behavior. Without these cells, no collagen II deposition will occur, and thus no interface connection. Collagen deposition is directly correlated with interface strength, and the linking of the collagen ultrastructure is established as vital in the minimization of interface motion(Ahsan & Sah, 1999; Dimicco & Sah, 2001).

The third criterion is less to do with the choice of construct or repair type, but with the subchondral bone and fixation. For a stable repair, the repair tissue must adhere properly to the subchondral bone underneath. This is typically accomplished in the clinic with the use of bioglues or bone cement. Studies have shown that the fixation at the DZ is absolutely vital to the integrity of the repair, but repair methods in this area are reasonably well-established, and so this dissertation will focus on the first two criteria: stiffness match, and interface strength.

#### **1.4.2 Clinical Repair Assessment**

Current clinical standards for repair assessment revolve around medical imaging of the knee joint. By visually comparing the morphology of the repaired tissue to the surrounding healthy tissue, a qualitative assessment of the repair is made. The oldest assessment methods employ radiographs which have very poor contrast in soft tissue. Their lack of ability to visualize cartilage has traditionally been the source of serious critique (Guermazi et al., 2012) as they can only visualize joint space width for OA diagnosis(Kellgren & Lawrence, 1957).

Instead, current repair assessment methods examine tissue contrast and morphology using Magnetic Resonance Imaging (MRI). As MRI has excellent contrast in soft tissue and is sensitive to low-grade, pre-OA damage(Reichenbach et al., 2010), MRI-based scoring methods MOCART, MOAKS, and CROAKS have been created to semi-quantitatively grade cartilage health and repair(Hunter et al., 2011; Roemer et al., 2014; Welsch et al., 2011). These scores have proven to correlate with patient-related outcomes and act as good predictors of revision surgery needs within 5 years(Anderson et al., 2017). For more information on the details of semi-quantitative MRI-based cartilage repair scoring, the interested reader is directed to the following review(Hayashi et al., 2018). All three of these methods heavily rely on tissue morphology to assess repair.

Ultimately, clinical repair assessments prioritize patient-related outcomes over tissue mechanics. While patient-related outcomes are vital to appropriate patient care, they are beyond the scope of this work. As non-invasive, *in vivo* mechanical assessment is lacking within the medical field, there is a clear need to visualize tissue mechanics for cartilage repair.

### **1.4.3 Tissue Engineering Repair Assessment**

Tissue engineering (TE) *in vitro* approaches have more flexibility in repair assessment since destructive and invasive methods can be employed to quantify or visualize mechanical behavior. Mechanical testing methods are well-established ways of establishing tissue properties by observing the mechanical response. Among these methods, indentation tests are widest category and represent well-established methods(Olvera, Daly, & Kelly, 2015) that can measure aggregate modulus in confined compression, elastic (Young's) modulus in unconfined compression, shear modulus, Poisson's ratio, and dynamic modulus over any number of desired frequencies. These values are not comprehensive and the field for indentation testing continues

to evolve. However, these tests are destructive; biological samples are often damaged under repeated loading, and the tests require methods of tissue extraction and fixation that are final. Despite the continued importance of measuring material properties in TE constructs, indentation testing cannot be performed *in vivo*, which means reduced clinical translatability. Finally, most indentation tests cannot measure through-thickness behavior, only examining bulk properties. Measuring through-thickness behavior can be done *in vitro*, but often alters boundary conditions and is extremely laborious (Komeili, Abusara, Federico, & Herzog, 2018; Schinagl Robert, Gurskis, Chen Albert, & Sah Robert, 2005).

As cartilage repair seeks to provide curative therapy for focal cartilage damage, push-out strength tests are also popular to measure interface strength between the healthy tissue and the repaired tissue (Fisher et al., 2014; Theodoropoulos et al., 2016; Vinardell, Thorpe, Buckley, & Kelly, 2009). However, push-out tests share some problems with indentation testing; they are inherently destructive. Once again, this also prohibits *in vivo* application and makes longitudinal study far more expensive, with weaker clinical translatability. And again, there is the issue of visualizing through-thickness behavior. Push-out tests reduce measures of repair quality, which is a complex connection between the repair tissue and healthy tissue, to a singleton value.

Most forms of mechanical testing can only visualize surface or bulk properties, and lose depth-dependent information which is key for tissue repair. Purely mechanical approaches that seek to provide this information are extremely laborious and lose clinical relevance. Imaging methods can fill in the gaps by visualizing full-depth strains. Some imaging methods have *in vivo* application, and non-destructive visualization of tissue deformation, while not reducing interface information dimensionality.

Digital imaging correlation (DIC) is an established method that can visualize full-depth deformation and strain within tissues, with extremely high temporal and spatial resolution (Gilchrist, Witvoet-Braam, Guilak, & Setton, 2007). However, DIC setups require extensive preparation and fixation of the tissue, which is still destructive and alters boundary conditions. DIC also cannot be done *in vivo*, as it requires a controlled test setup with high-speed imaging.

On the other hand, optical coherence tomography (OCT) rectifies some of DIC problems by allowing for some *in vivo* application (Li et al., 2005; Nebelung et al., 2015; Simo, Shu-Zhe, Yan-Ping, & Yong-Ping, 2009). OCT provides extremely high spatial resolution, and visualization of through-thickness matrix properties, while also correlating with matrix constituents. As OCT's ability to penetrate into tissue is limited, it must be done with arthroscopic probes, which is invasive. However, OCT has also been used to evaluate articular cartilage damage and assess tissue repair. OCT can also examine optical properties of cartilage that correlate with tissue viscoelasticity. However, OCT has limited penetration depth and cannot visualize full-depth deformations in cartilage.

MRI is an established technique for *in vivo* and *in vitro* work that represents the gold standard for clinical cartilage repair assessment (Hunter et al., 2011; Roemer et al., 2014; Welsch et al., 2011). MRI possesses excellent soft tissue contrast, which allows for well-informed qualitative judgment of tissue morphology. MRI relaxometry such as T2 mapping (Welsch et al., 2011) and T1rho mapping (Welsch et al., 2011) correlate to matrix constituents. Additionally, motion-sensitive scans can visualize through-thickness cartilage mechanical behavior, *in vitro* and *in vivo* (Chan et al., 2016; Chan & Neu, 2012; Sajid & Chan, 2019).

Not all current assessment methods are sensitive to the important features of cartilage repair. Clinical methods focus on non-destructive, non-invasive visual qualitative assessments of tissue morphology and the repair interface based. Engineering approaches examine mechanical behavior, but often by reducing through-thickness data to a singleton measurement. There is a need for a quantitative, full-depth, biomechanical approach to cartilage repair. MRI is an already established method for visualizing cartilage repair, and has been employed *in vitro* and *in vivo* to visualize full-depth strains in cartilage. MRI-based strains are already used by clinicians in cardiology following tissue trauma, but rarely for musculoskeletal tissues, and not at all to assessing cartilage repair. Here, I propose the use of MRI-based strain maps as a quantitative measure of the quality of cartilage repair.

## **2. PROBLEM STATEMENT AND SPECIFIC AIMS**

A quantitative, full-depth, biomechanical approach to cartilage repair is needed. As current TE approaches advance towards full-depth recapitulation of the cartilage matrix, assessment methods must advance as well in order to properly assess potential repair strategies in terms of material property match and repair integration. The objective of this project is to assess the ability of MRI-based strain mapping in evaluating cartilage repair.

### **2.1 Specific Aim 1**

Assess whether MRI-based strain fields can be used to measure tissue viscoelasticity and depth-dependent changes in tissue mechanics.

#### **2.1.1 Specific Aim 1A**

Assess the ability of a multi-frame MRI acquisition in fitting viscoelasticity model constants.

#### **2.1.2 Specific Aim 1B**

Assess the ability of MRI-based strain distribution and mean strain in measuring depth-dependent mechanical property differences.

### **2.2 Specific Aim 2**

Assess the correlation between simulated MRI-based strain fields and material properties and interface strength.

#### **2.2.1 Specific Aim 2A**

Assess the correlation of MRI-based strains of an inclusion and the surrounding tissue with material stiffness match.

### **2.2.2 Specific Aim 2B**

Assess the correlation of MRI-based strains of a repair interface with material stiffness match and integration strength.

### **3. SPECIFIC AIM 1**

This chapter will cover the two sub-aims used to fulfill Aim 1. Aim 1A covers the fitting multi-frame MRI data to a viscoelastic model of cartilage. Aim 1B covers a semi-quantitative method to analyze strain maps acquired from depth-dependent phantoms.

#### **3.1 Aim 1A – Viscoelastic Parameter Estimation**

##### **3.1.1 Rationale**

Integrative cartilage repair requires a match of material properties(Ahsan & Sah, 1999; Wang et al., 2018). As cartilage is a viscoelastic material, it is important to recapitulate this time-dependent response within the repair tissue to minimize extraneous interface motion(Shapiro, Koide, & Glimcher, 1993). Cartilage viscoelasticity been described with models like quasi-linear viscoelasticity(Fung, 1993) (QLV) and fitted with indentation data (Tripathy & Berger, 2012). Indentation testing provides high temporal resolution, but can only obtain the deformation of the overall tissue through the displacement of the indenter. On the other hand, MRI can visualize through-thickness mechanics without altering boundary conditions(Neu, Hull, Walton, & Buonocore, 2005). Previous studies have observed some relationship between cartilage viscoelasticity and MRI data through diffusion-weighted and diffusion tensor imaging(Ferizi et al., 2017; Rodriguez-Vila, Sánchez-González, Oropesa, Gomez, & Pierce, 2017). Motion-sensitive MRI data has mapped strains *in vivo* without altering boundary conditions(Chan et al., 2016), but has not been fit to any viscoelastic models. Here, I examined if displacement maps produced from a multi-frame, motion-sensitive MRI sequence can be used to fit a QLV model of cartilage.

##### **3.1.2 Cartilage Explantation**

Cartilage explants were needed to assess SNR in tissue with a multi-frame acquisition. Week-old calf stifle joints were purchased from an abattoir (Research 87, Boylston, MA) and shipped overnight. Joints were dissected to extract 3 cartilage explants from the lateral-posterior side of femoral condyle from a single joint (Figure 4)(Butz, Chan, Nauman, & Neu).

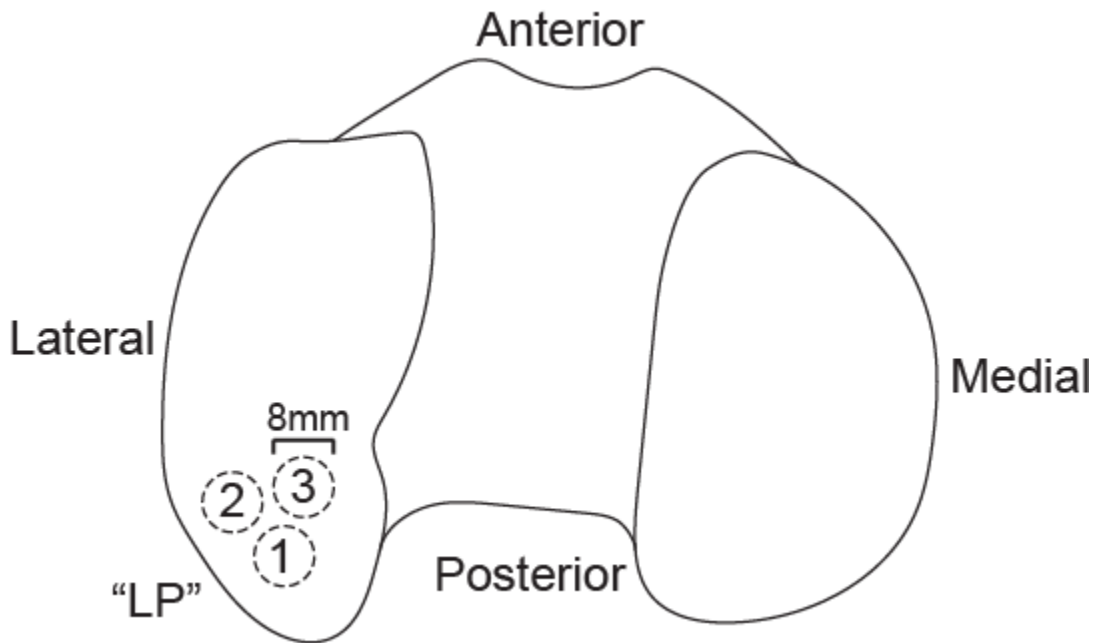


**Figure 4: Cartilage explantation locations. Explants were 8mm in diameter, and cut down to 4mm height.**

Explants were extracted using an 8mm diameter steel punch, and were cut 4mm from the articulating surface to create a flat base and constant height. Explants were stored at -20°C in 300mOsm PBS using airtight cryovials to preserve mechanical properties(Szarko, Muldrew, & Bertram, 2010).

### **3.1.3 Sample Preparation**

Explants were thawed inside cryovials to RT over 5.5 minutes in a 37C water bath. Explants were dabbed dry and bonded with cyanoacrylate to 3D printed sample platforms. A

divot in the center of the platform ensured the stability and central positioning of the explant. The explant and platform were put inside a watertight latex bag which was filled with 4mL of isotonic PBS. The platform and bag were inserted into a 3D printed sample holder (Figure 5).

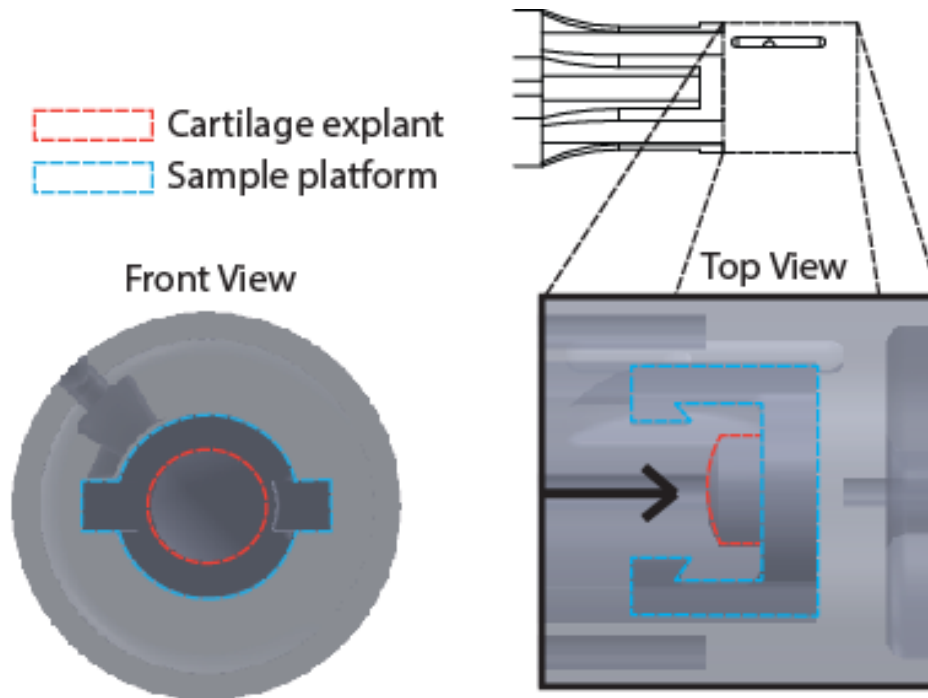


**Figure 5: Sample holder layout with cartilage explant installed. Loading was applied with a flat tip indenter in the direction of the arrow.**

### **3.1.4 Cyclic Loading Device**

I constructed an electropneumatic, MRI-safe, cyclic loading device based on previous efforts (Martin, Neu, & Hull, 2009; Neu & Hull, 2003) and verified its performance (Figure A.1- Figure A.6). The device was bolted to the front of a 7T Bruker Pharmascan system (Bruker Medical GMBH, Ettlingen, Germany) with the explanted cartilage and sample holder (Figure 5) placed at magnet isocenter.

### **3.1.5 Multi Frame Imaging & Signal to Noise Ratio Measurement**

The explants were loaded in synchrony with MRI imaging. Fast Imaging in Steady Processions (FISP) scans were performed with the following parameters: 128x128 pixels, 1mm thick coronal slice, TR/TE: 5/2.5ms, FA 35°, 1 average, 1 repetition, 4 segments, and  $\alpha/2$  starter sequence with 8 dummy scans. The trigger was sent by the loading device at the start of each loading cycle. A trigger delay of 50ms or 900ms was included with motion scans to adjust the timing of the acquisition to the loading cycle (Figure 6).

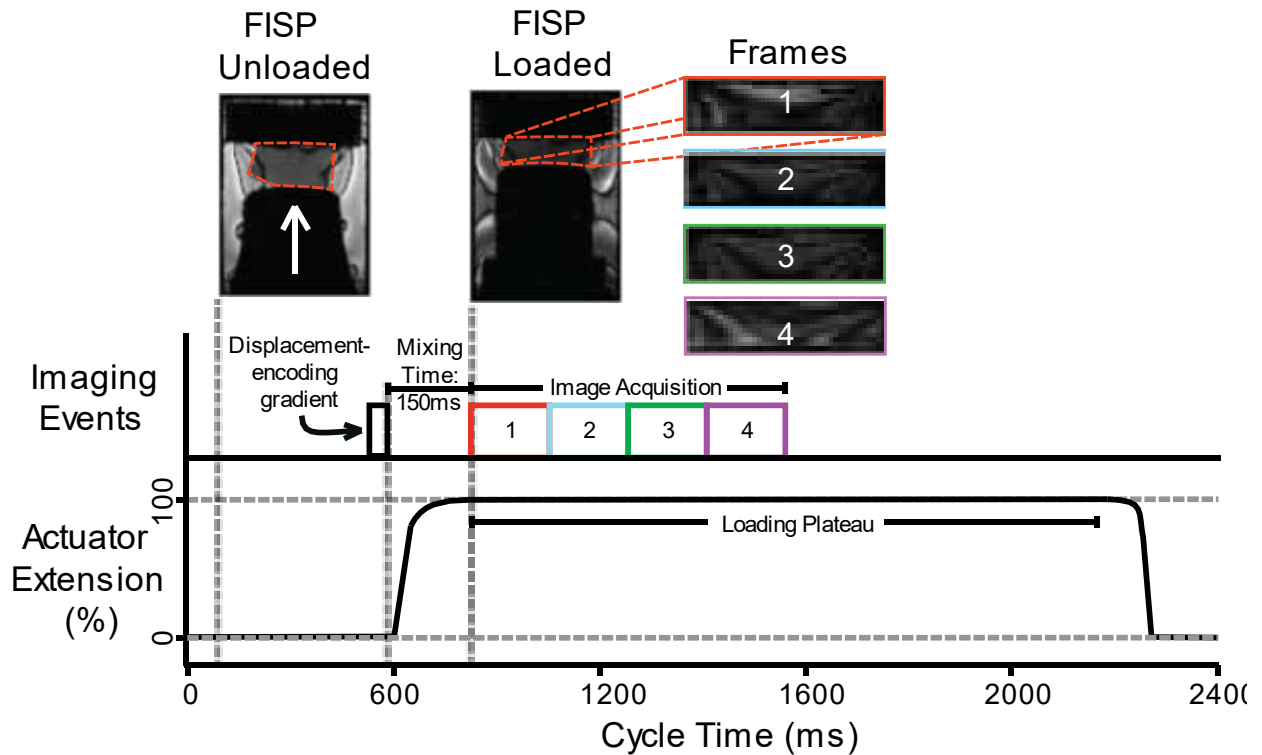


**Figure 6: The synchronization of the loading device with the multi-frame image acquisition and displacement encoding. Displacement encoding was applied before the load, and frames were acquired after a mixing time of 150ms.**

After preconditioning with 300 loading cycles (Martin et al., 2009), I applied displacement encoding via Displacement Encoding with Stimulated Echoes (DENSE), and acquired images with FISP (Aletras, Ding, Balaban, & Wen, 1999; Chan & Neu, 2012). Four

frames were acquired at the start of the loading plateau, 160ms apart. Three explants were loaded and imaged this way. Signal-to-noise ratio (SNR) was computed for each DENSE acquisition as the mean of the ROI within the magnitude data, divided by the standard deviation of a region of noise (Figure 7). The SNRs were averaged across all scans, per frame (Table 1).

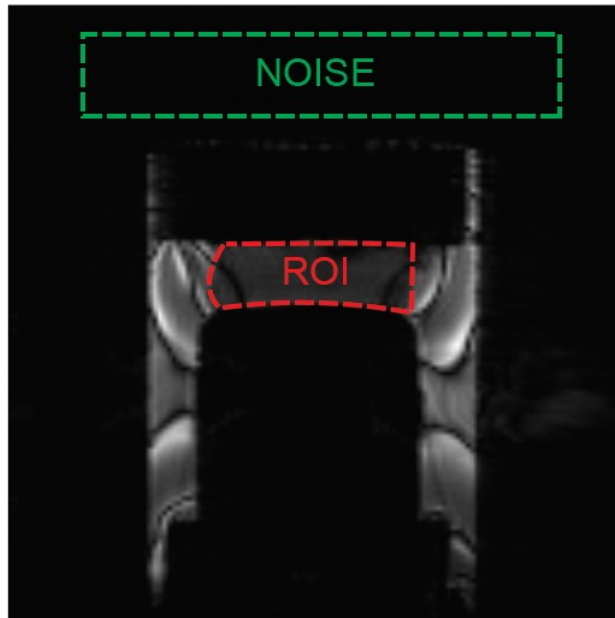


**Figure 7: Loaded FISP image with highlighted regions for ROI mask and noise mask.**

**Table 1: Scan results, average SNR per frame. SNR was computed as the mean of the ROI divided by the standard deviation of the noise.**

Frame #	SNR
1	2.786
2	2.601
3	2.418
4	2.394

### 3.1.6 Viscoelastic Modeling

Cartilage stress relaxation data, as acquired through indentation testing, has produced an excellent fit of data to a quasi-linear viscoelastic (QLV) model (Equation 1)(Fung, 1993) (June & Fyhrie, 2013).

$$gQLV(t) = c \left\{ E \left( \frac{1}{\tau_2} \right) E \left( \frac{1}{\tau_1} \right) \right\} \quad (1)$$

Where E is an exponential integral, defined as:

$$E(y) = \int_y^\infty \frac{\exp(-t)}{t} dt \quad (2)$$

This equation models stress relaxation through three constants,  $c$ , the intensity factor, and time constants,  $\tau_1$  and  $\tau_2$ . QLV models have fitted cartilage explant stress relaxation data *in vitro*(C.-Y. Huang et al., 2001; C. Y. Huang et al., 2003; June & Fyhrie, 2013; Mak, 1986), demonstrating that fluid-independent models still provide an excellent fit of data compared to that of fluid-dependent ones. However, these methods fit data with sampling rates ranging 100-200Hz(June & Fyhrie, 2013; Mak, 1986), with thousands of data points, but only using an indenter on the articulating surface. MRI-based imaging is able to visualize full-thickness mechanics with subpixel resolution, but much lower temporal resolution. Here, I attempted to fit these relaxation parameters to four frames of full-depth cartilage displacements acquired at the start of the loading plateau.

### 3.1.7 Monte Carlo Simulations

A Monte-Carlo simulation was performed using a custom MATLAB script to fit the relaxation constants  $c$ ,  $\tau_1$ , and  $\tau_2$ . An idealized stress-relaxation curve was generated using the

literature values of each constant (June & Fyhrrie, 2013). Four time points were computed for the curve using the timing of the multi-frame image acquisition performed earlier. White Gaussian noise was added to the idealized values in a Monte Carlo simulation of 1000 iterations. Noise was applied for an effective SNR of 0dB (complete noise) to 100 dB (virtually noiseless) in 5 dB increments. MATLAB's Curve Fitting toolbox was employed for parameter estimation with the above equation, using robust fitting options. The mean value for each of the 1000 iterations was calculated and plotted alongside the 95% confidence interval (CI) of the fit and the literature value. With a convergence tolerance of  $10^{-6}$ , convergence occurred for  $c$  at 60dB (Figure 8), for  $\tau_1$  at 65dB (Figure 9), and for  $\tau_2$  at 70dB (Figure 10), which are equivalent to SNRs of  $1 \times 10^6$ ,  $3.162 \times 10^6$ , and  $1 \times 10^7$

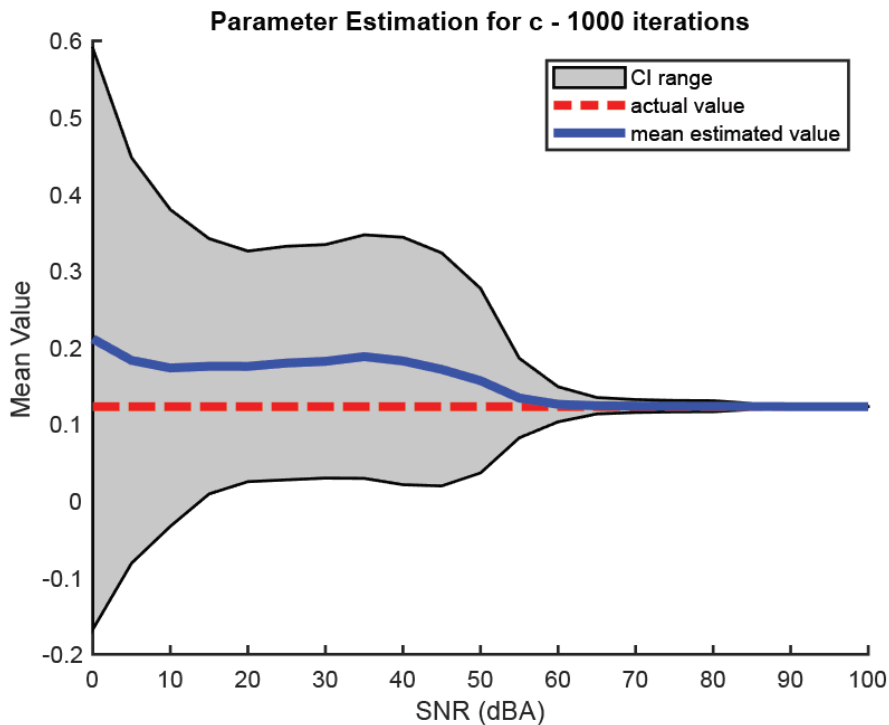


**Figure 8: Parameter estimation for  $c$ , intensity constant. Convergence was observed at 60dB, or  $1 \times 10^6$ .**

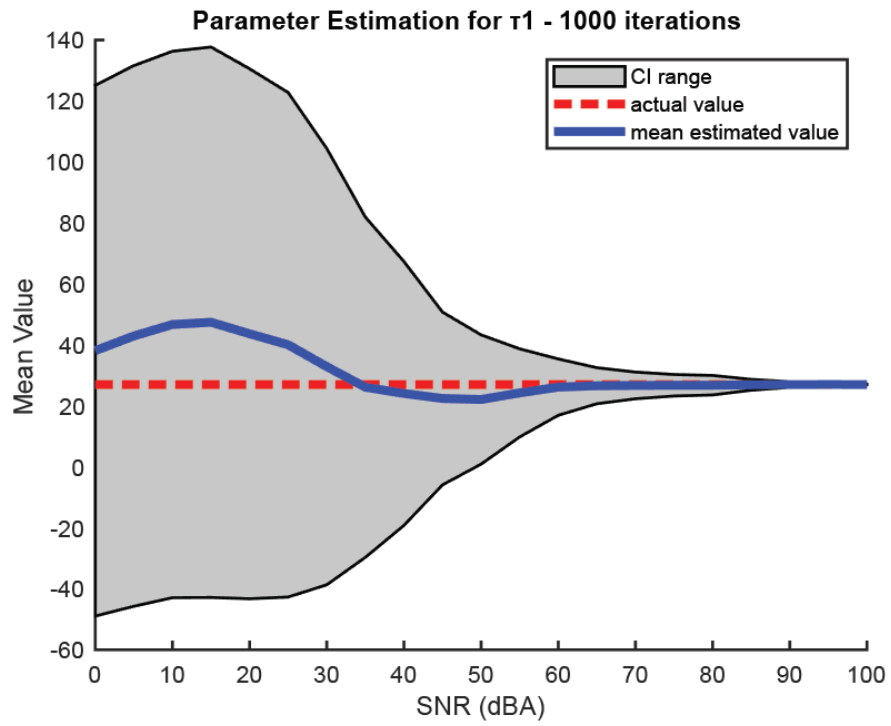


Figure 9: Parameter estimation for relaxation constant  $\tau_1$ . Convergence was observed at 65dB or  $3.162 \times 10^6$ .

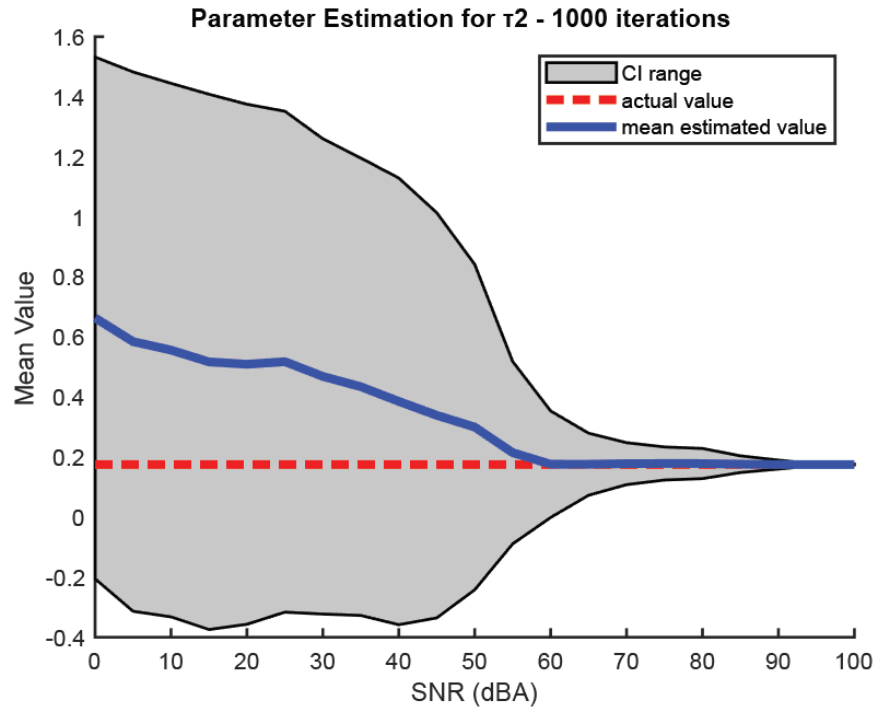


Figure 10: Parameter estimation for relaxation tau2. Convergence was observed at 70dB or  $1 \times 10^7$ .

### 3.1.8 Aim 1A Discussion

As observed with the multi-frame scans, the SNR of the acquisition ranged from approximately 2.8 to 2.4. The Monte Carlo simulation indicated the needed SNR for convergence using only 4 frames from a cine acquisition is closer to 60dB or  $1 \times 10^6$  for the most liberal measure; 6 orders of magnitude greater than the first frame. Previous studies have imaged cartilage with cine FISP acquisitions *in vivo* with an SNR of 35, which is approximately 15.44 dB (Hunold, Maderwald, Ladd, Jellus, & Barkhausen, 2004). Preliminary work with phantoms shows a higher SNR, closer to 15 or 7dB. My SNR is lower than that of previous studies because of my imaging parameters, too low for parameter estimation.

A limitation of the parameter estimation lies with my choice of relaxation function, which has been shown to be inaccurate for more complex mechanical responses such as impact

loading(Selyutina, Argatov, & Mishuris, 2015). However, the modified QLV model was chosen because of the method of loading, which would be performed cyclically at a loading plateau, similar to previous work(Tripathy & Berger, 2012).

While additional frames can be employed to increase temporal resolution, each doubling of the requisite number of frames doubles the needed scan time. Preliminary work has employed scan times close to 40 minutes and suggests scans longer than 1 hour will result in mechanical degeneration of the cartilage tissue. While MRI data may have correlates to tissue viscoelasticity, I am unable to use motion-sensitive techniques to fit full-depth displacement data to viscoelastic parameters due to a combination of insufficient temporal resolution and SNR.

## **3.2 Aim 1B – Spatial Strain Distribution Analysis**

### **3.2.1 Rationale**

Cartilage experiences depth-dependent strains due to depth-dependent mechanical properties(Chan, Neu, & Hull, 2009b; Chen, Bae, Schinagl, & Sah, 2001). In studies examining cyclic loading in cartilage-on-cartilage contact, MRI-based Green-Lagrange strains varied by depth and by distance from contact regions(Chan et al., 2009b; Zevenbergen et al., 2018). These differences appear in both intact and defect cartilage models. Axial, transverse and shear strain distributions have been spatially profiled using DIC data, showing clear differences with altered matrix composition(Irwin et al., 2021). As MRI-based strains have mapped cartilage behavior *in vivo*, and strain distribution reflects material changes *in vitro*, a natural extension is an analysis of MRI-based strain distribution. I assessed the ability of this analysis and traditionally used mean strains in evaluating depth-dependent material property changes.

### 3.2.2 Agarose Phantoms

A phantom with depth-dependent material properties was needed in order to assess a method of spatially-dependent strain distribution analysis. Previously published data has examined the displacement and strain maps of 6 unique, depth-dependent agarose phantoms (Figure 11)(Griebel, Khoshgoftar, Novak, van Donkelaar, & Neu, 2014). The agarose phantoms were assembled from a combination of 2% and 4% agarose- a uniform 2% agarose gel (sample ID: “2”), a uniform 4% gel (“4”), and four types of layered agarose gels. Two gels were poured with a 2% layer on top and a 4% layer on the bottom. In one of these gels, the upper layer comprised 2/3 of the total height, and the bottom was the remaining 1/3 (“22-41”). In the other, the upper layer was 1/3 the total height, the bottom was the remaining 2/3 (“21-42”). Two additional gels were poured with 4% on top and 2% on the bottom with the same configuration for layer thickness, “41-22” and “42-21”. These gels were cyclically loaded in synchrony with MRI DENSE imaging, and their displacement maps acquired(Griebel et al., 2014). Here, I re-examined this published data. Displacements were smoothed using 50 smoothing cycles (Figure A.12), and principal and maximum shear strains computed(Geers, De Borst, & Brekelmans, 1996).

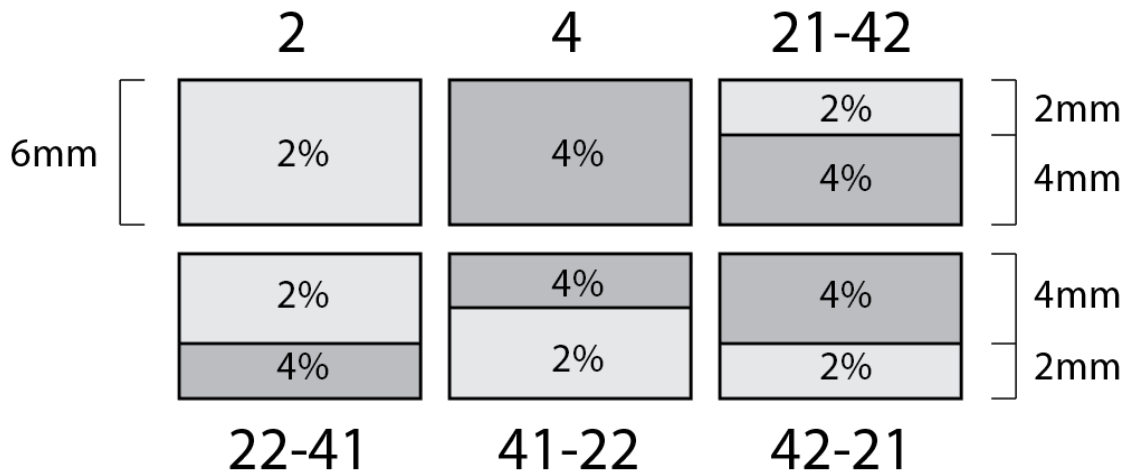


Figure 11: Arrangement and naming scheme for the agarose phantoms.

### 3.2.1 Strain Analysis

The previously published study visualized spatially-dependent strains in the phantoms from the use of a round-tip indenter. In order to compare spatially-dependent strains, I examined the strain distribution in discrete cells of a grid. A rectangular shape of the undeformed phantoms was assumed. Each edge pixel of the deformed maps was registered to the one of the rectangular sides. The rectangular image was divided into a 3x6 grid. The interior of the grid was warped by spline interpolation to the deformed shape of the construct (Figure 12). The deformed grids were then registered back to the undeformed configuration for comparisons. Each cell in the grid, in each strain map, for each phantom was compared to that cell for that map, for every other phantom.

Cell comparisons were performed with Kolmogorov-Smirnov for strain distribution and Mann-Whitney U for means. Kolmogorov-Smirnov tests adjusted for differences in means, and only examined differences in strain distribution shape. The map of statistically significant cells was compared to a logical map of the known differences in agarose concentration based on phantom layout (Figure 11), and sensitivity and specificity computed. Analysis of variance

(ANOVA) and Kruskal-Wallis, while common for depth or spatial analysis of strains and material properties (Klein, Chaudhry, Bae, & Sah, 2007; Zevenbergen et al., 2018), were excluded here because each comparison is guaranteed to have members of both agarose concentrations.

Multiple comparisons were corrected by Bonferroni correction, where the significance level  $\alpha = 0.05$  was divided by the number of comparisons. I compared each cell of a 6x3 grid (18 total) with 15 paired phantom comparisons (6 phantoms, choose 2, excluding duplicates) for a total of 270 comparisons. My significance level of  $\alpha = 0.05$  then became approximately  $\alpha = 1.9 \times 10^{-4}$ . I chose the Bonferroni correction as a highly conservative measure because preliminary testing showed strain distribution to be very sensitive to noise.

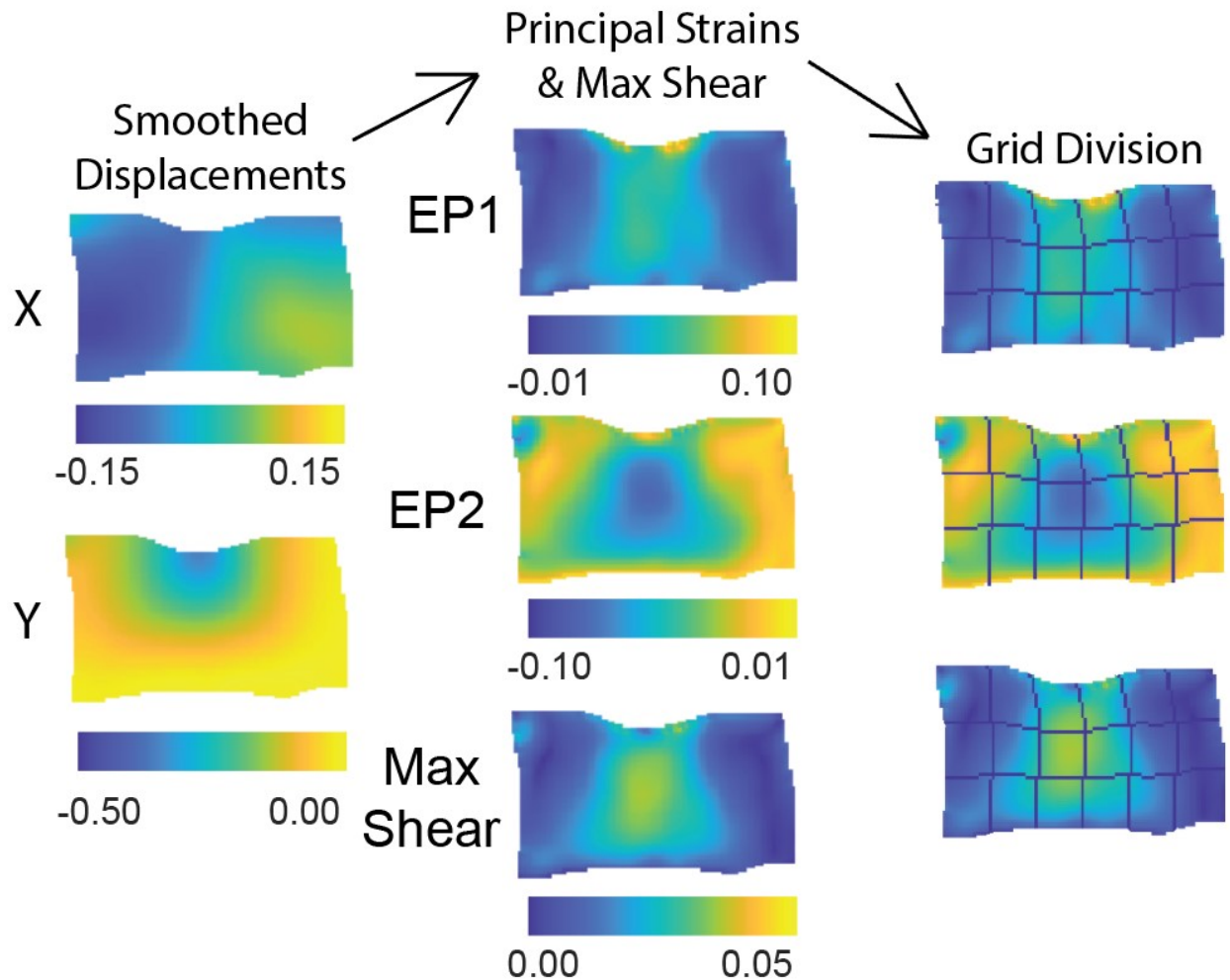


Figure 12: Representative process, using uniform 2% gel. Smoothed displacements are used to compute principal strains, which are divide into deformed grids for analysis. Each cell in the grid for a given phantom was compared to that cell of every other phantom.

### 3.2.2 Results

Kolmogorov-Smirnov (KS) and Mann-Whitney U (MW-U) tests were performed as described on each of 15 phantom-pair combinations, repeated for each strain map. Example analysis is shown for EP1, uniform 2% versus uniform 4%, for KS (Figure 13) and MW-U (Figure 14) tests. Sensitivity and specificity were computed for each method (Table 2).

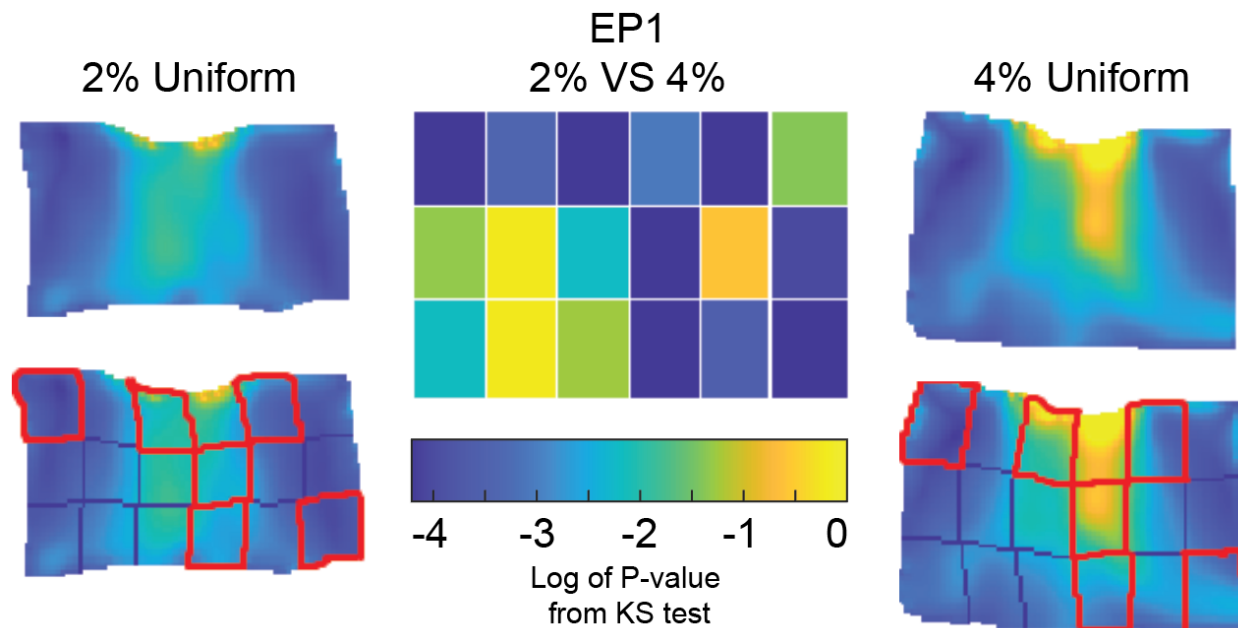


Figure 13: Kolmogorov-Smirnov analysis shown for uniform 2% VS uniform 4%. Strain distribution analysis showed 6 cells that were statistically significant, highlighted in red. Colored grid corresponds to p-values for comparison. Statistically significant cells are at the bottom of the scale and are colored dark blue.

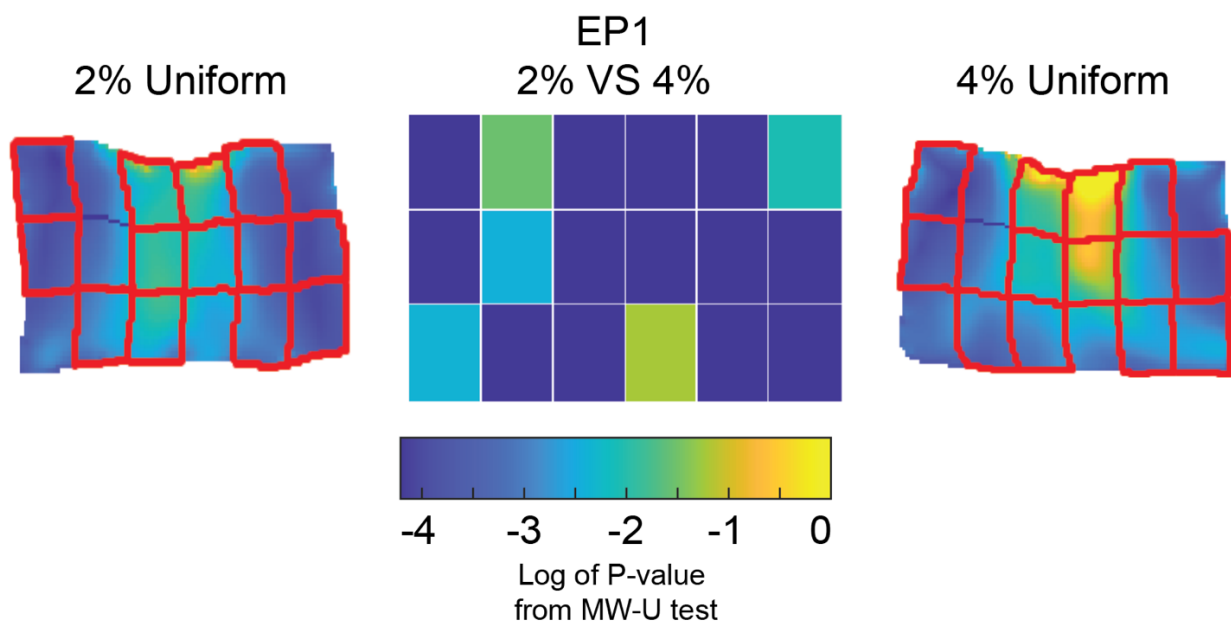


Figure 14: Mann-Whitney U analysis shown for EP1 of uniform 2% VS uniform 4%. Mean analysis shows 13 statistically significant cells, highlighted in red. Colored grid corresponds to p-values for comparison.

**Table 2: Sensitivity and specificity of statistical tests in evaluating depth-dependent material properties. Statistically significant results were compared to a logical map of known differences in agarose concentration.**

	<b>KS Test</b>	<b>MW-U Test</b>
<b>Sensitivity</b>	86.48%	68.64%
<b>Specificity</b>	54.64%	63.91%

### **3.2.3 Aim 1B Discussion**

As Griebel et al. 2014 found, differing full-depth strain patterns can be observed for each phantom. The layers with 2% agarose concentrations experienced relatively diffuse strain concentrations compared to layers with a 4% composition. I analyzed the sensitivity and specificity of discretized strain distribution and mean analyses and in detecting these localized changes in material properties. I found that the Kolmogorov Smirnov test, which normalizes for the difference in mean, was more conservative and less sensitive to changes in agarose concentration than the Mann-Whitney U test. The increased in test specificity was marginal, indicating that most of the information pointing to differences between phantoms was available through the mean strain, not strain distribution.

Previous studies have examined changes in cartilage strains based on known spatially-dependent material changes and treatments. Irwin et al. analyzed interface strains from different repair groups using ANOVA (Irwin et al., 2021). Through measuring mean strains, they demonstrated repair angle was a better predictor of strain than histology or tissue composition. Schinagl et al. investigated the depth-dependent material properties through correlation with depth-dependent mean strains (Schinagl Robert et al., 2005). These studies agree with these results; spatially-dependent mean strains better reflect material property changes.

Limitations of this study included the discretization of strains, which meant the analysis was agnostic to spatial information. Strain is dependent on both material properties and the

applied loading, including the distance from the point of indenter contact. Zones of iso-strain form gradients within the tissue depth; the shape of these patterns is potentially valuable to an examination of depth-dependent material properties.

The analysis here was an effort to move toward a quantitative assessment of spatially-dependent strain maps. With sudden changes in material properties, clearly visible strain gradients arise, dependent upon the orientation and distance from the applied loading and relative stiffnesses of the materials. Mean strains should be considered over strain distribution because of improved sensitivity and supporting literature that demonstrates its correlation to material properties. However, future analysis must consider the spatial relationship of the strain data, either in the form of texture mapping, local measures of variance, or even simple gradient mapping.

## 4. SPECIFIC AIM 2

Current clinical repair assessments are performed qualitatively on morphological data acquired from MRI(Hunter et al., 2011; Roemer et al., 2014; Welsch et al., 2011), while TE repair assessments focus on destructive mechanical tests(Olvera et al., 2015; Theodoropoulos et al., 2016). Morphology alone provides no information about a tissue's ability to sustain load, a vital consideration for load-bearing cartilage. Bulk mechanical tests reduce important information about the repair interface to singleton measurements and cannot visualize or assess the depth-dependent mechanics critical to cartilage function. Through-thickness mechanical assessment is an integral part of evaluating cartilage repair, and should be done without altering boundary conditions and biasing the mechanics being observed. There is a need for full-depth assessment of cartilage repair through non-destructive visualization of mechanical behavior.

Strain mapping has been used to assess through-thickness cartilage behavior *in vitro*. These strains are correlated with relative differences in material properties and interface mechanics, and have been used to assess cartilage repair(Chung, Heebner, Baskaran, Welter, & Mansour, 2015; Irwin et al., 2021; Wang et al., 2018). However, these methods are still destructive and alter boundary conditions. MRI-based strains are non-destructive and non-invasive, and have been acquired *in vivo* to visualize through thickness mechanics(Carter et al., 2015; Chan et al., 2016; Lad et al., 2016). However, MRI-based strains have not been correlated with spatially-dependent material changes or interface mechanics in cartilage repair. Furthermore, methods of assessing spatial information are often limited to the mean or peak value of an ROI, or by plotting the former by percentage of total depth or width. Other fields such as ecology and geology analyze topographical, spatially-dependent information by generating heuristics based on image texture or clustering(Dale, 1999; Plotnick, Gardner,

Hargrove, Prestegaard, & Perlmutter, 1996). The interested reader is directed to a review of these spatial analysis methods for topographical analysis(Dale et al., 2002). These spatial analysis methods have not been applied to strain mapping; their maps of texture-based heuristics may further improve correlates to cartilage repair.

I built finite element (FE) models based on features of successful repair; material stiffness match and integration strength. Simulated MRI-based strains were generated using these models in order to assess their ability in evaluating cartilage repair. Strains were analyzed through correlations between the mean strains and spatially-dependent material properties and interface mechanics. Additionally, I assessed the value of texture-based spatial analysis methods by correlating the mean values of their heuristic maps with the same features.

This work was divided into two sub-aims, each focused on different localized strains. 2A analyzed the strains of an inclusion and the surrounding tissue to evaluate material stiffness match. 2B analyzed the strains of the repair interface to evaluate material property match and integration strength.

## **4.1 Aim 2A Methods**

### **4.1.1 Spatial Analysis of Strains**

Several common methods of spatial analysis were implemented; variance-to-mean-ratio (VMR), lacunarity analysis, Moran's Index of autocorrelation (Moran's I), and gradient mapping.

The first was variance-mean ratio (VMR). The variance of all pixels within a moving window of size  $r$  is divided by the mean, and applied to a single pixel. The VMR is mapped and treated as a local measure of variance (Equation 6)(Dale, 1999; Pritchard, 2001).

$$m_1(r) = \sum_{i=1}^r \frac{x_i}{n} \quad (3)$$

Where  $m_1$  is the first moment of data (the mean) (Equation 3) with a window size  $r$ , with  $n$  total pixels (Equation 4). Then  $s^2$  is the variance (Equation 5).

$$n = r^2 \quad (4)$$

$$s^2 = \frac{\sum_{i=1}^r x_i^2 - nm_1^2}{n-1} \quad (5)$$

$$VMR_r = \frac{s^2}{m_1} \quad (6)$$

The next method employed is lacunarity analysis (Equation 8), which is similar to VMR. Values are computed inside a moving window, but instead measures the 2<sup>nd</sup> moment of the data ( $m_2$ ) (Equation 7) divided by square of the first moment ( $m_1$ ) (Equation 3).

$$m_2(r) = \sum_{i=1}^r \frac{x_i^2}{n} \quad (7)$$

$$\Lambda(r) = \frac{m_2(r)}{m_1(r)^2} \quad (8)$$

This measure is related to VMR and is for texture-mapping of sparsely or densely clustered data points (Plotnick et al., 1996; Plotnick, Gardner, & O'Neill, 1993).

Moran's I is a local index of spatial autocorrelation (Equation 9). Autocorrelation is a metric for texture recognition. Areas with highly clustered or similar data exhibit high positive autocorrelation, while areas with highly separated or dissimilar data exhibit negative autocorrelation. Randomly scattered data features no autocorrelation.

$$I(r) = \frac{\sum \sum w_{ij}(r)(x_i - \bar{x})(x_j - \bar{x})}{W(r) \sum \frac{(x_i - \bar{x})^2}{n}} \quad (9)$$

Gradient mapping was also implemented (Equation 11). The direction and intensity of each pixel was approximated using the partial derivative of the change in pixel intensity in the X

and Y directions (Equation 10). Gradient mapping measures local rates of change and is used to create topographical maps(Dale, 1999).

$$\nabla f = \begin{bmatrix} g_x \\ g_y \end{bmatrix} = \begin{bmatrix} \frac{\partial f}{\partial x} \\ \frac{\partial f}{\partial y} \end{bmatrix} \quad (10)$$

$$f = \sqrt{g_y^2 + g_x^2} \quad (11)$$

#### 4.1.2 Finite Element Model

An FE model was created of a cartilage explant and round-tipped indenter. Explant geometry was modeled as an 80 $\mu$ m-thick, full-depth cross section of a cylinder, 8mm diameter, 4mm tall, while the indenter was modeled similarly as a cross section of a hemisphere, 16mm diameter. The explant was modeled with an eccentric region of softer tissue, from the articulating surface to half of full depth, intended to model an inclusion. Geometry was cut in half for reduced computational load (Figure 15). All motion was constrained to in-plane motion, except the inner edge of the tissue and indenter constrained to Y-axis motion.

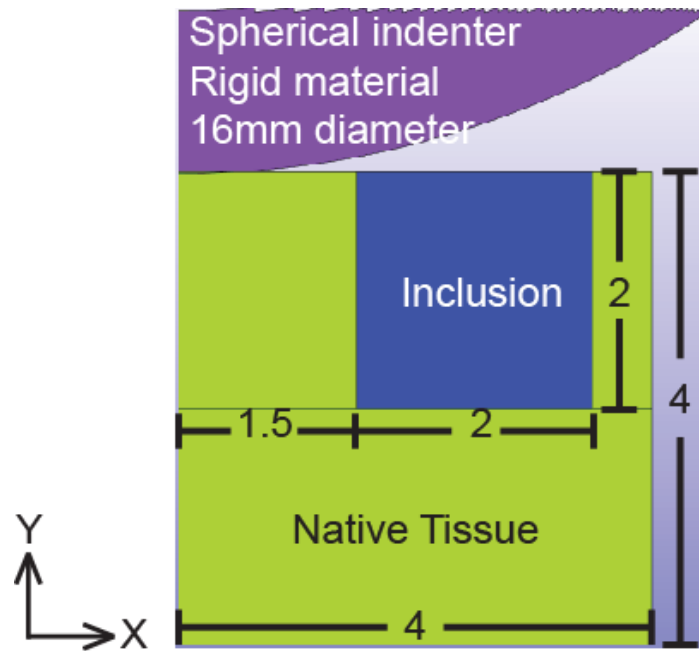


**Figure 15: Model layout, showing position of the inclusion (blue) relative to the healthy tissue (lime green). Assumptions of half-symmetry are made, and the model is cut in half. The left side of the model is the center of the tissue, the inner edge, while the right is the outer edge. The indenter (purple) indents the tissue on the articulating surface of the modeled explant. All dimensions are in millimeters.**

The meshes for all pieces of geometry was hexahedral (8 node 0.04-mm cubic elements). The indenter was modeled as a rigid body, while the healthy cartilage was a biphasic material (a porous neo-Hookean solid component with constant fluid permeability). The inclusion was modeled similarly, but with varying Young's modulus and Poisson's ratio. The properties ranged from those representative of damaged cartilage, ICRS OA grades 1, 2 and 3 to those of healthy tissue (Table 3), and then beyond those seen in healthy tissue (Kleemann, Krockner, Cedraro, Tuischer, & Duda, 2005). The values ranged from 30% of healthy to 150% of healthy, in steps of 10%. Models were labeled by the ratio of the inclusion stiffness and healthy tissue stiffness, which was termed the stiffness ratio (Table 4). Values for Poisson's ratio as determined by unconfined compressed were unavailable for ICRS-graded cartilage. Instead, Young's modulus and Poisson's ratio were varied together because compressibility and elastic stiffness are tied to

collagen matrix integrity(Kiviranta et al., 2006), which becomes weaker with OA progression(Kumar et al., 2015).

A compressive load of 0.163N (equivalent to 100N) was applied in the negative Y axis with the rigid indenter, ramping up linearly from 0N over 0.1 seconds. This was done to improve computational stability. The model was run in FEBio with a non-symmetric, steady-state BFGS solver with 10 steps, 0.01 seconds each.

**Table 3: Literature value ranges for damaged and healthy cartilage (Kleemann et al., 2005; Little, Bawolin, & Chen, 2011; Mow & Guo, 2002) , Values considered for healthy, healthy properties are bolded.**

Property	ICRS Grade			Healthy
	3	2	1	-
Young's Modulus (MPa)	0.28 ± 0.12	0.37 ± 0.13	0.50 ± 0.14	0.41 - <b>0.85</b>
Poisson's Ratio	-	-	-	0.06 - <b>0.30</b>

**Table 4: Young's modulus and Poisson's ratio for each model. The model with healthy-level parameters is bolded.**

Stiffness Ratio	30%	40%	50%	60%	70%	80%	90%	<b>100%</b>	110%	120%	130%	140%	150%
Young's Modulus (MPa)	0.26	0.34	0.43	0.51	0.60	0.68	0.77	<b>0.85</b>	0.94	1.02	1.11	1.19	1.28
Poisson's Ratio	0.09	0.12	0.15	0.18	0.21	0.24	0.27	<b>0.30</b>	0.33	0.36	0.39	0.42	0.45

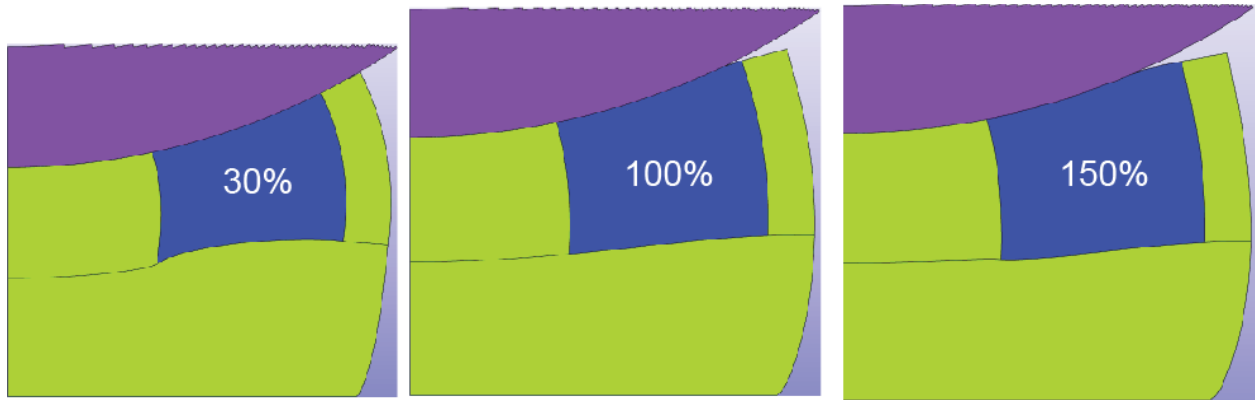


**Figure 16: Fully loaded models. The inclusion (blue), varied in stiffness ratio, ranging from 30% of healthy stiffness (softest), 100% (matching healthy), and up to 150% (above healthy).**

### 4.1.3 Data Processing

I approximated MRI-based strains with synthesized displacement maps generated using FE model data. Transverse and axial element displacements were extracted from the final time step of each FE model and interpolated into 64x64-pixel displacement maps. The effective FOV was 5.25 x 5.25mm and pixel size was approximately 82 $\mu$ m, similar to that of preliminary scans. Scanner noise was simulated by treating interpolated displacement maps using white Gaussian noise with a standard deviation 0.0061mm, the pooled standard deviation observed from preliminary precision studies. Noisy maps were smoothed with 20 cycles of a 5x5 Gaussian filter (Figure 17). Smoothed displacements were used to compute first ( $E_1$ ) and second ( $E_2$ ) principal strains, along with maximum shear strains. Principal and maximum shear strains were chosen as a conservative estimate of maximal and minimal tissue deformation.

### 4.1.4 Data Analysis

The previously mentioned spatial analysis metrics (VMR, lacunarity, Moran's I, gradient mapping) were computed for each strain map using a window size of 5 pixels where relevant. Two ROIs were established within the displacement maps. The first ROI covered the inclusion, while the second covered the surrounding 5 pixels (Figure 18). The ROIs were generated using

the known geometry of the model. The means of each ROI were calculated for strains and each spatial analysis heuristic. The ratio of the two means comprised a single point for each of the FE models, and was termed the mean ratio. Pearson's correlation was performed between the mean ratio and the stiffness ratio.

I assessed the ability of the mean ratios of strain and spatial heuristics in evaluating stiffness match by identifying what each curve determined as the optimal model. The optimal model had a mean ratio close to 1 in straight-line curves, or a minimum/maximum value for a U-shaped curve. Straight-line curves with a near-perfect correlation (absolute value 0.95 or higher) and an optimal model within close to the 100% model (ranging from 80%-120% stiffness) were considered successful evaluators of stiffness ratio. U-shaped mean ratio curves with optimal models approaching ranging from 80%-120% were also considered successful evaluators of material stiffness. This range was chosen as a conservative measure of successful stiffness recapitulation within TE construct studies(Beck, Barragan, Tadros, Gehrke, & Detamore, 2016; Raghunath, Rollo, Sales, Butler, & Seifalian, 2007; Woodfield et al., 2004; Xu et al., 2018).

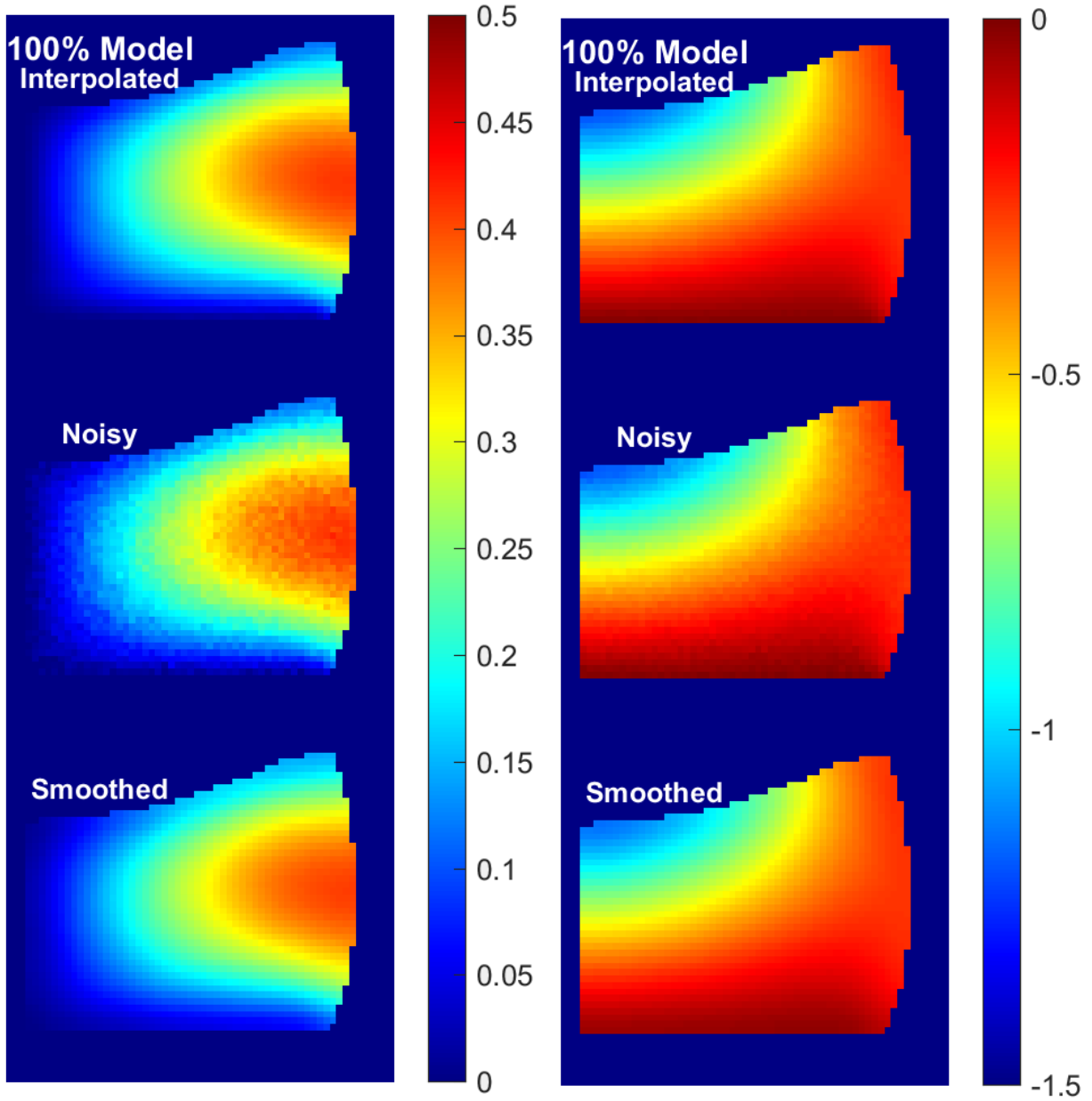
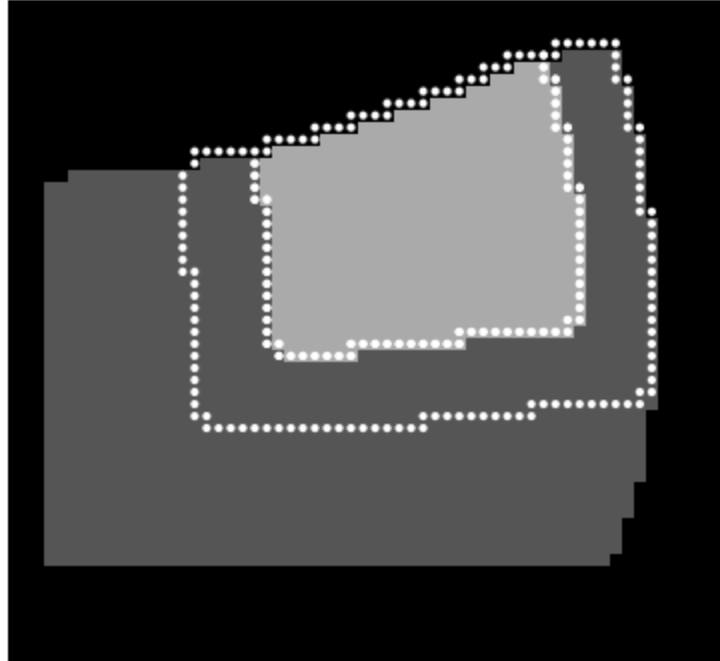


Figure 17: Displacement treatment process shown with transverse (left) and axial (right) displacements from the 100% stiffness model. Interpolated displacements are injected with noise, and then smoothed. Displacements are in millimeters.



**Figure 18: FE model mask, shown for the 100% stiffness ratio model. The light grey in the center denotes the inclusion, while the dark grey is the healthy tissue. Dotted white lines indicate the ROIs. The first ROI covers the inclusion (inner dotted line) while the second ROI (outer dotted line) is the bordering region. Analysis was performed on the ratio of the means from each ROI, termed the mean ratio.**

## **4.2 Aim 2A Results**

### **4.2.1 Displacements**

I observed positive transverse displacements concentrated in the outer edge of the tissue as the compressive load from the indenter caused the material to bow outward (Figure 19A). The peak displacement ranged from 0.39mm in the 30% ratio model, and increased to a peak of 0.447mm in the 150% ratio model. The displacements along the inner edge (the left side), were close to zero.

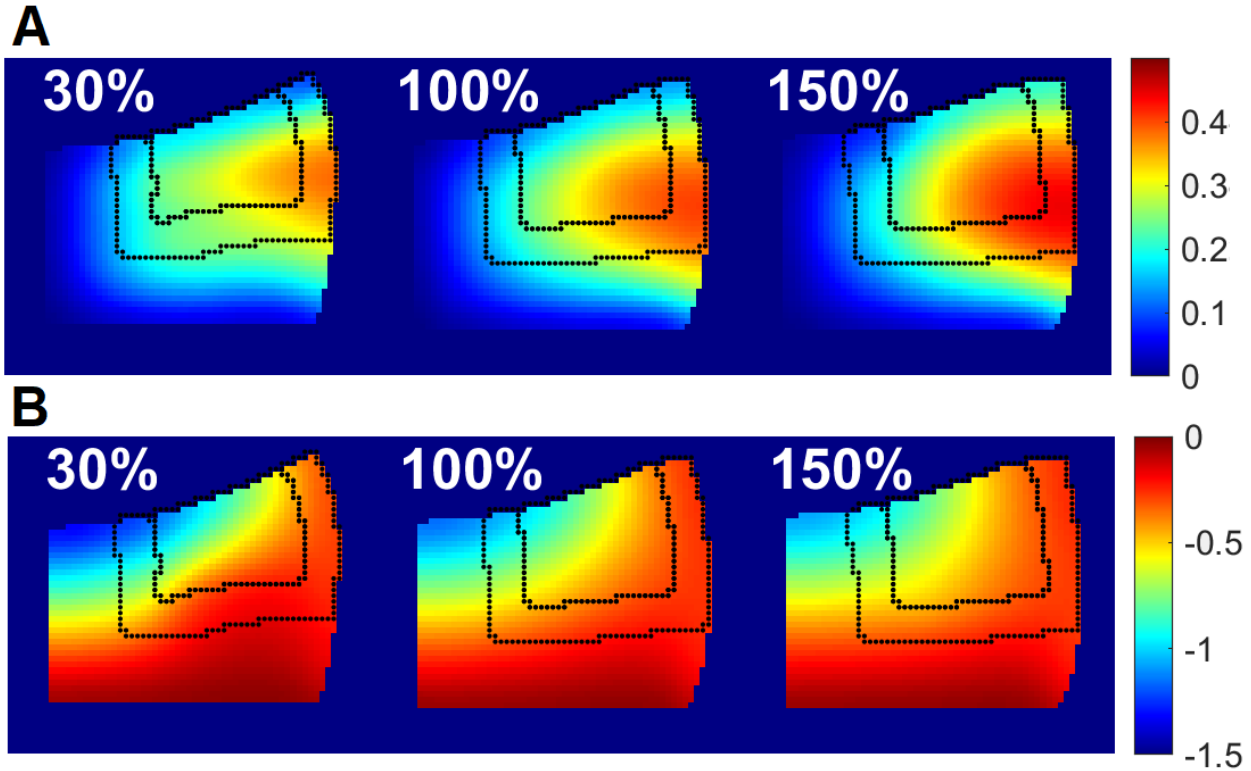


**Figure 19: Transverse (A) and axial (B) displacements of representative models. Displacements are in millimeters. Analysis ROIs are shown. The inner dotted line covers the inclusion, the outer covers 5 pixels of the surrounding tissue.**

Negative axial displacements (Figure 19B) were concentrated near the point of contact with the indenter. This concentration was present in all models, but was highest in the 30% model with a peak of -1.38mm. The peak displacements decrease with increasing stiffness ratio, down to -1.11mm in the 150% model.

#### 4.2.2 Strain Mapping

In the 30% model,  $E_1$  (Figure 20) shows multiple strain concentrations through the inclusion and bordering region, peaking at 23.2%. At 100% stiffness ratio, these strains are reduced in peak and number, peaking close to 20%. At 150%, there is a large concentration of tensile strains within the inclusion, peaking at 22.7%. There are multiple strain concentrations

around and in the inclusion in the 30%. They are reduced in magnitude at 100%, but become consolidated at 150%.

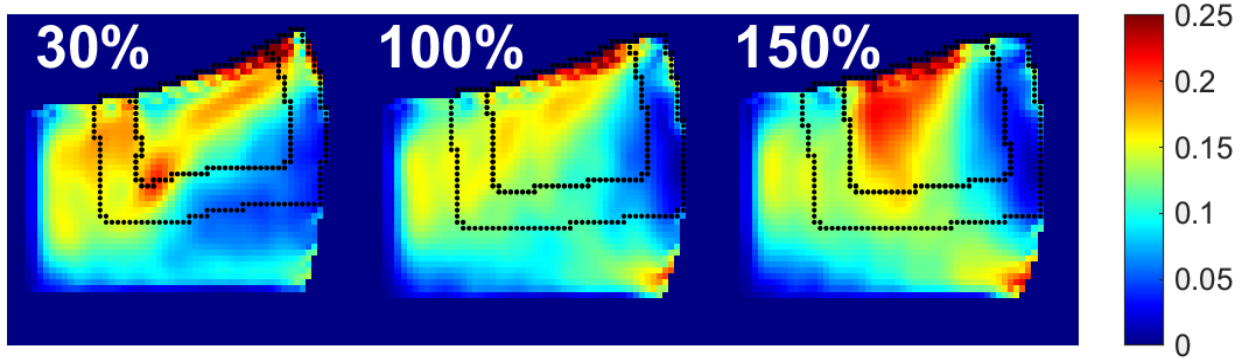


**Figure 20:  $E_1$  of representative models. Analysis ROIs are shown. The inner dotted line covers the inclusion, the outer covers 5 pixels of the surrounding tissue.**

$E_2$  strains (Figure 21) are highly concentrated within the lower and inner portion of the inclusion, peaking at -41.8%. The strain concentration is lessened at 100%, peaking at -34.6%. At 150%, the strain is further reduced, peaking at -31.7%. The topography shows a concentration in the inclusion in the 30% model which becomes smoother at 100%.

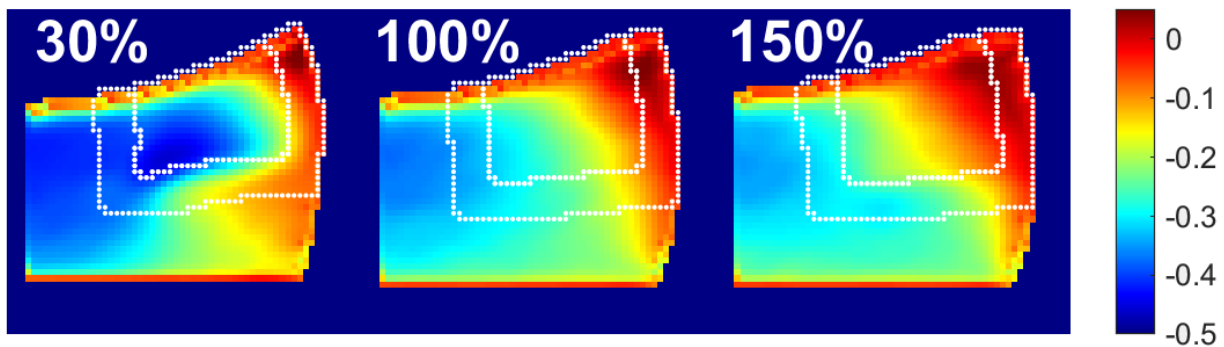


**Figure 21:  $E_2$  of representative models. Analysis ROIs are shown. The inner dotted line covers the inclusion, the outer covers 5 pixels of the surrounding tissue.**

Maximum shear strains (Figure 22) were concentrated in the lower, inner edge of the inclusion in the 30% model, peaking at 18.2%. This concentration was reduced and moved

outside of the inclusion as the stiffness ratio increased to 100%, with a peak of 12.9%, with smoother topography. The 150% model had a lower peak at 12.1%, but several small strain concentrations.

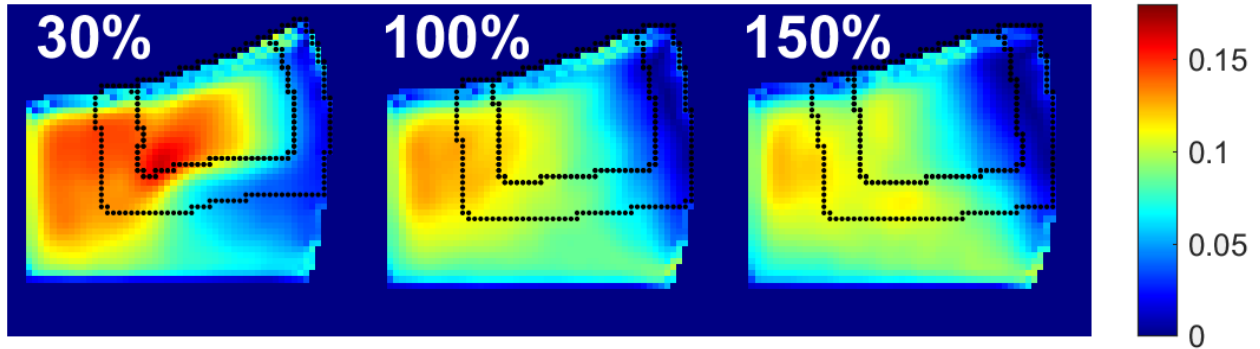


Figure 22: Maximum shear of representative models. Analysis ROIs are shown. The inner dotted line covers the inclusion, the outer covers 5 pixels of the surrounding tissue.

### 4.2.3 Spatial Analysis

VMR mapping (Figure 23) showed changes in heuristic topography when the stiffness ratio increased for all three strains. High,  $E_1$  VMR values are concentrated near the upper, outer edge of the inclusion, moving toward the surface. The mean VMR decreases between 30% to 100%, but increases again at 150%. For  $E_2$ , the topographical map shows a peak heuristic concentration in the upper edge in the 30% model, becoming more diffuse in the 100% model, and then increasing again at 150%. For maximum shear strains, the heuristic concentration moves from the lower edge of the inclusion at low stiffness ratio, to the outer edge of the inclusion at high stiffness ratio, especially at 150%.

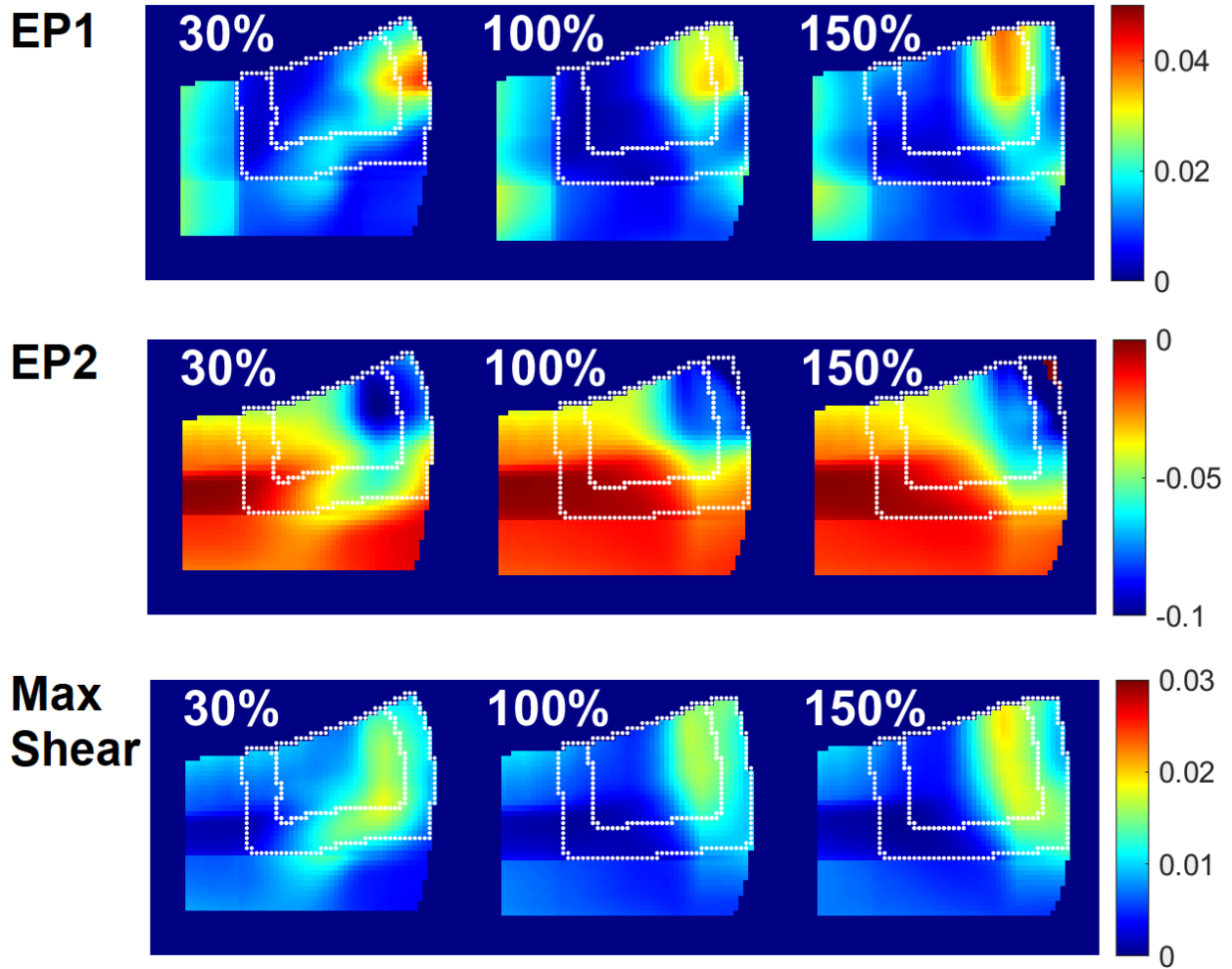


Figure 23: VMR maps of all strains, for representative models. Analysis ROIs are shown. The inner dotted line covers the inclusion, the outer covers 5 pixels of the surrounding tissue.

Lacunarity analysis (Figure 24) showed a similar trend to VMR. High heuristic concentrations were presented toward the upper and outer edge of the tissue. Increasing stiffness ratio moved the heuristic peaks toward the outer edge of the inclusion in all strain maps and increased peak values, but did not show any topographical changes.

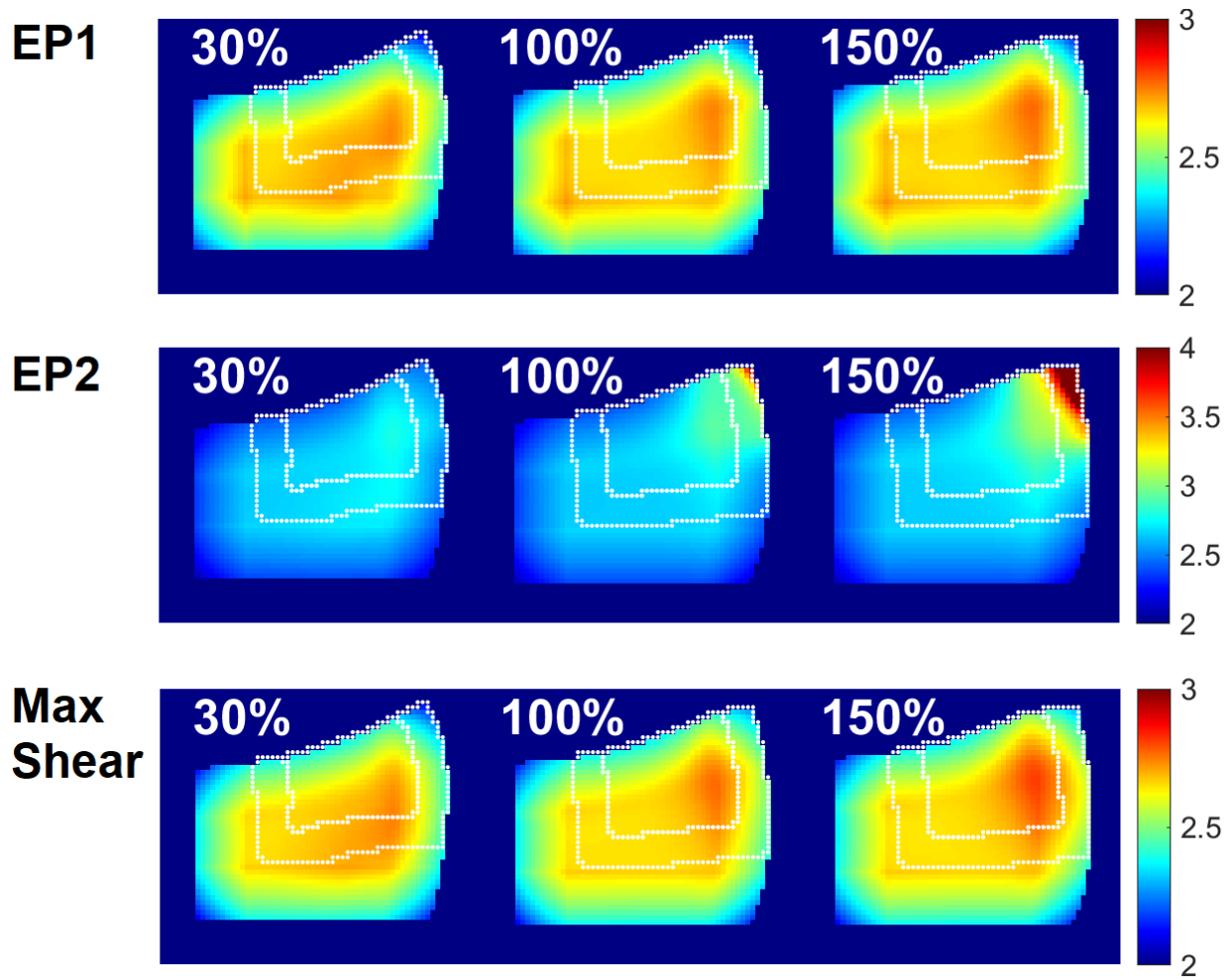


Figure 24: Lacunarity analysis for all strains, for representative models. Analysis ROIs are shown. The inner dotted line covers the inclusion, the outer covers 5 pixels of the surrounding tissue.

Moran's I (Figure 25) showed clear shifts in the highly autocorrelated areas with increasing stiffness ratio for all three strains.  $E_1$  bears a concentration toward the lower inner edge of the inclusion, becoming diffuse and moving away from the inclusion.  $E_2$  shows a highly autocorrelated region within the lower edge of the inclusion, decreasing when the stiffness ratio was 100%, and increasing again inferior to the inclusion at 150%. Maximum shear strains exhibited a highly autocorrelated region near the lower edge of the inclusion at 30%. This concentration moved toward the inner edge of the healthy tissue at 100%, away from the

inclusion. At 150%, the inner portion and outer lower edge of the healthy tissue show high relative autocorrelation, but not the inclusion itself.

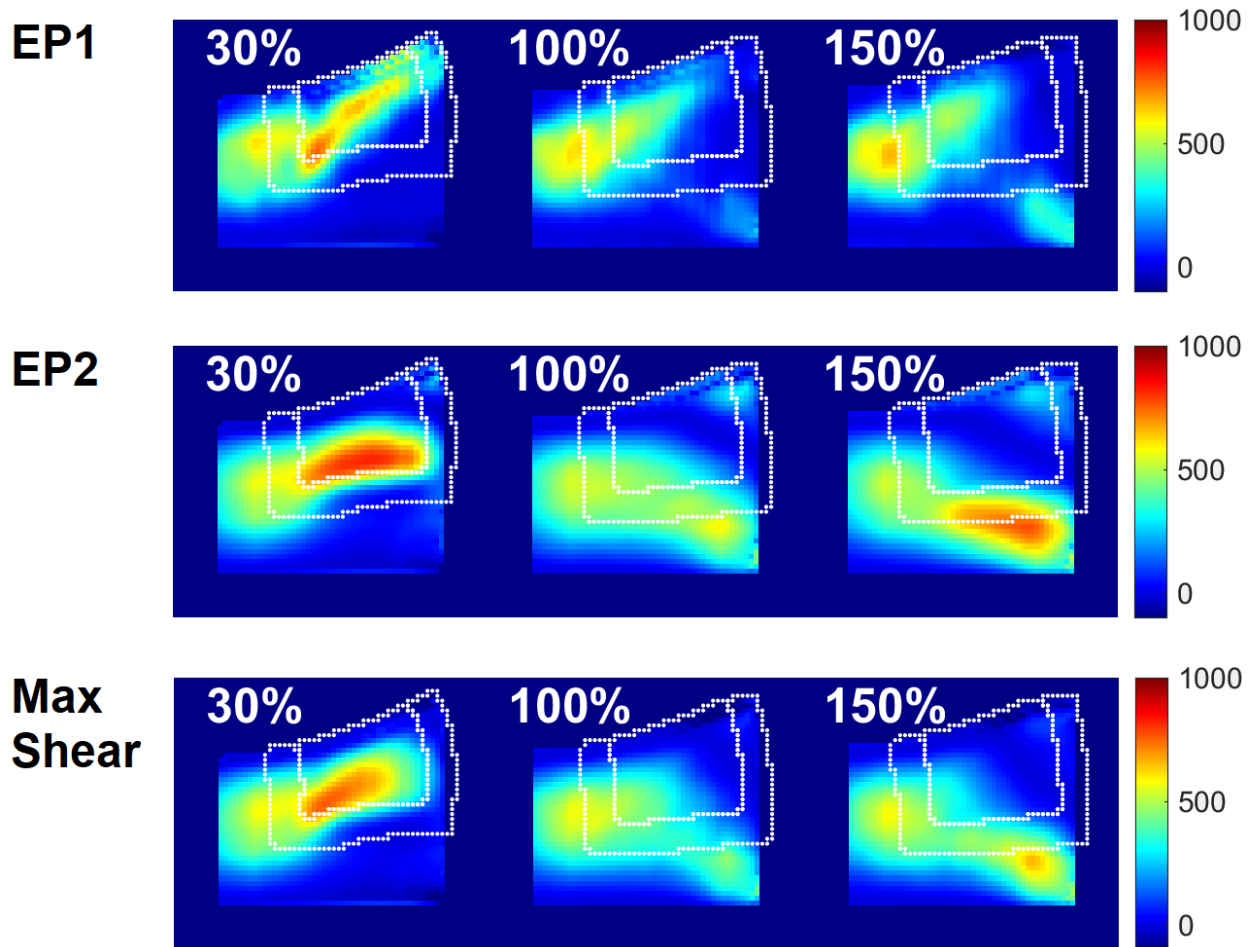


Figure 25: Moran's I of all strains, for representative models. Analysis ROIs are shown. The inner dotted line covers the inclusion, the outer covers 5 pixels of the surrounding tissue.

Gradient mapping (Figure 26) also showed clear shifts in gradient intensity with increasing stiffness ratio in all three strains. In  $E_1$ , the 30% model had a high relative gradient toward the lower, inner edge of the inclusion. The gradient intensity is reduced at 100% stiffness, with no clear concentrations or peak.

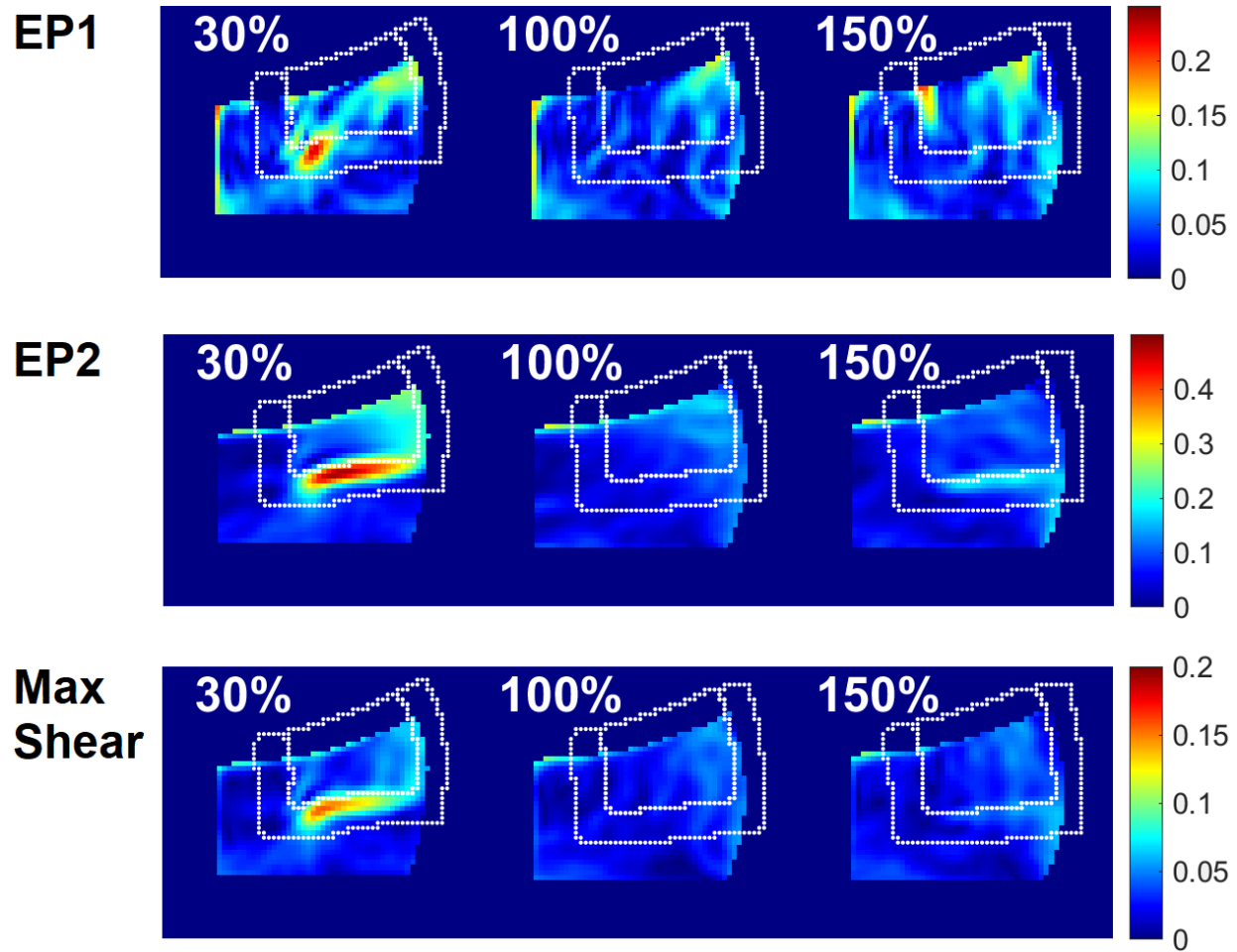


Figure 26: Gradient mapping of all strains, for representative models. The outer 3 pixels were excluded from gradient analysis to avoid edge bias. Analysis ROIs are shown. The inner dotted line covers the inclusion, the outer covers 5 pixels of the surrounding tissue.

At 150%, several high-gradient areas appear near the inclusion surface.  $E_2$  has a high gradient toward the lower edge of the inclusion. This gradient becomes smooth at 100%, but begins to increase in the same location at 150%. Maximum shear strains exhibit a similar pattern as  $E_2$ , but with reduced peaks. Relative gradient intensity is high at the lower inclusion edge but becomes smooth at 100% stiffness. The 150% model has scattered topographical irregularities near the lower outer edge of the inclusion border.

#### 4.2.4 Correlation and Plots

The mean ratios for  $E_1$  (Figure 27),  $E_2$  (Figure 28), and maximum shear (Figure 29) mean strain and mean spatial analysis heuristics were plotted against the stiffness ratio. Pearson's correlation was performed between the mean ratio and stiffness ratio (Table 5). Optimal models were determined from the mean ratio curves (Table 6). The methods that identified optimal models close to the truly optimal case, the 100% model, were considered successful evaluators of stiffness match. Mean ratio of  $E_2$  and its gradient map, as well as the mean ratio of the maximum shear gradient map were successful evaluators.

**Table 5: Pearson's correlation values for the mean ratio of each analysis method VS the stiffness ratio. Strong correlations are in bold green and red colors, for positive and negative correlations respectively. Color intensity fades with decreasing correlation strength. Values between below -0.50 and above 0.50 were considered strongly correlated. Values with absolute value 0.95 or greater were considered nearly perfectly correlated.**

<b>Correlation</b>	<b>Mean</b>	<b>VMR</b>	<b>LAC</b>	<b>Moran's</b>	<b>Grad</b>
$E_1$	0.974	0.888	0.925	-0.990	0.637
$E_2$	-0.996	-0.687	-0.805	-0.950	0.279
Max Shear	-0.987	0.949	0.952	-0.953	0.654

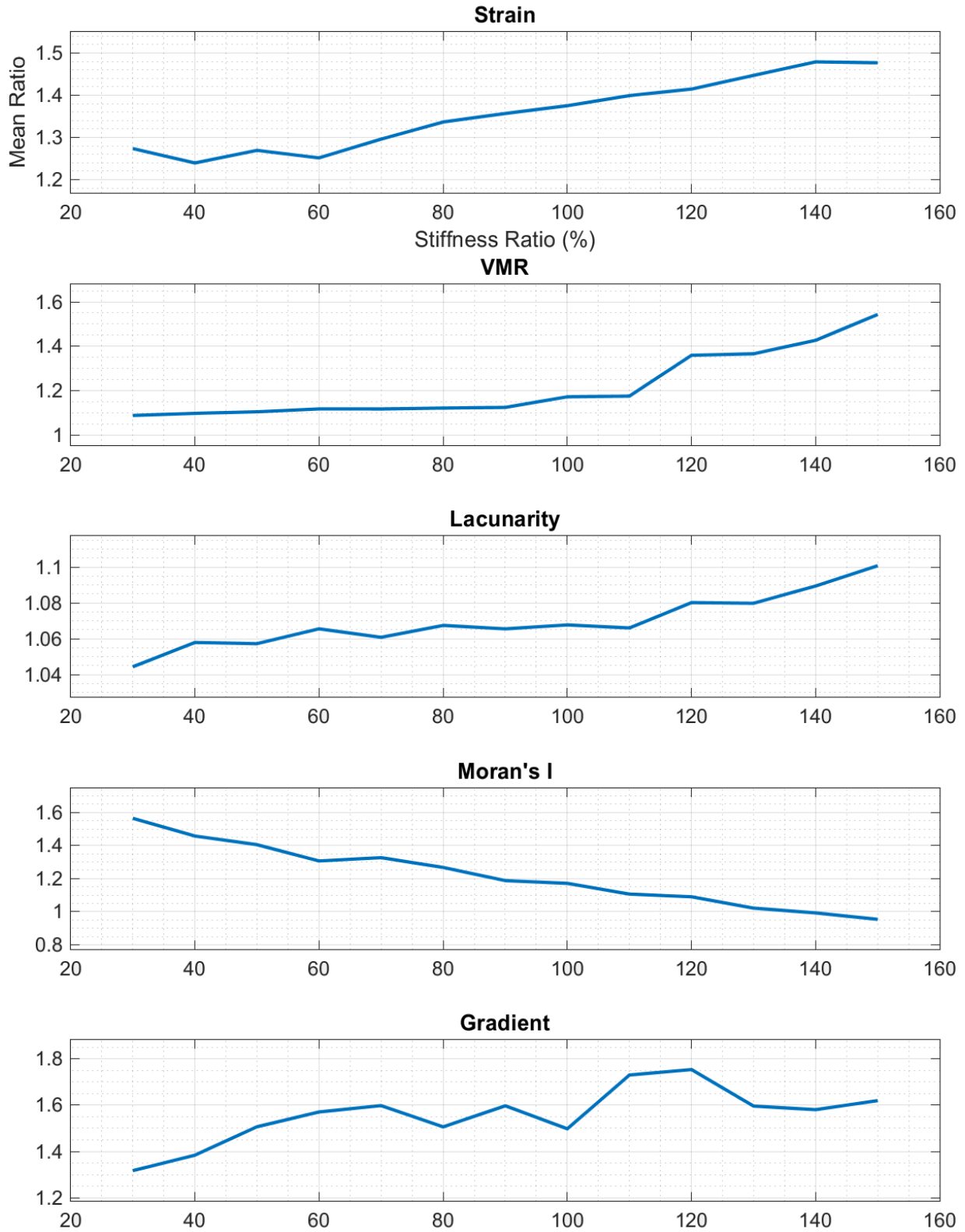


Figure 27: E1 mean ratio plots for all analysis methods.

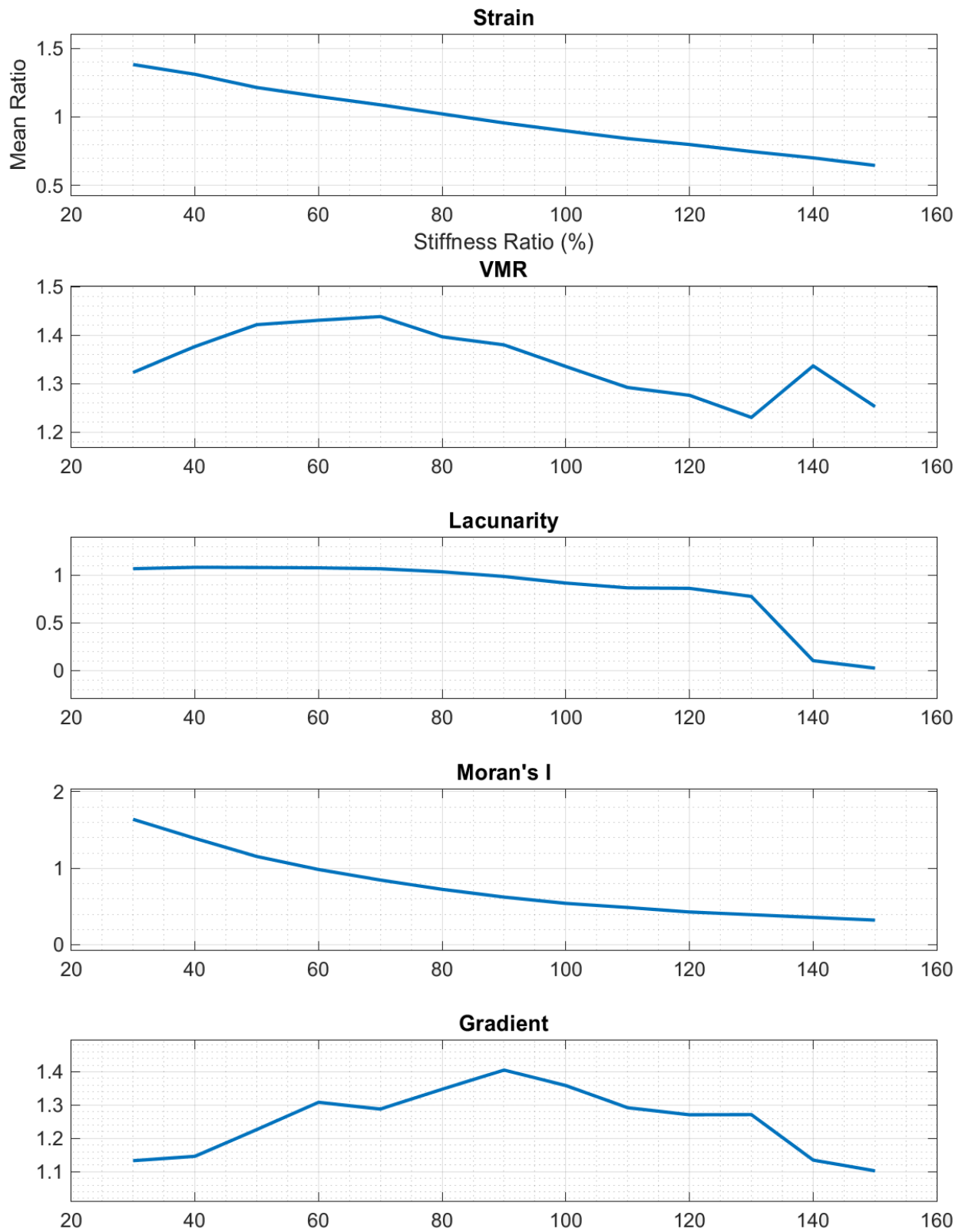


Figure 28: E2 mean ratio plots for all analysis methods.

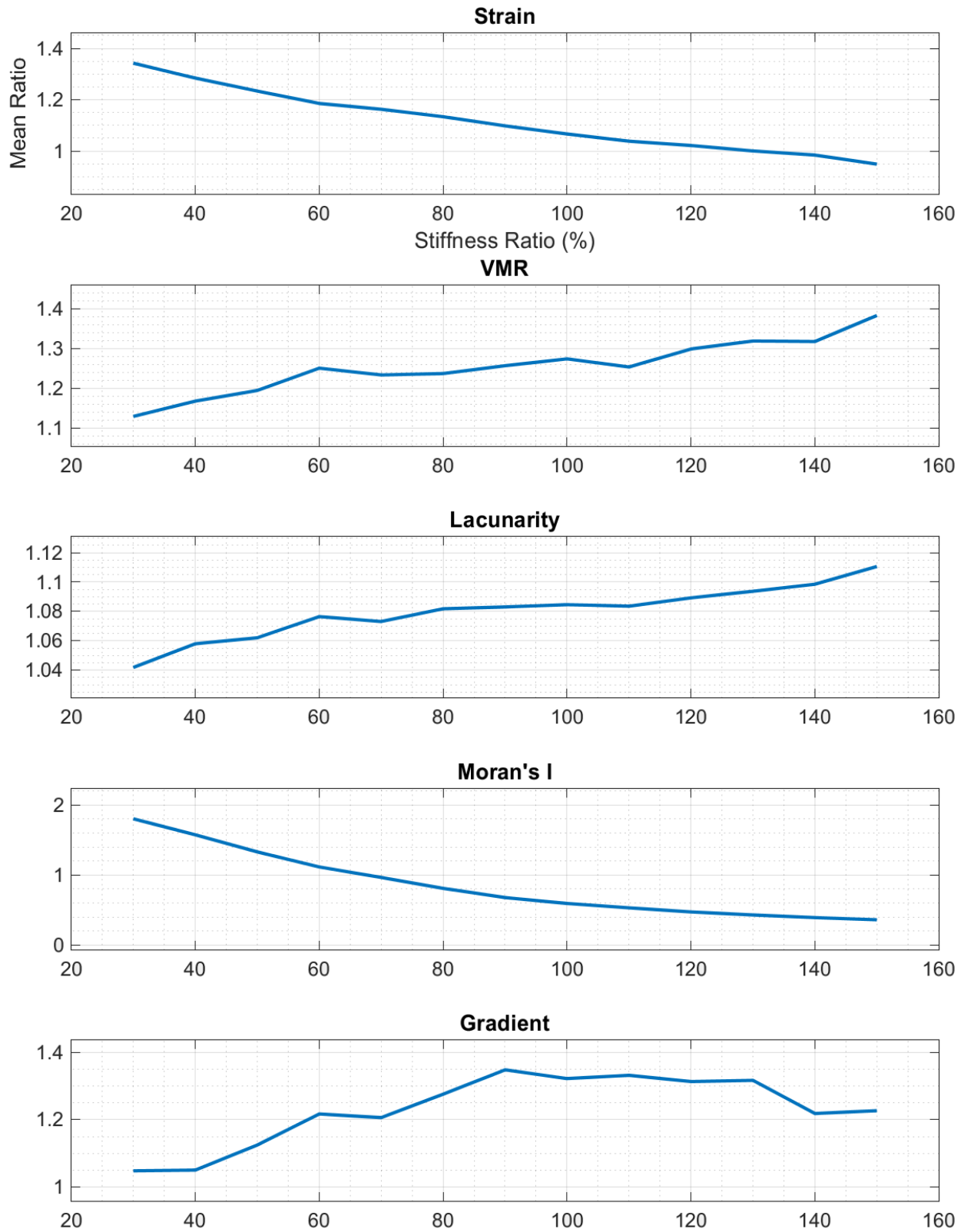


Figure 29: Maximum shear mean ratio plots for all analysis methods.

**Table 6: Optimal models as determined by the mean ratio-stiffness ratio curve. The optimal model along the curve yielded the value closest to 1, or a minimum/maximum. Each mean ratio's ability to assess stiffness ratio was evaluated through the proximity of the optimal model to 100% and the degree of correlation/curve shape. If value met one of these criteria, it was highlighted orange. If it met both, it was highlighted blue.**

<b>E<sub>1</sub></b>	<b>Optimal Model</b>	<b>Proximity to 100%</b>	<b>Correlation</b>
<b>Strain</b>	<b>40%</b>	<b>60%</b>	<b>0.974</b>
VMR	30%	70%	0.888
Lac	30%	70%	0.925
Moran's I	150%	50%	-0.990
Gradient	30%	70%	0.637
<b>E<sub>2</sub></b>	<b>Optimal Model</b>	<b>Proximity to 100%</b>	<b>Correlation</b>
<b>Strain</b>	<b>80%</b>	<b>20%</b>	<b>0.996</b>
VMR	130%	30%	-0.687
Lac	90%	10%	-0.805
Moran's I	60%	40%	-0.950
<b>Gradient</b>	<b>90%</b>	<b>10%</b>	<b>0.276</b>
<b>Max Shear</b>	<b>Optimal Model</b>	<b>Proximity to 100%</b>	<b>Correlation</b>
<b>Strain</b>	<b>130%</b>	<b>30%</b>	<b>-0.987</b>
VMR	30%	70%	0.949
Lac	30%	70%	0.952
Moran's I	70%	30%	-0.953
<b>Gradient</b>	<b>90%</b>	<b>10%</b>	<b>0.654</b>

### 4.3 Aim 2A Discussion

The most successful evaluators of material stiffness match were E<sub>2</sub> mean strain, E<sub>2</sub> gradient, and maximum shear gradient. E<sub>1</sub> and maximum shear also demonstrated ability to evaluate stiffness ratio through a strong correlation. This was in line with my expectations as the modeled tissue is primarily under compression. The softer inclusion of the low stiffness ratio models absorbed more load than stiffer neighbors (Figure 21). This was reflected in the mean strain curve (Figure 28). The success of the gradient mean ratio for E<sub>2</sub> and maximum shear can be attributed to the presence of high relative strain concentrations in the low stiffness models; the

high peak strains present yielded a steeper gradient from the surrounding strains. The eccentric positioning of the inclusion resulted in  $E_1$  and maximum shear mean ratio values higher than 1, weakening identification of an optimal model through the plot of stiffness ratio and mean ratio and my criteria. Despite this, all mean strain ratios correlated nearly perfectly with stiffness ratio, and exhibited clear qualitative differences on the strain maps.

VMR, lacunarity, and Moran's I did not improve evaluation of stiffness ratio over strain alone. Gradient mapping demonstrated some benefit through an identification of an overall maximum in gradient mean ratio in the optimal model, but did not improve correlation. For qualitative assessment, these heuristic maps did not clearly visualize differences not already seen in the strain maps alone, so they will not be shown in any further analysis.

These results are in line with previous studies that have examined spatial changes in cartilage material properties. Earlier studies first examining depth-dependency in cartilage have found compressive strains yielded the most information about spatially-dependent mechanical differences (Schinagl Robert et al., 2005). Studies examining spatially-dependent degradation of cartilage have used strain mapping with compressive and shear loading (Griffin et al., 2014; Yin, 2014) and solved the inverse model to determine depth-dependent moduli. They found compressive and shear strain concentrations were localized to regions of reduced material properties. However, my results disagree with previous efforts looking for correlates in MRI-based strain data and matrix constituents (Zevenbergen et al., 2018). I attribute this difference to the lack of ground truth material properties in the previous study. The displacement fields were generated through an idealized model; the resulting strains were directly dependent on the input material properties which made for a nearly perfect correlation.

Limitations of this study include analysis of strains and map heuristics in a limited ROI. Strain maps visualize through-thickness mechanics of the entire tissue. The results show changes in strain topography that extend beyond the defined ROIs. Excluding this topography along with peak strains and heuristics is losing valuable spatially-dependent information which may improve future efforts. Additionally, we assume a state of plane stress and compute only in-plane strains, a limitation of the model and the displacement-encoding method(Aletras et al., 1999; Chan & Neu, 2012) upon which it is based.

In conclusion, mean strain ratio can be used to evaluate material stiffness match in a tissue inclusion. MRI-based  $E_1$ ,  $E_2$ , and maximum shear strains are sensitive to these changes, and the ratio of the inclusion strains and bordering strains strongly correlated with stiffness ratio. Spatial analyses offered some quantitative benefit through gradient mapping, but there was no benefit from VMR, Lacunarity, or Moran's I.

## **4.4 Aim 2B Methods**

### **4.4.1 Rationale**

In Aim 2A, I found a clear relationship between the strains localized to an inclusion and the stiffness ratio, a measure I used to quantify material property match. I also noted qualitative differences in strain map topography based on the stiffness ratio. However, these observations were from images synthesized using a simple FE model of a cartilage explant. This model featured an inclusion of varying stiffness, but with a welded biphasic interface. This interface models perfect tissue integration which is observed only in intact, healthy cartilage.

As the cartilage repair methods advance, a vital consideration lies within interface mechanics(Ahsan & Sah, 1999; Shapiro et al., 1993; Wang et al., 2018). Current repair approaches often apply an adhesive to the interface of the repair tissue and healthy

cartilage(Khan, Gilbert, Singhrao, Duance, & Archer, 2008; Tew et al., 2001), which improves collagen deposition and repair strength(Dimicco & Sah, 2001; Moretti et al., 2005). However, a strong interface alone is not enough to create effective cartilage repair. We demonstrated that stiffness mismatch can create focal concentrations of high relative strains (Figure 21 & Figure 22). These high strain concentrations are associated with PG loss and collagen fibril damage(Brown et al., 2012; Eskelinen, Mononen, Venäläinen, Korhonen, & Tanska, 2019) and must be avoided for therapeutic repair. Strains associated both with material property changes and interface mechanics have been visualized for cartilage repair, but only *in vitro*, and by altering critical boundary conditions(Chung et al., 2015; Irwin et al., 2021; Wang et al., 2018). MRI-based strain mapping can be performed non-destructively and *in vivo*, and has visualized through thickness mechanics(Aletras et al., 1999), but has not been applied to cartilage repair.

I extended my analysis by building a cartilage repair FE model with improved physiological relevance. I then assessed the ability of MRI-based strains in evaluating cartilage repair interface mechanics. Mean strains of the interface were correlated with interface strength and repair stiffness match. Strain topography was analyzed using spatial analysis heuristics, and their mean values correlated with the same.

#### **4.4.2 Finite Element Models**

Previously published patient-specific geometry of the knee cartilage was imported(Rodriguez-Vila et al., 2017). Geometry of the medial femoral condyle and medial tibial plateau were remeshed and smoothed in Blender with 7 subtree divisions, preserving sharp edges (Figure 30). Cylindrical, full-depth defects 8mm in diameter were created on the medial femoral condyle where previous studies have demonstrated a high incidence of defects and high contact

stresses (Figure 31). Contract stresses are 10-15% higher on the medial side than those on the lateral, and cover 20% more area(Dong et al., 2011; Karataglis et al., 2006).

All models were then converted to tetrahedral meshes in Gmsh using Delaunay triangulation (Delaunay, 1934). The tetrahedral element size was 0.075mm, with 100 smoothing cycles. Meshes were exported into PreView for FE model setup.

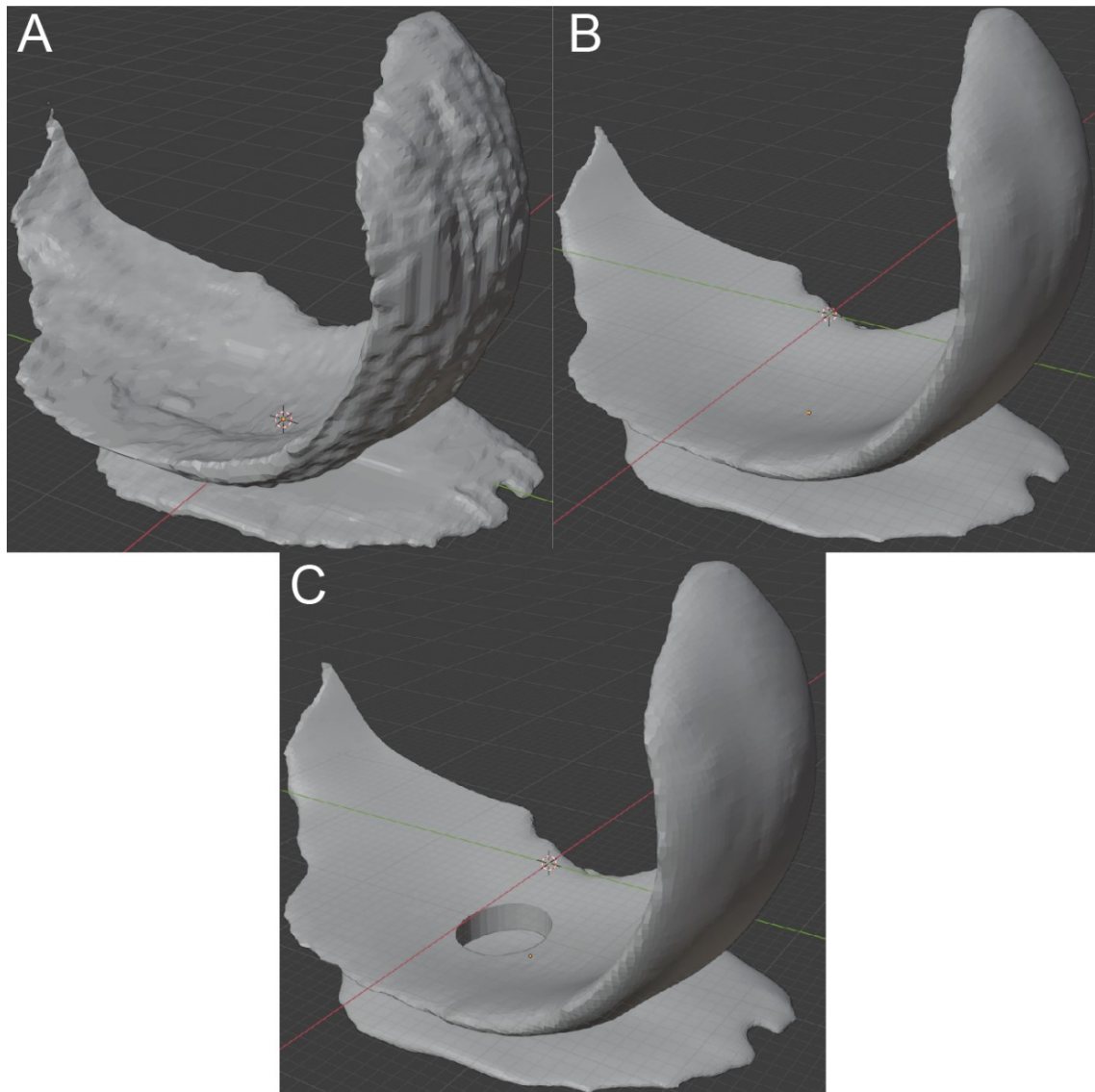


**Figure 30: Model remeshing, smoothing, and defect insertion. (A) The raw, unsmoothed geometry imported from (Rodriguez-Vila et al., 2017). (B) The remeshed and smoothed model. (C) The same model as (B) but with a full-depth defect.**

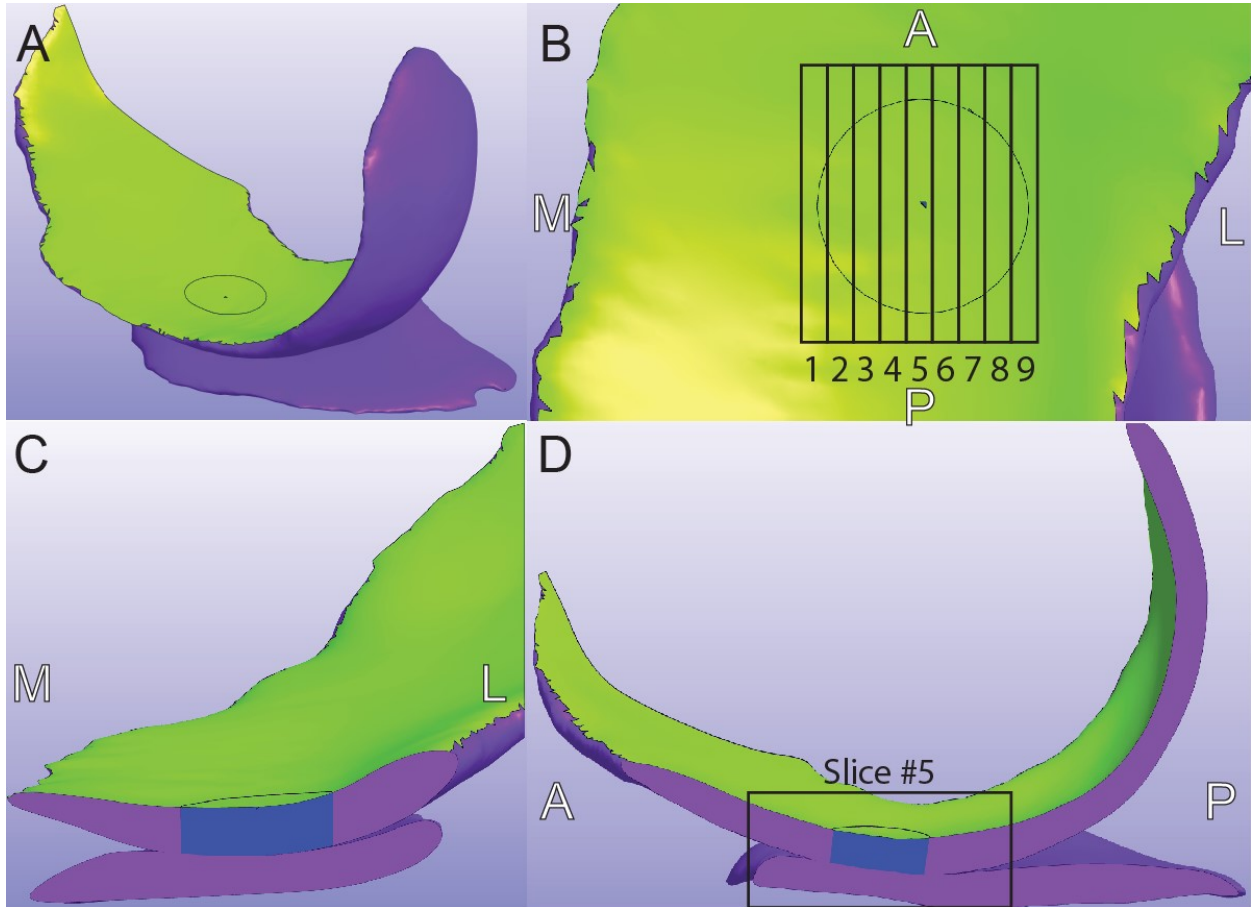


**Figure 31: (A) The patient-based FE model layout. A thin rigid body (lime green) models the femur, which applies load to the femoral and tibial cartilage (purple). (B) Positioning of 9 slices, done medial to lateral direction, relative to the defect. (C) Coronal slice of the model through the repair tissue center, shown as example only. (D) Zoomed-in sagittal slice, corresponding to slice #5 from (B). Tissue inclusion (blue) is centered at point of contact between healthy femoral and tibial tissue (purple). Slice interpolation was performed for entire combined femoral and tibial areas, but analysis was performed only within the indicated ROI.**

As previously discussed, the MRI-based strains I acquire lack the temporal resolution and SNR to meaningfully visualize changes in viscoelastic behavior (Figure 8, Figure 9, & Figure 10). Cyclic physiological loading will induce a strain plateau, which is ultimately better

representative of the state of the tissue I can visualize. Thus, this model represents a steady-state response of loading within the joint and will neglect viscoelasticity.

The healthy tissue was modeled as hyperelastic, isotropic, Neo-Hookean. As the load was distributed evenly over the tissue surface, the stiffness was chosen as the aggregate modulus under confined compression, 2MPa and a Poisson's ratio of 0.3(Mow & Guo, 2002). The repair tissue was modeled similarly, with an elastic stiffness ranging from 0.6MPa to 3MPa, stiffness ratio steps ranging from 30% to 150% in 10% increments, 13 total steps. Poisson's ratio was varied similarly, ranging from 0.06 to 0.45. Elements on the subchondral region of the femoral mesh were extracted and interpolated into triangular elements. The mesh here modeled the cartilage-bone interface of the femur (Figure 31A). A rigid body load in the negative Z direction of 0N was applied to the rigid body at  $t = 0$ , ramping up to 200N linearly over 0.1s, approximately 60% of half the patient body weight (Osteoarthritis Initiative ID 9932809\_00). Fixed boundary conditions were applied to the DZ layer of the tibial mesh, while the cartilage-bone interface of the femur was constrained to vertical motion. A sliding elastic contact interface was applied to the articulating surfaces of the femoral and tibial meshes with a coefficient of friction of 0.05. A sticky contact interface with variable maximum traction was applied to the interface of the femoral repair and healthy tissues. This traction force modeled the adhesive forces from bioglues or tissue integration in cartilage repair, contributing to interface strength. The maximum traction was varied from 0.001MPa up to 1000MPa, ranging from effectively no integration to integration exceeding material properties. The maximum traction was varied by one to half an order of magnitude for a total of 11 steps. Aggregate modulus and Poisson's ratio were varied together, but maximum traction was varied alone. Each combination of aggregate modulus and maximum traction resulted in a unique model, for a total of  $13 \times 11 = 143$  models

(Table 7). One last model was also generated using the intact geometry (Figure 30B) using the healthy-level values for aggregate modulus and Poisson’s ratio (Table 7). No interface was modeled in the intact model. Finally, the analysis was performed using 5 time points every 0.02s from 0 to 0.1s as performed by a BFGS, non-symmetric, steady-state solver in FEBio.

**Table 7: Parameters varied within repair tissue for FE model. Bolded values are considered healthy-level.**

<b>Property</b>	<b>Repair Tissue Values</b>												
<b>Aggregate Modulus (MPa)</b>	0.6	0.8	1.0	1.2	1.4	1.6	1.8	<b>2.0</b>	2.2	2.4	2.6	2.8	3.0
<b>Poisson's Ratio</b>	0.09	0.12	0.15	0.18	0.21	0.24	0.27	<b>0.3</b>	0.33	0.36	0.39	0.42	0.45
<b>Maximum Traction (MPa)</b>	0.001	0.01	0.05	0.1	0.5	1	5	10	50	100	<b>1000</b>		

#### **4.4.3 2D Slice Interpolation and Strain Calculation**

Transverse and axial element displacements were imported into MATLAB at the final timestep and interpolated into 9, 1mm thick 2D slices, centered on the repair site (Figure 31B). Centroid-weighted averaging was performed for the elements contained within each voxel. This was done as a computationally-inexpensive approximation for the averaging of proton signals in MRI. Interpolated displacements were injected with noise ( $\sigma = 0.0061\text{mm}$ ) and smoothed with a 5x5 Gaussian filter over 50 cycles (Figure A.12) (Figure 33). Principal and maximum shear strains were calculated using the maximum likelihood estimator(Chan, Neu, & Hull, 2009a; Geers et al., 1996)

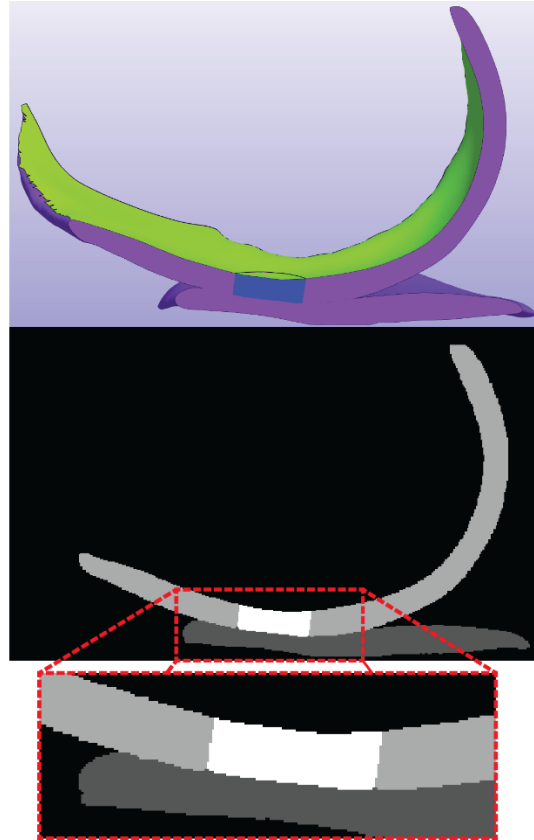


**Figure 32: Interpolation of FE model. Repair cartilage is white, femoral cartilage is light grey, and tibial cartilage is dark grey. Analysis region was scaled down from full image, and is shown in the highlighted area.**

#### **4.4.4 Spatial Analysis of Data**

Spatial analysis methods were the same as Aim 2A- mean strain, VMR, lacunarity, Moran's I, and gradient mapping. Here, I examined the mean values of the interface alone. The interface ROIs for each slice were considered an 8 pixel-thick region on the interface between the repair and the healthy tissue, 4 pixels on each side (Figure 34). These ROIs were generated using the input geometry. For the intact case, the ROI was overlaid from the 100%-1000MPa model, as an approximation.

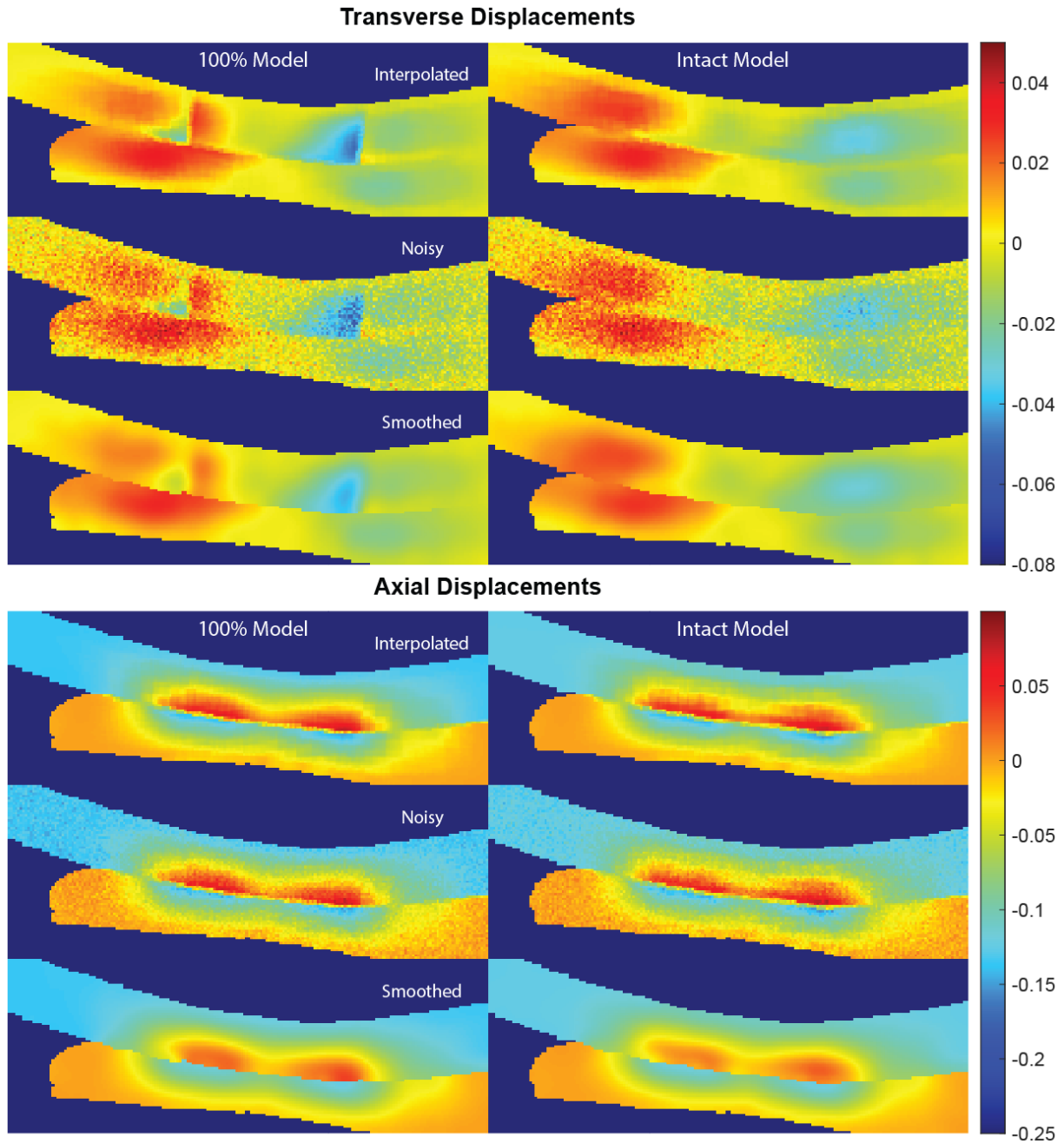


**Figure 33: Displacement processing. Interpolated displacements are injected with noise,  $\sigma = 0.0061\text{mm}$  (Figure A.7), and then smoothed. Representative transverse and axial displacements are shown on 100%-10MPa and Intact models.**

# Slices

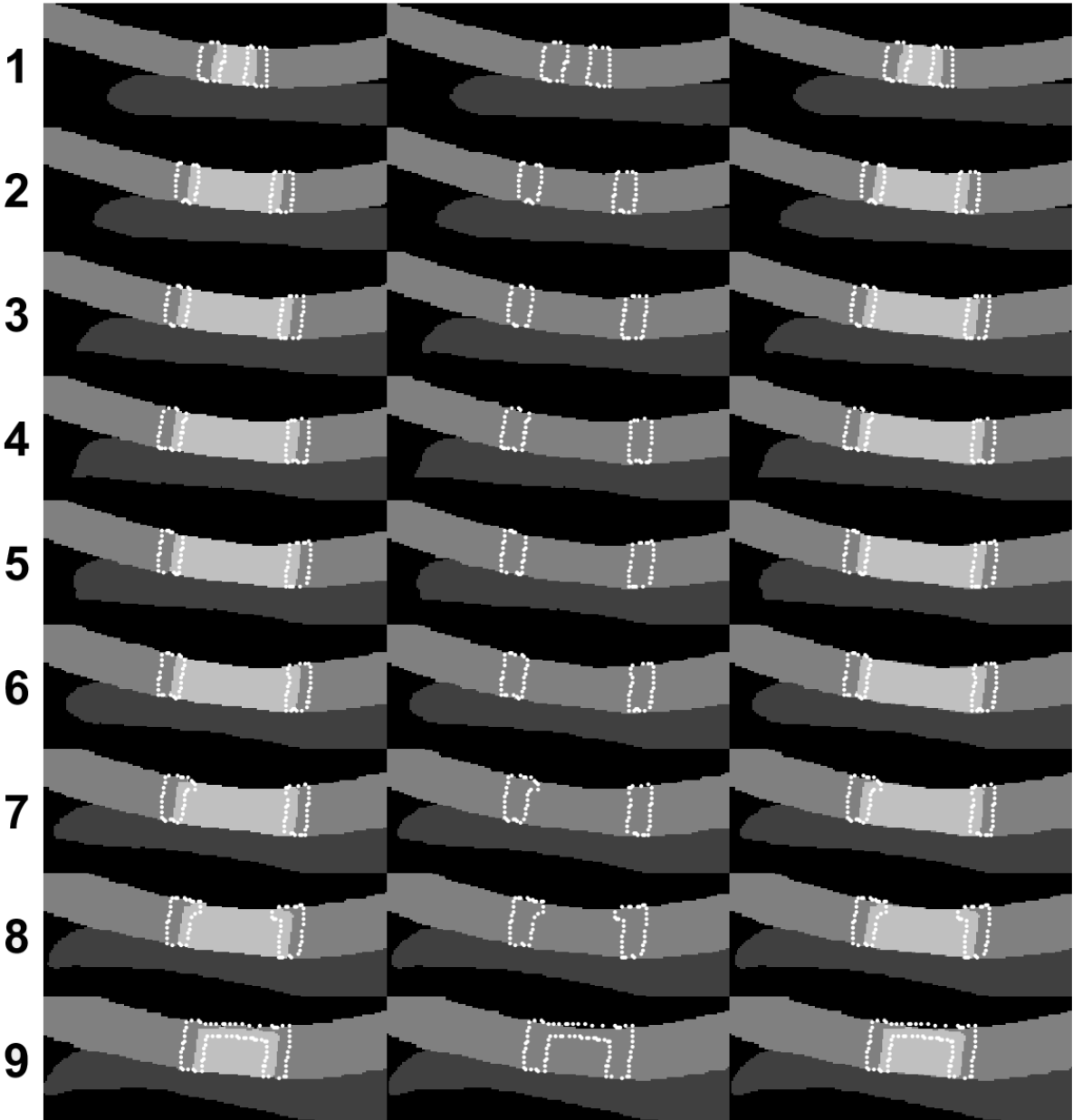


Figure 34: Masks and analysis ROIs shown for all slices of representative models. ROI comprises the region encompassed by white dotted lines, which overlaps the boundary between the repair cartilage (light grey) and healthy femoral cartilage (medium grey). Left column shows the 100% stiffness ratio-1000MPa model. Middle column shows the intact model, overlaid with the same ROI. Right column shows the intact model again, but overlaid with repair tissue from the 100%-1000MPa model and the same ROI. Invalid points resulting from this approximation were excluded from analysis.

Each strain and the spatial analyses heuristic was averaged from all ROIs of each model.

These values were correlated with either the stiffness ratio (30-150%) or the maximum traction

(0.001MPa to 1000MPa), and plotted. For all comparisons, the value of the intact model was also plotted as a straight horizontal line, to provide a baseline value for healthy-level repair.

The ability of the mean interface value to evaluate stiffness match or interface strength was assessed similarly as in Aim 2A. The optimal model had the closest mean value to that of the intact model.

For stiffness ratio, straight-line curves with a near-perfect correlation (absolute value 0.95 or higher) and an optimal model within close to the 100% model (ranging from 80%-120% stiffness) were considered successful evaluators of stiffness ratio. U-shaped mean ratio curves with optimal models approaching ranging from 80%-120% were also considered successful evaluators of material stiffness. This range was chosen as a conservative measure of successful stiffness recapitulation within TE construct studies(Beck et al., 2016; Raghunath et al., 2007; Woodfield et al., 2004; Xu et al., 2018).

## **4.5 Aim 2B Results**

### **4.5.1 Displacements**

Interface transverse displacements were dependent on the stiffness ratio (Figure 35). The 30% model experienced peaks along the interface of -0.029mm and 0.019mm within slices 5 and 6 as the stiffer healthy tissue pushed in on the soft repair tissue. The 100% model showed similar peaks of -0.028mm and 0.020mm, but spread across the interface. The 150% model experienced higher peaks of -0.078mm and 0.045mm due to the stiffer repair tissue pushing outward on the softer surrounding material. The intact model did not experience any particular concentration along the interface, and experienced lower peaks of -0.022mm and 0.017mm.

Axial displacements were also dependent on stiffness ratio, and exhibited the highest concentrations in 30% model (Figure 36), peaking at 0.078mm. These concentrations are present

at the point of contact between the femoral repair tissue and the tibial tissue. The 100% and 150% models show similar displacements of 0.039mm and 0.042mm respectively, but peaks were localized to slices 5-6 and 8-9 respectively. The intact model showed similar displacements to the 100% model, with a peak of 0.039mm in slice 5.

Models with variable maximum traction showed no observable changes across the full range. Transverse displacements (Figure 37) peaked at -0.029mm and 0.019mm in slice 5, higher than those of the intact model. Axial displacements (Figure 38) peaked at 0.042mm in slice 5, also higher than that of the intact model. The topography of the axial displacements was similar to that of the intact model in all models.

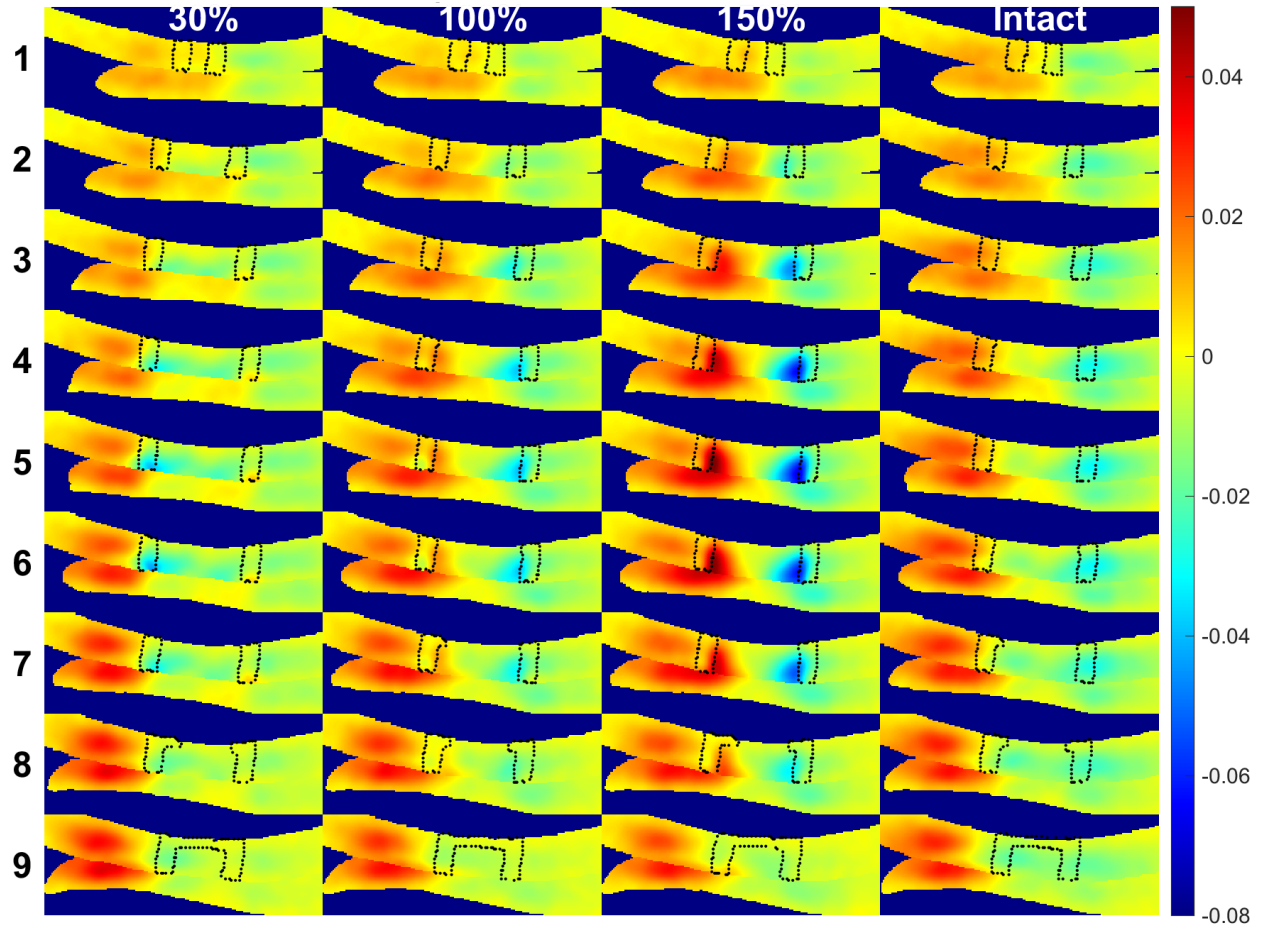


Figure 35: Representative transverse displacement maps of the stiffness ratio, all slices. Transverse displacements were concentrated along the healthy-repair interface (dotted black line) and increased with stiffness ratio.

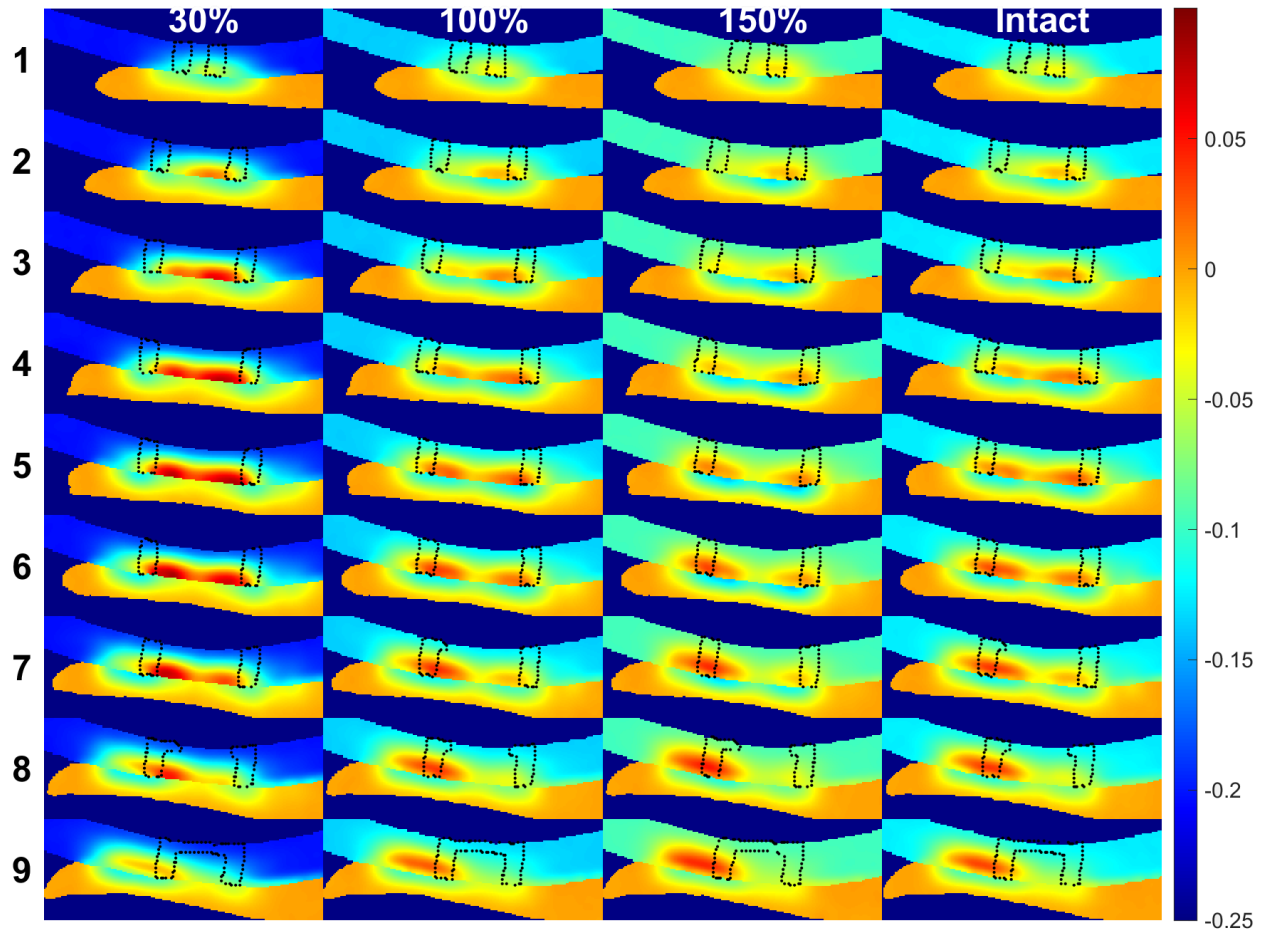


Figure 36: Representative axial displacement maps of the stiffness ratio, all slices. Axial displacements were concentrated on the point of contact between the femoral and tibial tissue, and decreased with stiffness ratio. Interface is shown as a dotted black line.

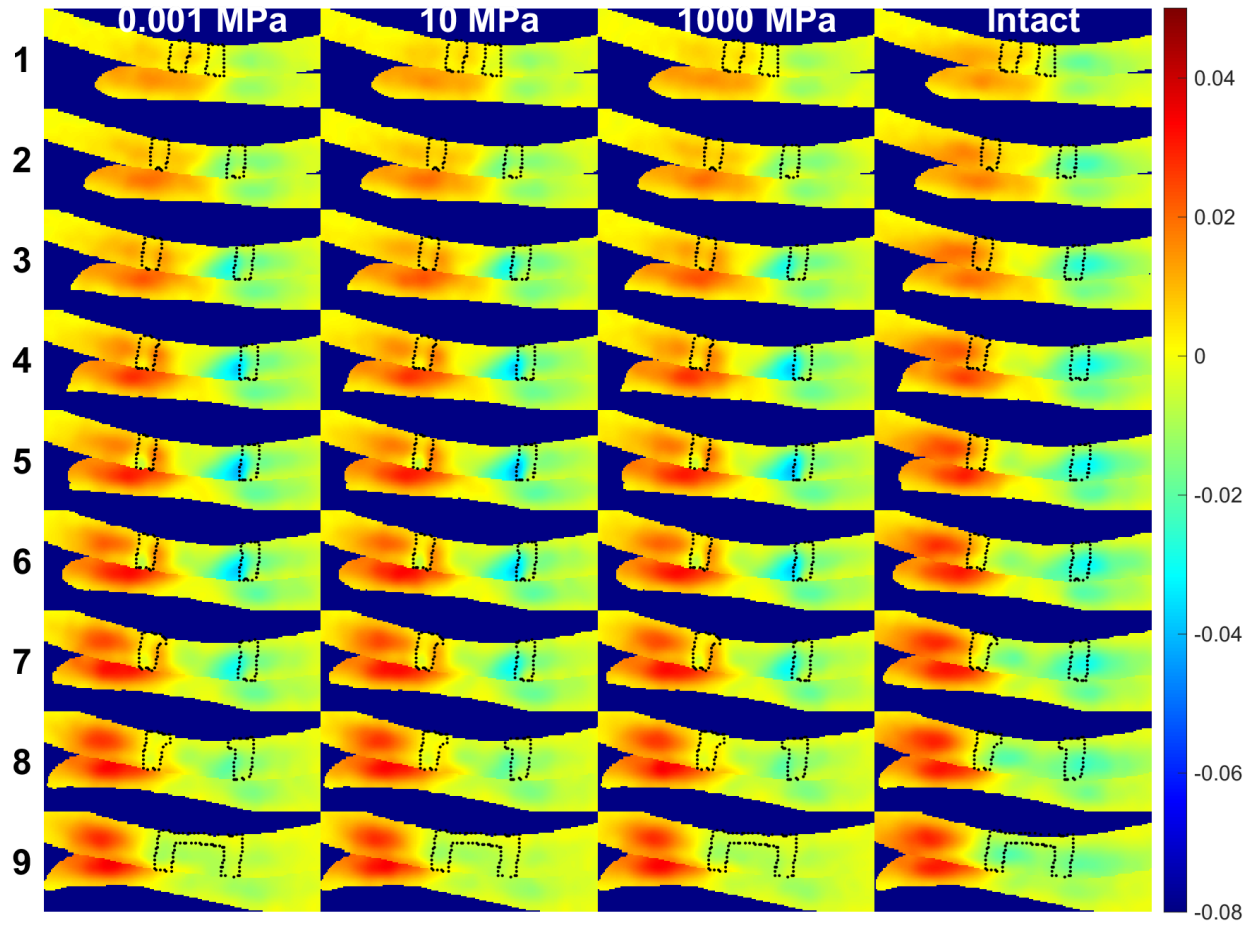


Figure 37: Representative transverse displacement maps of maximum traction, all slices. No changes were observed across the model range. Interface is shown as a dotted black line.

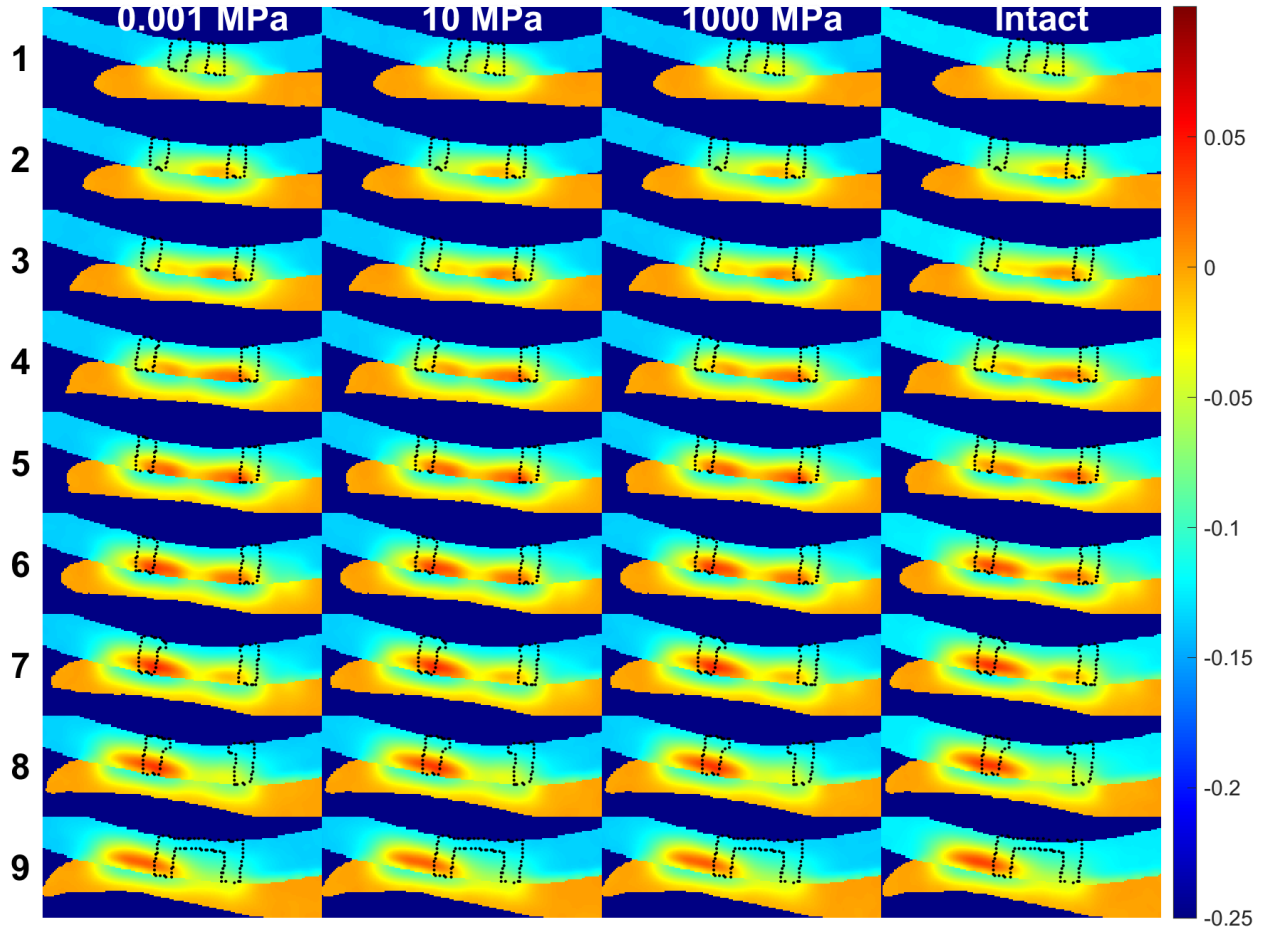


Figure 38: Representative axial displacement maps of maximum traction, all slices. No changes were observed across the model range. Interface is shown as a dotted black line.

#### 4.5.2 Strain Mapping of Repair Scenarios

The stiffness ratio altered  $E_1$  (Figure 39). The 30% model shows high tensile strains concentrated in the repair tissue and interface, in slices 3-7, peaking at 11.9% in slice 6. These concentrations are reduced in the 100% and 150% models to 7.1% and 6.6% respectively. However, there was a corresponding increase in the tibial strains, which rose from a peak of 5.3% in the 30% model to 7.4% in the 150% model. The intact model shows similar strain values to the 100% model with a peak of 6.7%, but more diffuse concentrations.

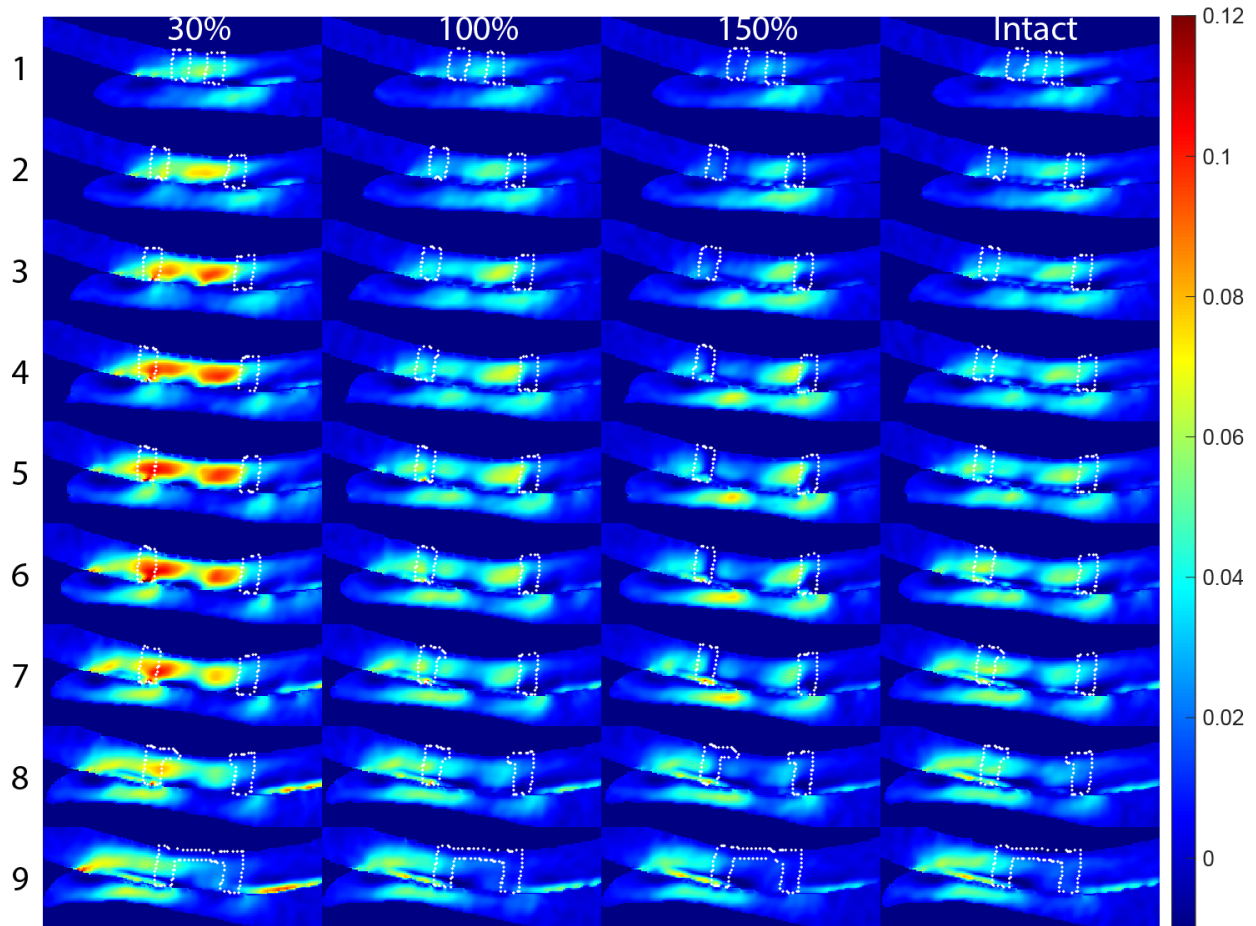
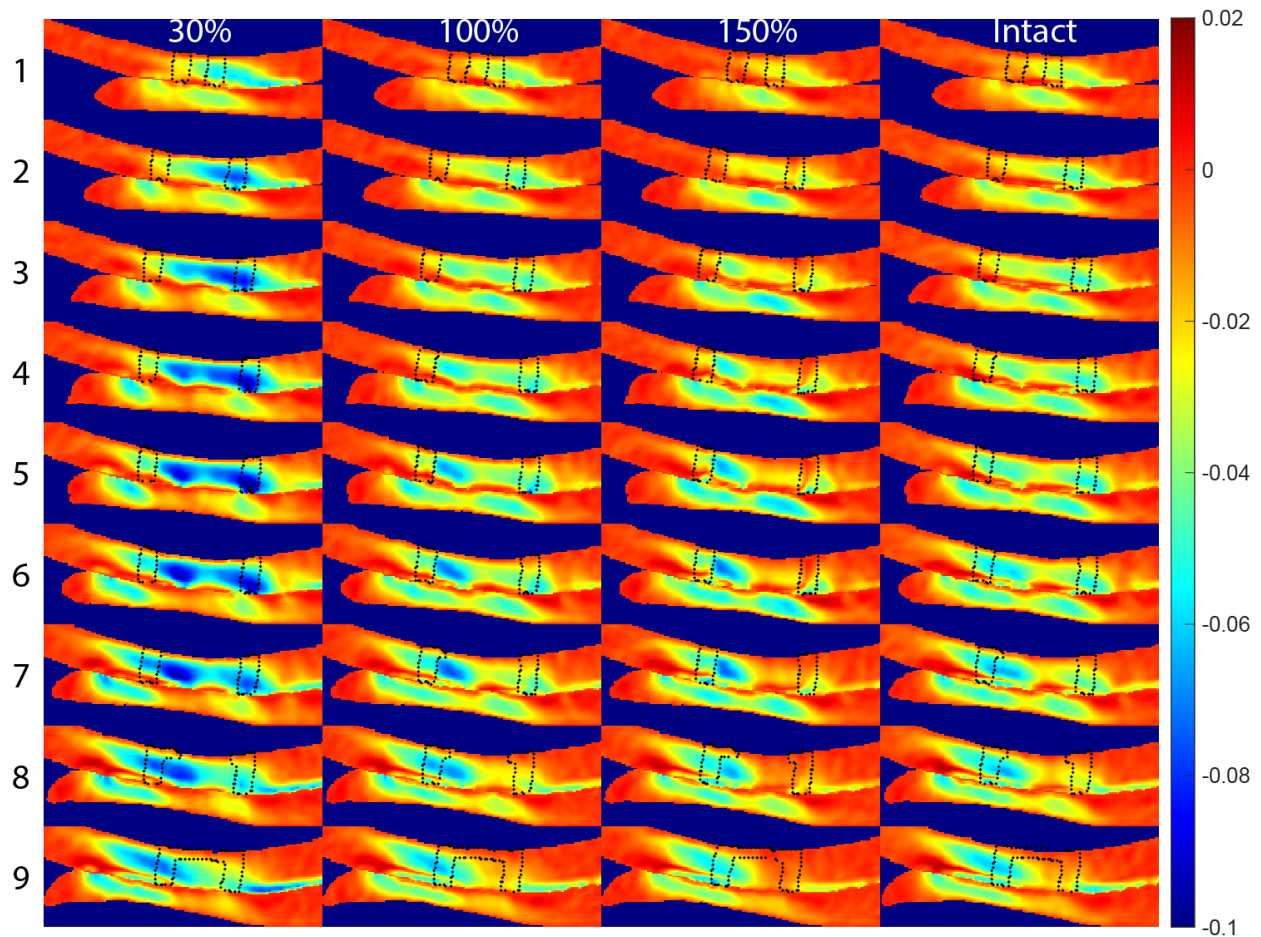


Figure 39:  $E_1$  of representative stiffness ratio models, all slices. Repair interface is shown as a dotted white line.

$E_2$  was also altered by the stiffness ratio (Figure 40). The 30% model experienced concentrated compressive strains in repair tissue and the interface in slices 2-8, peaking at -9.7% in slice 5. These concentrations are reduced as the stiffness ratio increases and shift to slice 7. The 100% and 150% model strain maps exhibit peaks of -7.2% and -6.8 respectively. The intact model shows topography similar to that of the 100% model, but with a more diffuse concentration and a lower peak of -5.92%



**Figure 40:  $E_2$  of representative stiffness ratio models, all slices. Repair interface is shown as a dotted black line.**

Maximum shear strain was also altered by the stiffness ratio (Figure 41). The 30% model exhibits shear strain concentrations in slices 2-8, peaking at 4.39% in the repair tissue and interface in slice 7. Increasing the stiffness ratio decreased the shear strain within the repair tissue; the 100% and 150% models yielded peak values of 2.9% and 2.8%. Similar to  $E_1$ , there was a corresponding increase in the tibial strains, with a peak of 2.9% in the 30% model to 3.2% in the 150% model. The intact model shear strain topography is similar to that of the 100% model; peaking at 2.9% and 2.8% respectively.

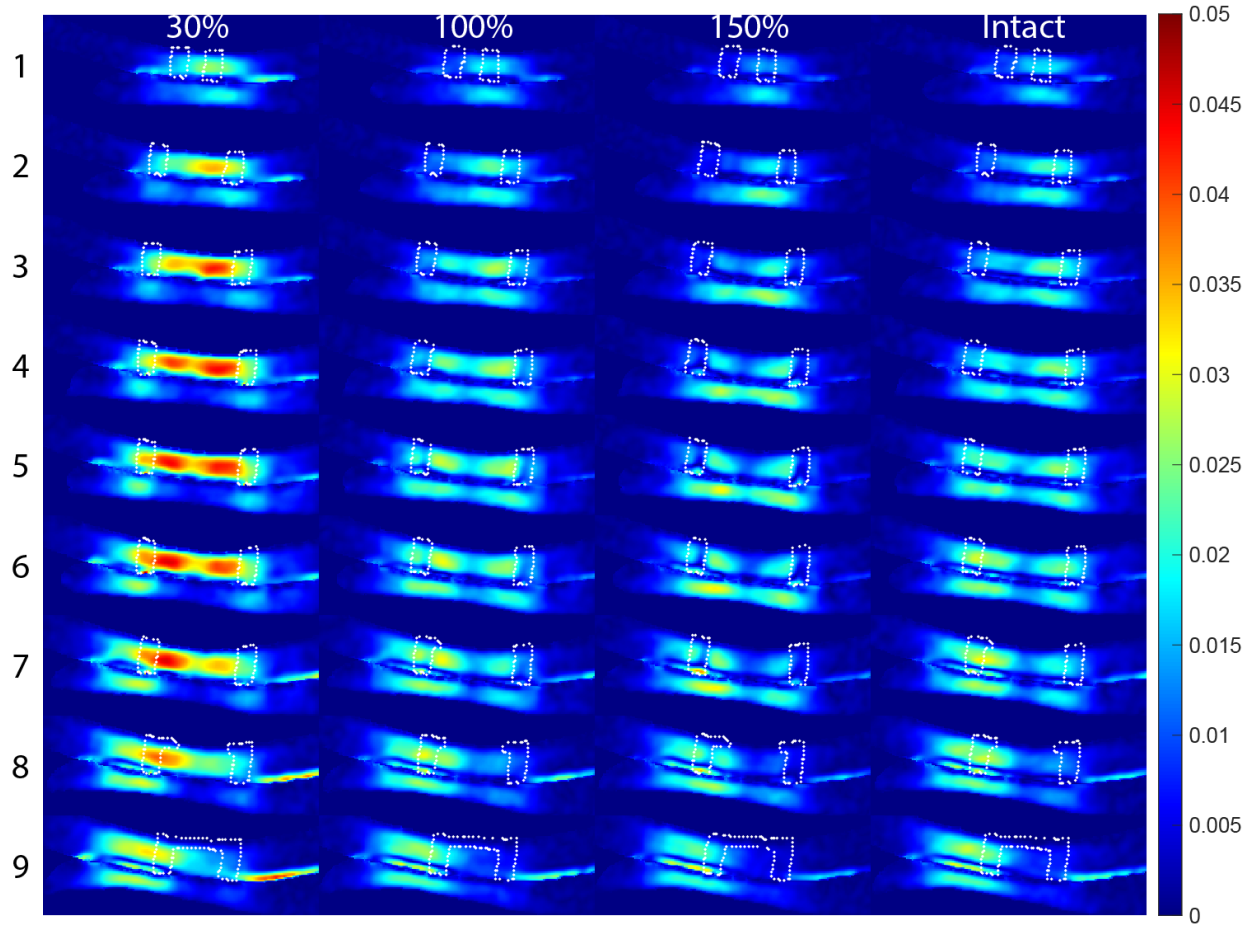


**Figure 41: Maximum shear strains of representative stiffness ratio models, all slices. Repair interface is shown as a dotted white line.**

There were no observable differences in any strain map from varying maximum traction (Figure 42, Figure 43, & Figure 44).

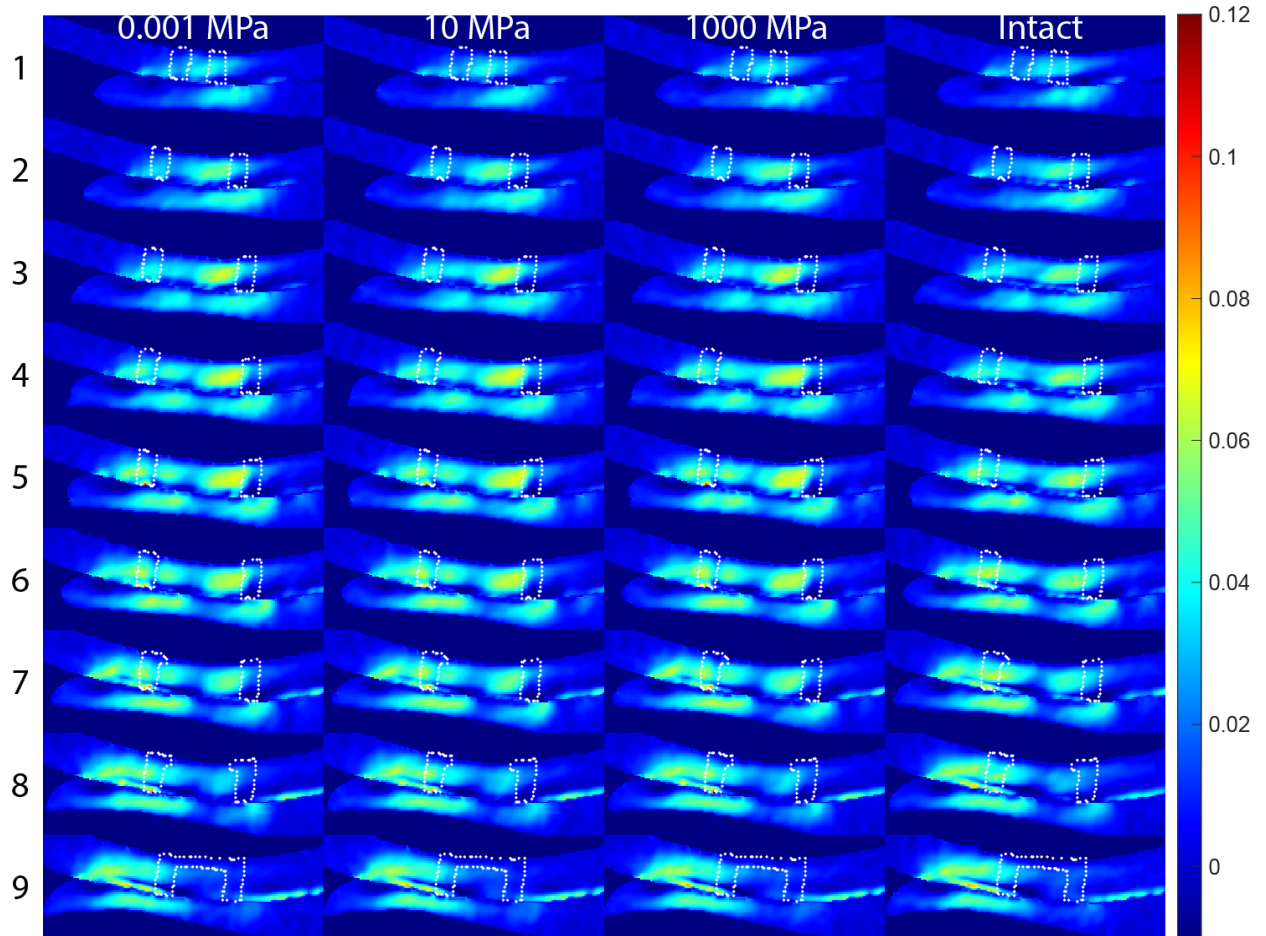


Figure 42:  $E_1$  of representative traction models, all slices. Repair interface is shown as a dotted white line.

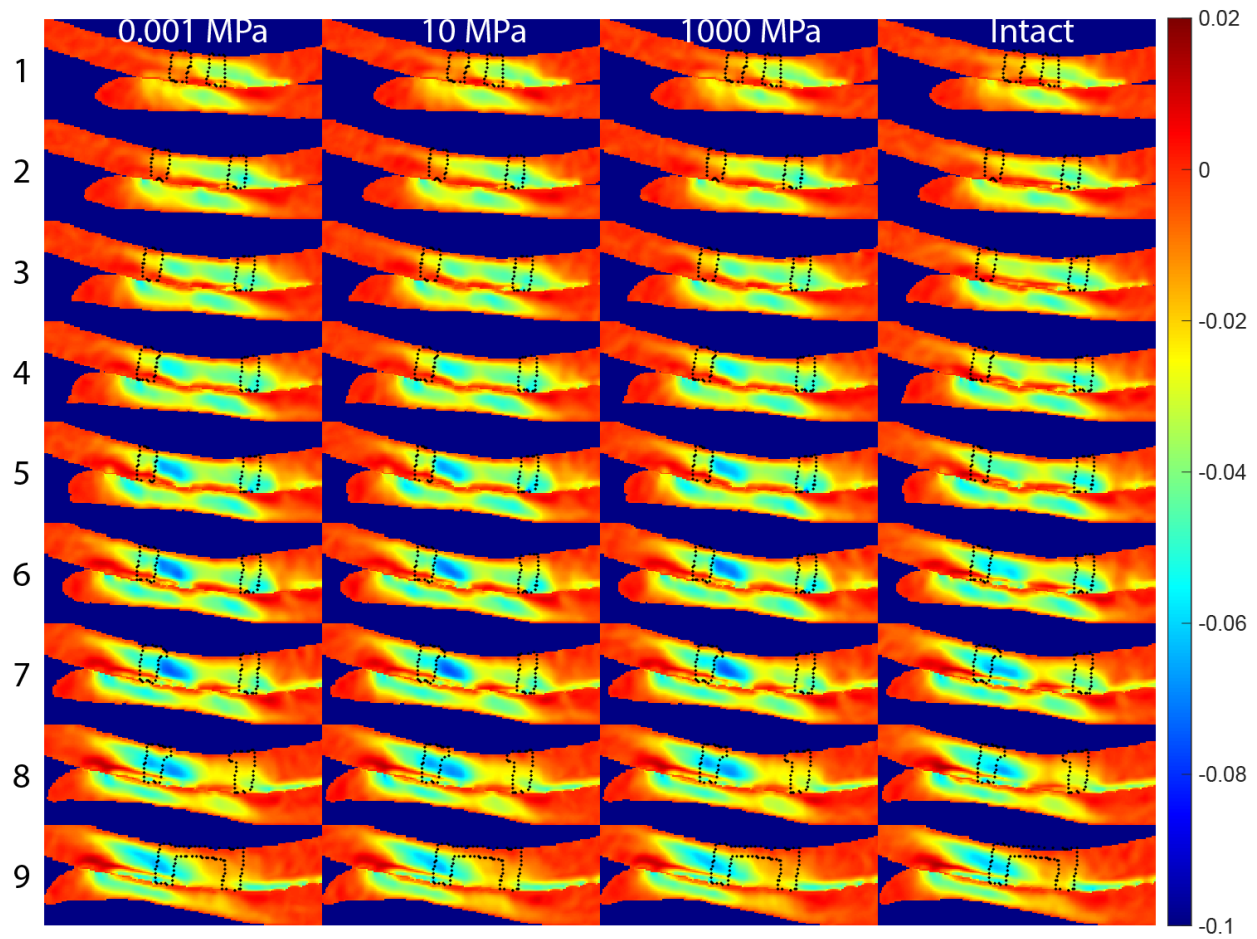


Figure 43:  $E_2$  of representative traction models, all slices. Repair interface is shown as a dotted white line.

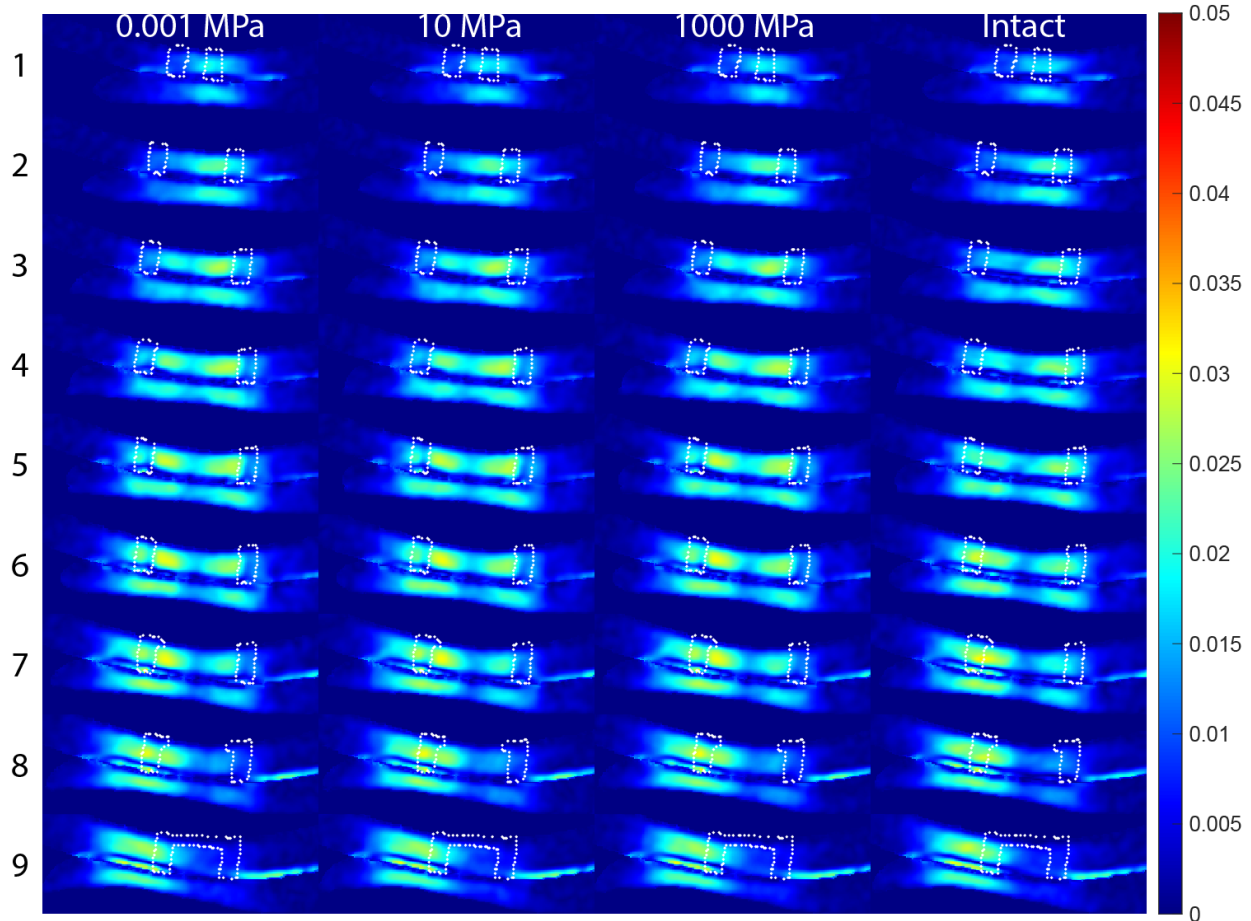


Figure 44: Maximum shear strains for representative traction models, all slices. Repair interface is shown as a dotted white line.

### 4.5.3 Correlation of Strain Maps and Spatial Analysis

Pearson's correlation was performed between the mean values and the stiffness ratio (Table 8) or maximum traction (Table 9). Mean values for  $E_1$  (Figure 45),  $E_2$  (Figure 46) and maximum shear (Figure 47) were also plotted against stiffness ratio. The same was done for maximum traction (Figure 48, Figure 49, & Figure 50). Each method's ability to evaluate stiffness ratio was determined from the results of these curves, based on the established criteria (Table 10). Assessment of interface strength was not performed due to model failure. No method

yielded any detectable change correlating with maximum traction (Figure 48, Figure 49, & Figure 50), and all correlations with it were weak (Table 9).

The successful evaluators of stiffness ratio varied for each strain.  $E_1$  and  $E_2$  mean strain and Moran's I were successful evaluators. For maximum shear, mean strain, VMR, Lacunarity, and Moran's I were all successful evaluators.

**Table 8: Pearson's correlation values for each strain type and spatial analysis heuristic VS stiffness ratio. Strong correlations are in bold orange and blue for negative and positive correlation, respectively. Color intensity fades with weaker correlation. Strong correlations were considered below -0.50 and above 0.50. Near perfect correlations were considered below -0.95 and above 0.95.**

Strain	Mean Strain	VMR	Lacunarity	Moran's I	Gradient
EP1	-0.992	-0.831	0.798	-0.998	-0.937
EP2	0.991	0.938	0.877	-0.998	-0.945
Max Shear	-0.992	-0.950	0.220	-0.996	-0.931

**Table 9: Pearson's correlation values for each strain type and spatial analysis heuristic VS maximum traction.**

Strain	Mean	VMR	LAC	Moran's	Grad
EP1	0.2969	0.4016	0.3796	-0.0059	0.2383
EP2	0.1796	-0.0147	-0.1229	0.0126	0.2617
Max Shear	0.1257	0.2828	0.1066	-0.1051	0.0558

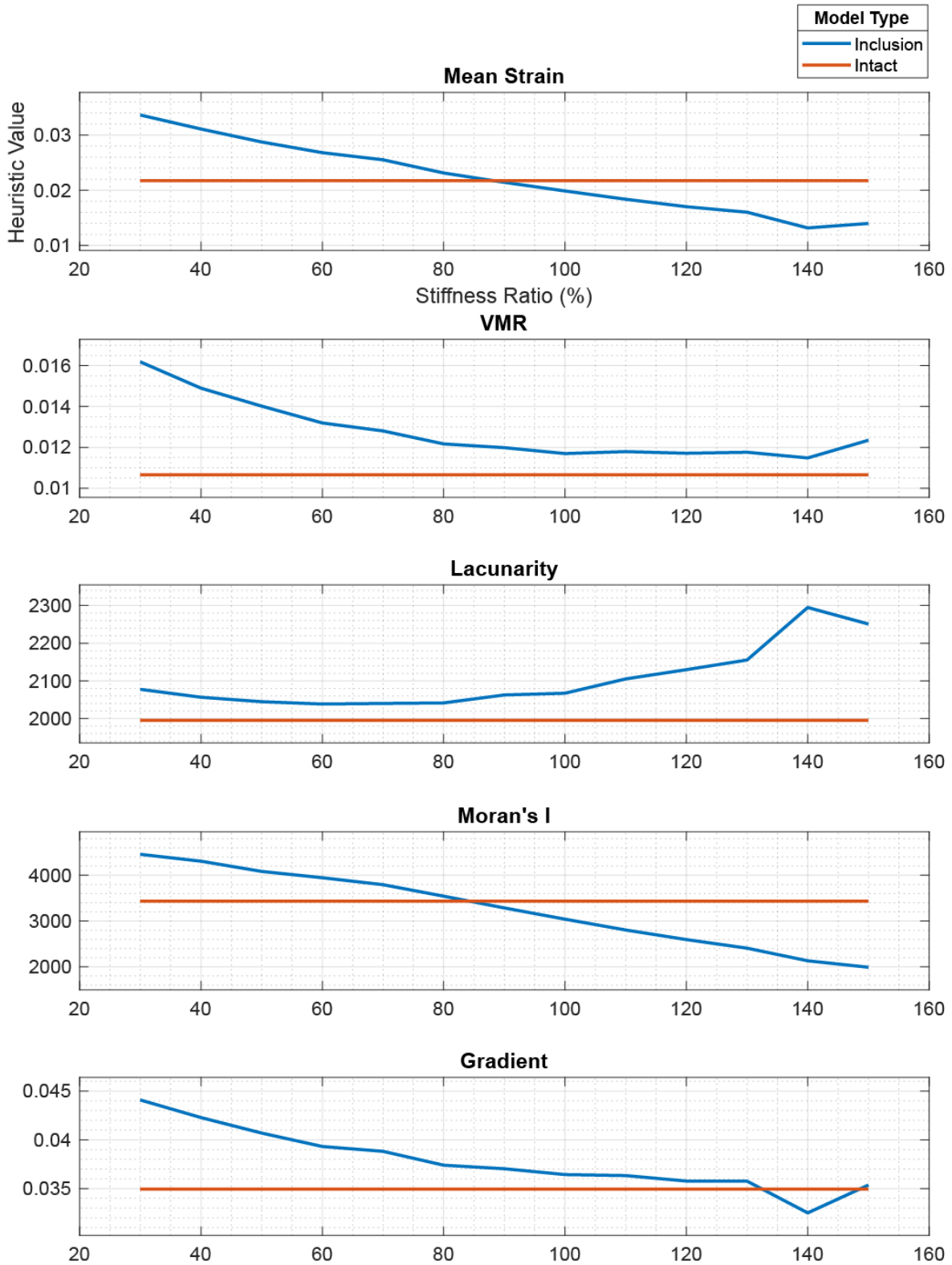


Figure 45: Plot of stiffness ratio against  $E_1$  mean heuristic values.

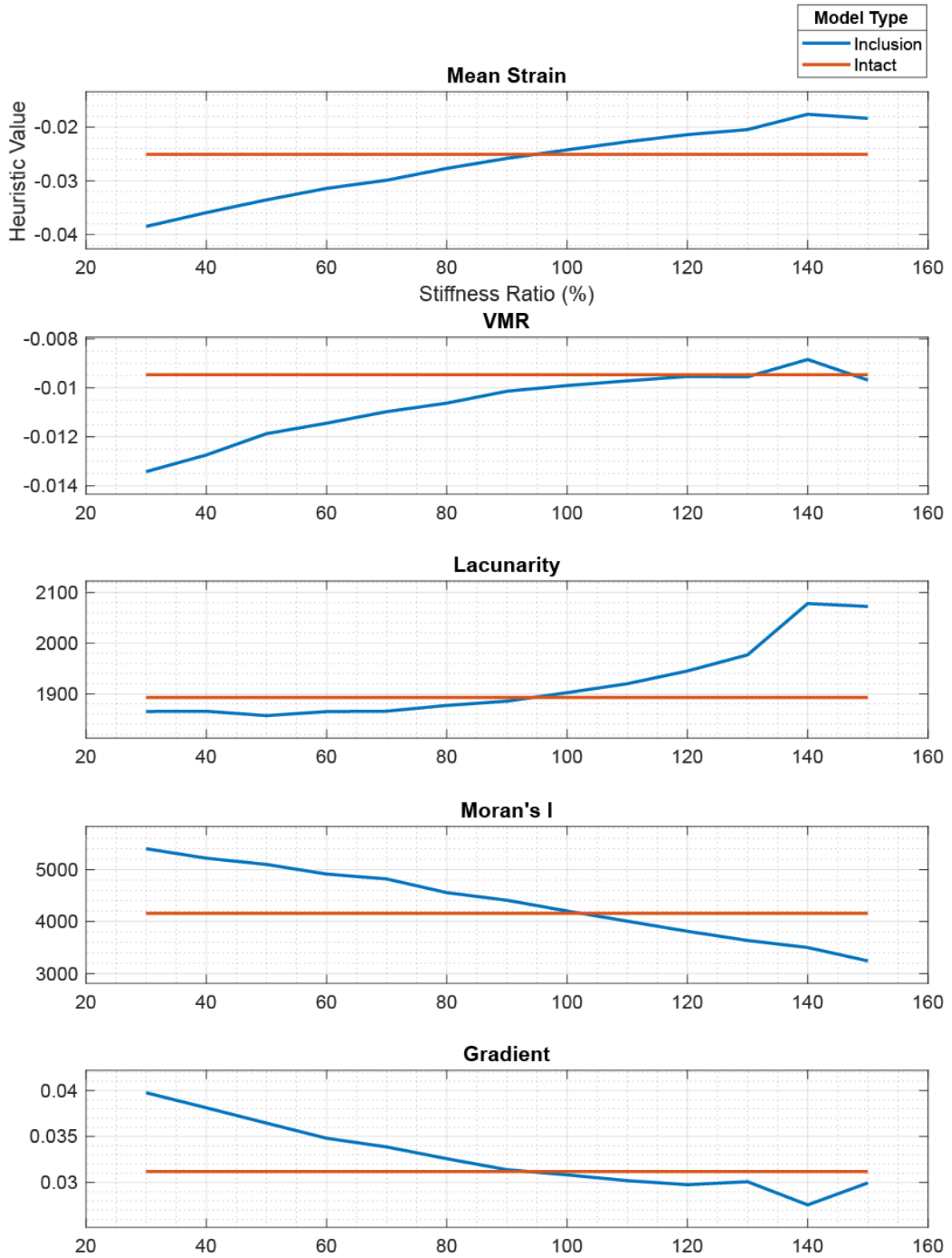


Figure 46: Plot of stiffness ratio against  $E_2$  mean heuristic values.

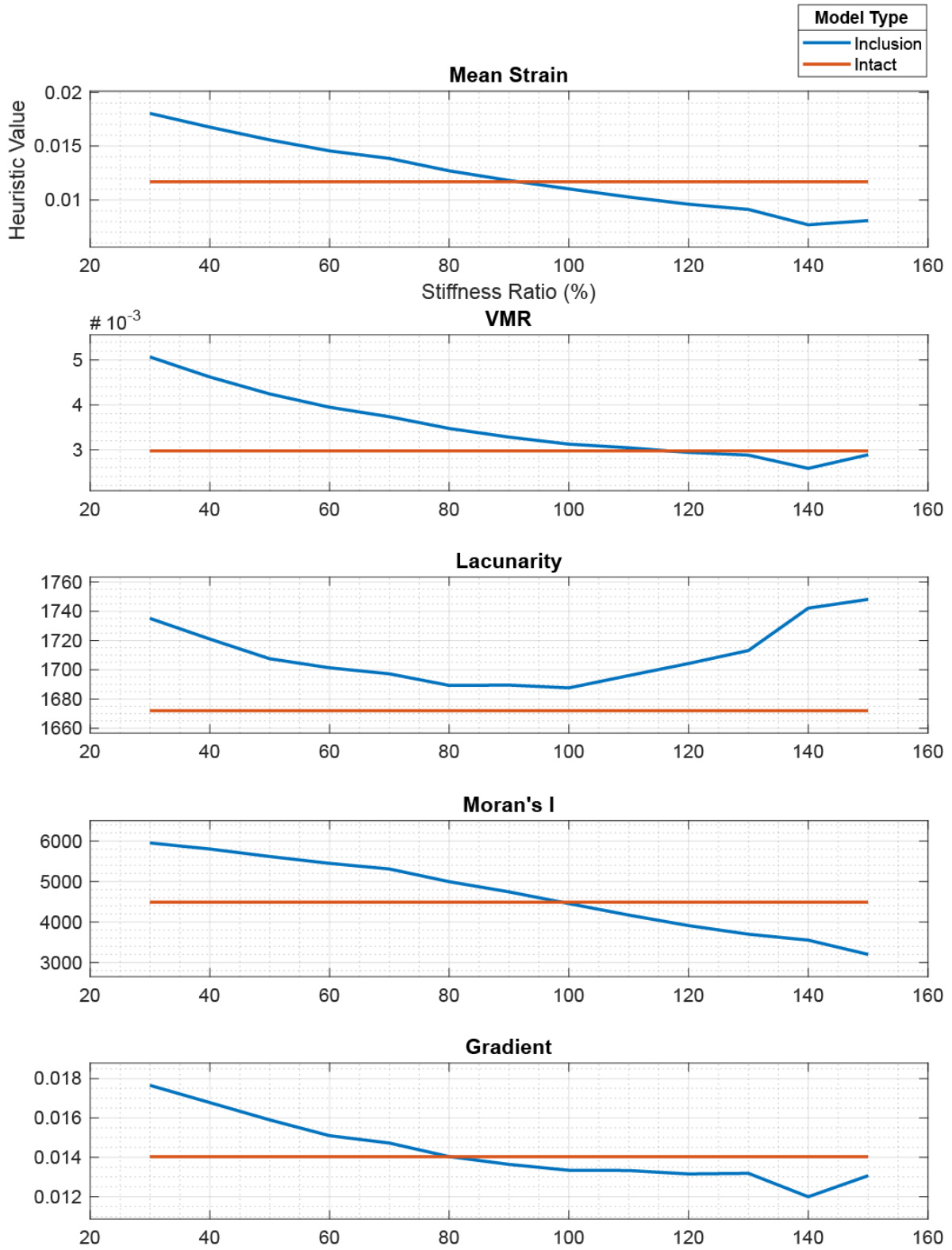


Figure 47: Plot of stiffness ratio against maximum shear heuristic values.

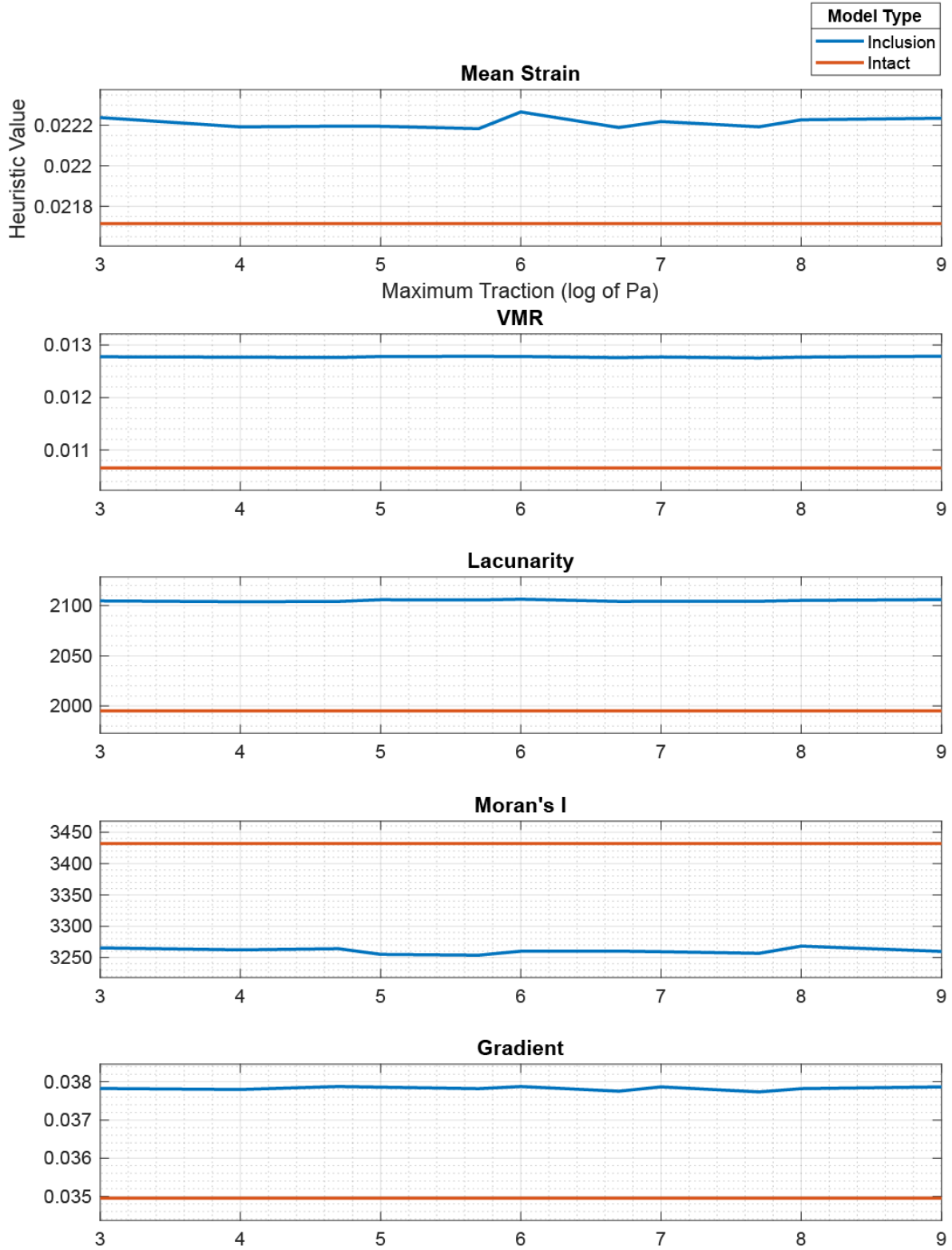


Figure 48: Logarithmic plot of maximum traction against  $E_1$  heuristic values.

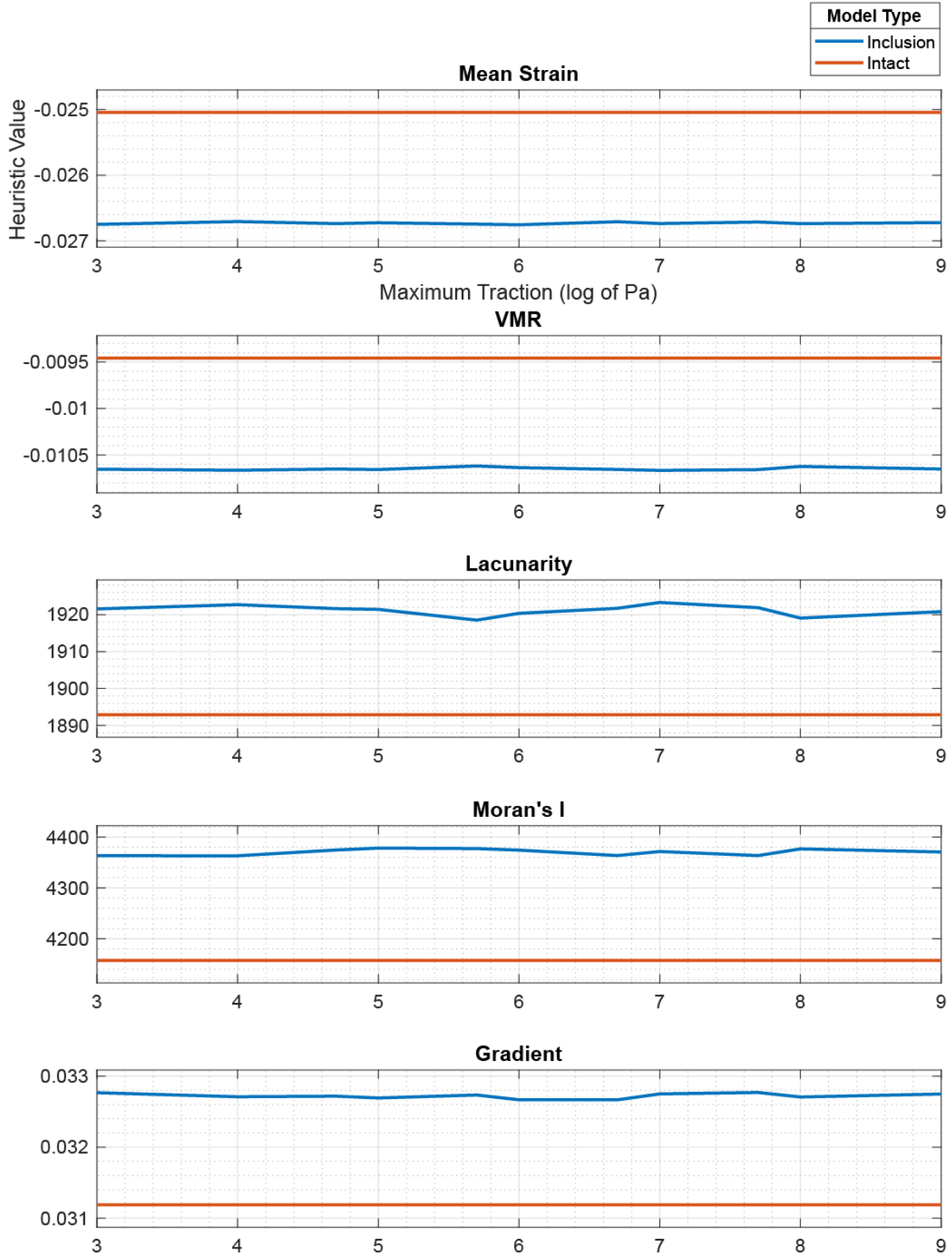
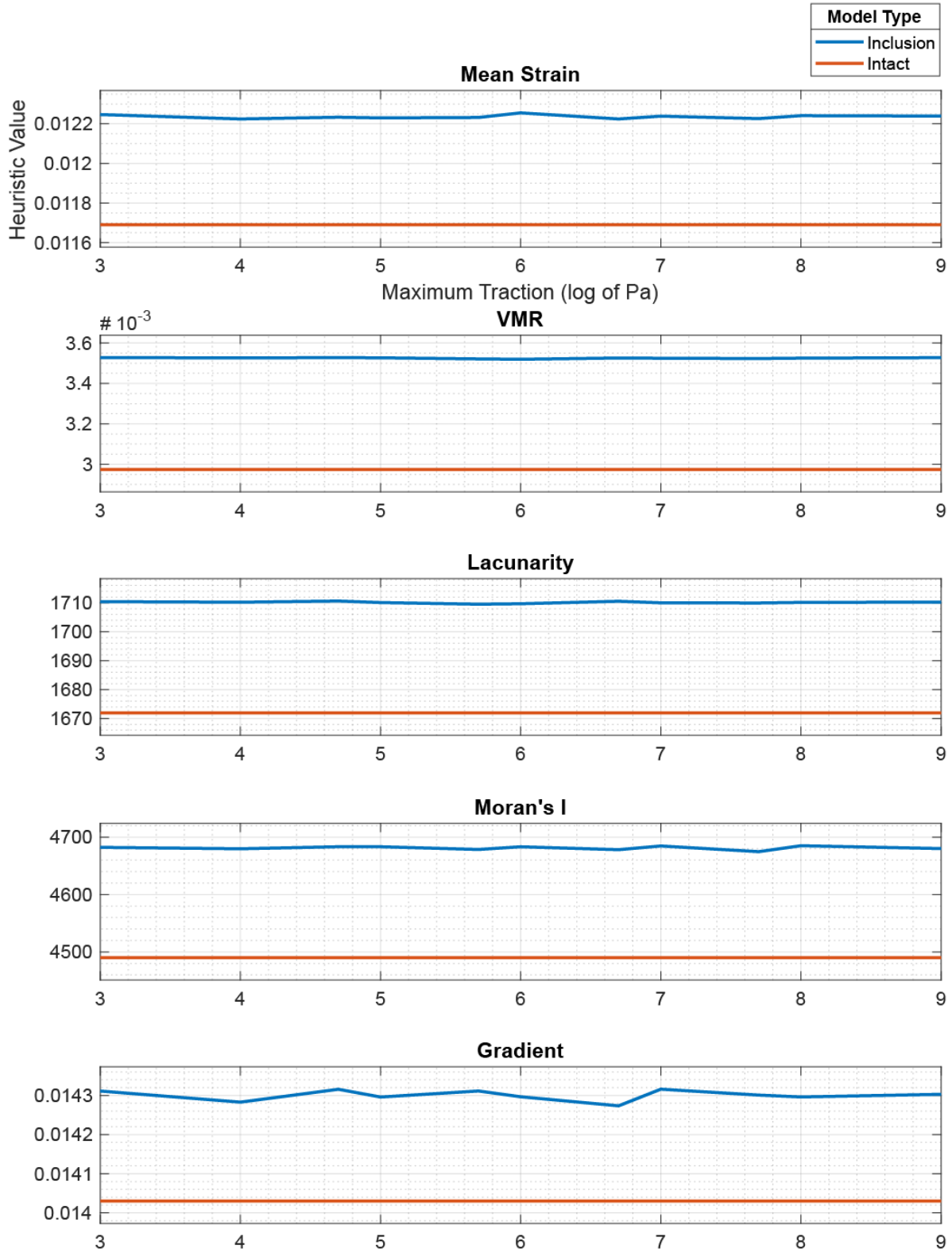


Figure 49: Logarithmic plot of maximum traction against  $E_2$  heuristic values.



**Figure 50: Logarithmic plot of maximum traction against maximum shear heuristic values.**  
**Table 10: The best evaluators of stiffness ratio highlighted in blue. The optimal model based on each curve was determined through a match with the intact model. If that optimal model was close to 100%, the true**

optimal repair case, and yielded a near-perfect linear correlation, then it was considered a successful evaluator. Methods meeting the first criteria but not the second are highlighted orange.

E1	Optimal Model	Proximity to 100%	Correlation
<b>Strain</b>	<b>90%</b>	<b>10%</b>	<b>-0.992</b>
VMR	-	-	-0.831
Lac	-	-	0.798
<b>Moran's I</b>	<b>80%</b>	<b>20%</b>	<b>-0.998</b>
Gradient	130%	30%	-0.937

E2	Optimal Model	Proximity to 100%	Correlation
<b>Strain</b>	<b>100%</b>	<b>0%</b>	<b>0.991</b>
VMR	120%	20%	0.938
Lac	90%	10%	0.877
<b>Moran's I</b>	<b>100%</b>	<b>0%</b>	<b>-0.998</b>
Gradient	90%	10%	-0.945

Max Shear	Optimal Model	Proximity to 100%	Correlation
<b>Strain</b>	<b>90%</b>	<b>10%</b>	<b>-0.992</b>
<b>VMR</b>	<b>120%</b>	<b>20%</b>	<b>-0.950</b>
<b>Lac</b>	<b>100%</b>	<b>0%</b>	<b>0.220</b>
<b>Moran's I</b>	<b>100%</b>	<b>0%</b>	<b>-0.996</b>
Gradient	80%	20%	-0.931

#### 4.6 Aim 2B Discussion

All interface mean strains and their Moran's I were successful evaluators of the stiffness ratio. VMR and lacunarity of maximum shear strains were also successful. This was expected as varying material properties of the repair tissue elicited altered strains along the repair interface. However, none of these methods successfully evaluated interface strength through changes in the maximum traction.

These results partially agree with studies that have examined spatially-dependent material property changes through strain mapping. Studies examining depth-dependent material properties have found compressive strains were highly correlated with spatially-dependent mechanical differences (Schinagl Robert et al., 2005). Studies examining localized cartilage

damage or digestion have found compressive and shear strain concentrations were localized to regions of reduced material properties(Griffin et al., 2014; Yin, 2014).

However, these results disagree with studies examining interface strains tied via adhesive forces. Other groups have found a clear reduction in interface shear strains through application of fibrin sealants in cartilage and adhesives in agarose gels(Irwin et al., 2021; Wang et al., 2018). These fibrin treatments have improved interface strength(Sennett et al., 2018) and agree with conventional wisdom that adhesives are a necessary component of repair.

I attribute this difference to my exclusion of viscoelastic behavior in the model, displacement interpolation, steady-state solver parameters, and the application of a purely compressive load onto a smooth surface. Exclusion of tissue viscoelasticity removes the time-dependent material properties observed in cartilage, thus reducing any transient shear strains that may appear during loading. The displacement interpolation effectively smooths element displacements as they are averaged per voxel, reducing the sensitivity of MRI-based acquisitions to sub-voxel scale strains. Furthermore, this loading applied is purely compressive, and only the vertical direction. The traction forces in the interface only resist shearing, but with a purely compressive load applied on axis, equally to all the tissue surrounding the repair, there is little shearing force concentrated in the interface. Physiologically, there is some shearing associated with articulation of the joint through the normal gait, which is why both clinicians and engineers apply some adhesive to the repair site(Adouni, Shirazi-Adl, & Shirazi, 2012; Lad et al., 2016; Taylor, C Bohm, Taylor, & Gross, 2011). Finally, I examine steady-state behavior by using a steady-state solver, and only examining the final timestep of the model. This simulates tissue that has settled into a loading plateau, eliminating the interface as a factor and forcing a greater dependence on the stiffness of the tissue. Manually examining every time point in the models

shows displacement and strain discontinuities across the interface, but only in the first or second time steps. By the last time point, the interface strains show smooth topography in all models. Additional validation is needed to ensure the sticky interface is appropriately modeling repair tissue interface.

Some limitations of this study include the above-mentioned single time-point, steady-state analysis and choice of pure compression. Additionally, some sacrifices were made in FE model accuracy during troubleshooting, such as exclusion of a meniscus. The implementation of the repair interface was not validated, and so its performance cannot be verified. Finally, all forms of analysis presented required prior knowledge of the exact location of the repair. While cases of poor local mechanical property match can be visualized by strain mapping alone, analysis of mean interface strains can only be done where the exact interface location is known. This limits these methods to the tissue engineering field for *in vitro* use or highly controlled *in vivo* experiments.

In conclusion, in-plane principal and maximum shear strains crossing the repair interface can be used to make assessments of repair stiffness ratio. All strains were able to identify optimal ranges and correlated nearly perfectly. Spatial analysis methods of interface strains were also able to assess stiffness ratio, but did not add information over strains alone. Due to problems in the analysis, interface strains could not make any assessment of interface strength. Future analysis must include all time points of a validated FE model for a full examination of interface strength, but steady-state analysis is sufficient for stiffness ratio evaluation.

## 5. DISCUSSION

### 5.1 Limitations and Shortcomings

One limitation of these studies lies in the removal of tissue viscoelasticity. As demonstrated in Aim 1A, MRI-based strains lack the requisite SNR and temporal resolution to fit a quasi-linear viscoelastic model. Furthermore, I employed MRI-based imaging methods that have only mapped tissue deformation after a quasi-steady state is attained using cyclic preconditioning. Tissue viscoelasticity contributes minimally to the resulting loading plateau, which is primarily dependent on matrix stiffness. While some previous work has demonstrated high temporal resolution MRI-based strains that are capable of visualizing transient shear strains in phantoms (Chan & Neu, 2012), I was unable to apply this methodology to my *in vitro* strain maps. Additionally, my models employ steady-state solvers, of which I only examine the final time point in my analysis. This eliminates any time-dependency within my results, which may be the key to advancing repair assessment methods.

My studies also employ strain mapping and heuristic analysis for specific ROIs. In Aims 1B, 2A, and 2B, I observe strain concentrations in every image and model, even cases of uniform material properties. It is clear that the strain maps are affected by geometry, as well as relative stiffness differences. While extreme cases of material mismatch show clear localized qualitative differences, geometric differences must be taken into account when analyzing strain maps. My ROIs are generated by input geometry, but many imaging studies determine their ROIs by a combination of visual inspection and landmarks. Localizing the ROI in this way requires some level of prior knowledge about the key features of the tissue. As a result, if strain maps are being

used to assess the cartilage repair interface or visualize inclusions, this requirement limits their use to *in vitro* or *in vivo* work within the tissue engineering field.

## **5.2 Improvements and Potential Directions**

The first improvements lie within my MRI acquisition and loading system. As seen in Table 2, my observed multi-frame SNR is poor compared to previous studies (Chan & Neu, 2012; Hunold et al., 2004; Welsch et al., 2011) and my own phantom images. Increasing the number of averages while decreasing TE/TR to minimum allowable levels by the system gradient can improve SNR. This increases scan time, which results in higher study costs and risks tissue damage. However, tissue damage can be reduced by decreasing the applied strain rate, which in turn decreases the requisite force. By decreasing the strain rate, I also lengthen the time between the application of load on the tissue, and the attainment of the loading plateau—allowing for the insertion of more frames. While full-depth viscoelastic parameter estimation is virtually impossible with current MRI technology, these improvements in SNR and temporal resolution will be critical in enhancing my analysis.

There are several improvements that could be made to improve the physiological relevance of my models and resulting strain maps. Starting with the material properties of the models, viscoelasticity must be considered. While some studies have replicated physiological behavior using isotropic, neo-Hookean material properties (Dong et al., 2011), others demonstrate the need for fibril-reinforced poroelasticity (Halonen, Mononen, Jurvelin, Töyräs, & Korhonen, 2013; Halonen et al., 2014). These studies have shown that mean strains can be approximated using isotropic, elastic properties, depth and spatially-dependent strains only appear when depth-dependent material properties are implemented. Future simulations will implement these changes when examining through-thickness behavior.

In addition to material properties, the model can be improved with the inclusion of the meniscus, which was originally excluded due to technical constraints. Previous *in silico* studies have shown peak contact stresses are nearly doubled with axial loading in the absence of a meniscus, which is likely to change strain distribution throughout the joint (Vaziri, Nayeb-Hashemi, Singh, & Tafti, 2008). A significant portion of my analysis focuses on examining the localization of strain concentrations near repair tissue. The exclusion of a meniscus is known to alter contact stresses (McDermott & Amis, 2006), which is certain to affect the resulting strain topography. Future simulations will include the geometry of the meniscus, modeled as a fibril-reinforced, poroelastic material (Vaziri et al., 2008).

The remaining improvements to my studies lie within my analysis methods. Aim 1B demonstrated any link between spatially-dependent strains and depth-dependent material properties across entire strain maps, but only using discrete cells. Aims 2A and 2B focused on specific ROIs, correlating changes within those regions with model parameters. A combined approach is needed, analyzing the entire map of strains, but also quantifying their locations. Previous studies have explored histogram-like plots to measure changes in strain concentration as a percentage of total depth and width (Irwin et al., 2021). However, few studies consider spatially-dependent as well as time-dependent effects in their analysis. If adjacent tissues exhibit differing viscoelastic responses to loading, transient shear strains may appear that prevent long-term tissue integration (Ahsan & Sah, 1999; Shapiro et al., 1993), even if the overall stiffness and strain are the same under a loading plateau. Therefore, my analysis should be expanded in the following two ways; to process all model time points to cover any time-dependent effects, and measure strain concentrations as a continuous function of location, rather than by discrete cells or simple qualitative observation.

## **5.3 Significance and Impact**

### **5.3.1 Study Significance**

In these studies, I present MRI-based strains as an assessment method for detecting spatially-dependent changes in through-thickness mechanics. In Aim 1B, I assess the value of a strain distribution in detecting, spatially-dependent differences in material properties. In Aim 2A, I show a strong correlation between the mean strain ratios of an inclusion and the stiffness ratio. In Aim 2B, I show the strong correlation between mean strain and stiffness ratio is maintained in a physiologically-relevant repair model. Finally, in Aims 2A and 2B, I also visualize the altered strain topography associated with localized changes in material properties. These findings are significant in that they highlight the value of visualizing through-thickness mechanics in assessing cartilage repair. Using MRI-based strains in this way enables non-destructive visualization of tissue behavior, correlates to relative material properties, and improves *in vivo* translatability of *in vitro* TE repair strategies.

### **5.3.2 Tissue Engineering Impact**

As previously stated, the TE *in vitro* methods are advancing toward construct-based cartilage repair, but without the necessary tools for repair assessment. Through thickness mechanical assessment is neglected in favor of destructive mechanical tests or push-out tests(Olvera et al., 2015). These methods reduce information about cartilage repair down to singleton measurements and cannot detect spatially-dependent material changes. Some tissue engineering studies have measured depth-dependent properties via traditional mechanical testing(Schinagl Robert et al., 2005). However, these methods are destructive and extremely laborious, adding time and cost to each study. Traditional methods of imaging through thickness mechanics are destructive as well and alter boundary conditions(Gilchrist et al., 2007).

Visualizing through-thickness mechanics via non-destructive, non-invasive imaging can improve throughput for *in vitro* studies and reduce costs associated with longitudinal tissue studies. MRI-based strains can provide this information and should be considered for *in vitro* TE-based cartilage repair assessment.

## **5.4 Future Work**

### **5.4.1 Phantom & Repair Model Validation**

Immediate future work requires validation of my simulated MRI-based strains with phantoms and a simple explant repair model. Previous research has demonstrated Sylgard phantoms with tunable stiffness (Palchesko, Zhang, Sun, & Feinberg, 2012) which can be used to create a phantom with a variable stiffness ratio inclusion. MRI-based strains can be acquired from the phantom to confirm the relationship between mean strain ratio and the stiffness ratio. Additionally, I can create a simple explant repair model by removing cylindrical plug of a tissue from a larger explant and either reinserting it as is or with an agarose plug, with and without fibrin glue. I can acquire the same strain maps and examine the relationship between interface strains and material property match, and interface strength.

### **5.4.2 Spatiotemporal Strain Analysis of Cartilage Repair**

Improved analysis methods can further elucidate altered strain patterns in cartilage repair. By implementing continuous plots of mean principal and maximum shear strains by percentage of total depth and width, I can create a quantitative strain profile for an entire strain map (Irwin et al., 2021). Furthermore, the analysis can be improved by further optimizing SNR in a cine-acquisition to acquire multiple frames during cyclic loading. Then, we can construct an *in vitro* repair model using cartilage-on-cartilage contact. Large explants can be left intact, have removed tissue reinserted, or be repaired by simple agarose constructs. With these

improvements, time-dependent, through-thickness behavior associated with successful cartilage repair can be better assessed.

## 6. CONCLUSION

I applied MRI-based strain mapping, real and simulated, to applications of cartilage repair assessment. First, I assessed the ability of multi-frame acquisitions in MRI to fitting depth-dependent viscoelastic parameters in a quasi-linear viscoelastic model. The requisite SNR and temporal resolution needed to perform such a parameter estimation was far beyond what is possible.

Second, I assessed the ability of strain distribution and mean strain in evaluating depth-dependent material properties acquired from depth-dependent agarose phantoms. Mean strains proved more sensitive to depth-dependent material property differences than strain distribution, and were considered the better estimator of material properties for the remaining studies.

Third, I implemented texture-based spatial analysis methods and applied them to simulated strain maps of a tissue inclusion. The mean ratio of all strains strongly correlated with the stiffness ratio, a measure of material property match, with compressive strains being the best evaluator. Gradient mapping also demonstrated some ability to evaluate stiffness ratio, but not VMR, lacunarity, or Moran's I.

Finally, I applied the same analysis methods to simulated strains derived from a cartilage repair interface model. This model featured variable stiffness ratio as well as variable interface strength. I found that all interface strains strongly correlated with and evaluated the stiffness ratio, but could not assess interface strength due to analysis limitations. Spatial analysis of compressive and maximum shear strains also evaluated the stiffness ratio, but did not improve correlation.

Overall, MRI-based strains were highly predictive of material property match through the mean strain ratio and mean interface strains, and can be used to evaluate material property match in cartilage repair.

## REFERENCES

- Adouni, M., Shirazi-Adl, A., & Shirazi, R. (2012). Computational biodynamics of human knee joint in gait: From muscle forces to cartilage stresses. *Journal of Biomechanics*, *45*(12), 2149-2156. doi:10.1016/j.jbiomech.2012.05.040
- Ahsan, T., & Sah, R. L. (1999). Biomechanics of integrative cartilage repair. *Osteoarthritis Cartilage*, *7*(1), 29-40. doi:10.1053/joca.1998.0160
- Ahsanizadeh, S., & Li, L. (2015). Strain-rate-dependent non-linear tensile properties of the superficial zone of articular cartilage. *Connective Tissue Research*, *56*(6), 469-476. doi:10.3109/03008207.2015.1066779
- Ainola, M., Tomaszewski, W., Ostrowska, B., Wesolowska, E., Wagner, H. D., Swieszkowski, W., . . . Konttinen, Y. T. (2015). A bioactive hybrid three-dimensional tissue-engineering construct for cartilage repair. *Journal of Biomaterials Applications*, *30*(6), 873-885. doi:10.1177/0885328215604069
- Aletras, A. H., Ding, S., Balaban, R. S., & Wen, H. (1999). DENSE: displacement encoding with stimulated echoes in cardiac functional MRI. *Journal of Magnetic Resonance*, *137*(1), 247-252. doi:10.1006/jmre.1998.1676
- Anderson, D. E., Williams, R. J., DeBerardino, T. M., Taylor, D. C., Ma, C. B., Kane, M. S., & Crawford, D. C. (2017). Magnetic Resonance Imaging characterization and clinical outcomes after NeoCart surgical therapy as a primary reparative treatment for knee cartilage injuries. *American Journal of Sports Medicine*, *45*(4), 875-883. doi:10.1177/0363546516677255
- Antons, J., Marascio, M. G. M., Nohava, J., Martin, R., Applegate, L. A., Bourban, P. E., & Pioletti, D. P. (2018). Zone-dependent mechanical properties of human articular cartilage obtained by indentation measurements. *Journal of Materials Science: Materials in Medicine*, *29*(5), 57. doi:10.1007/s10856-018-6066-0
- Beck, E. C., Barragan, M., Tadros, M. H., Gehrke, S. H., & Detamore, M. S. (2016). Approaching the compressive modulus of articular cartilage with a decellularized cartilage-based hydrogel. *Acta Biomaterialia*, *38*, 94-105. doi:10.1016/j.actbio.2016.04.019
- Bracaglia, L. G., Smith, B. T., Watson, E., Arumugasaamy, N., Mikos, A. G., & Fisher, J. P. (2017). 3D printing for the design and fabrication of polymer-based gradient scaffolds. *Acta Biomaterialia*, *56*, 3-13. doi:10.1016/j.actbio.2017.03.030
- Brown, C. P., Houle, M. A., Chen, M., Price, A. J., Légaré, F., & Gill, H. S. (2012). Damage initiation and progression in the cartilage surface probed by nonlinear optical microscopy. *Journal of the Mechanical Behavior of Biomedical Materials*, *5*(1), 62-70. doi:doi.org/10.1016/j.jmbbm.2011.08.004
- Buckwalter, J. A., Mow, V. C., & Ratcliffe, A. (1994). Restoration of injured or degenerated articular cartilage. *Journal of the American Academy of Orthopaedic Surgeons*, *2*(4), 192-201. doi:10.5435/00124635-199407000-00002
- Butz, K. D., Chan, D. D., Nauman, E. A., & Neu, C. P. Stress distributions and material properties determined in articular cartilage from MRI-based finite strains. *Journal of Biomechanics*, *44*(15), 2667-2672. doi:10.1016/j.jbiomech.2011.08.005
- Carter, T. E., Taylor, K. A., Spritzer, C. E., Utturkar, G. M., Taylor, D. C., Moorman, C. T., . . . DeFrate, L. E. (2015). In vivo cartilage strain increases following medial meniscal tear

- and correlates with synovial fluid matrix metalloproteinase activity. *Journal of Biomechanics*, 48(8), 1461-1468. doi:10.1016/j.jbiomech.2015.02.030
- Chan, D. D., Cai, L., Butz, K. D., Trippel, S. B., Nauman, E. A., & Neu, C. P. (2016). In vivo articular cartilage deformation: noninvasive quantification of intratissue strain during joint contact in the human knee. *Scientific Reports*, 6, Article 19220. doi:10.1038/srep19220
- Chan, D. D., & Neu, C. P. (2012). Transient and microscale deformations and strains measured under exogenous loading by noninvasive magnetic resonance. *PLoS One*, 7(3), e33463. doi:10.1371/journal.pone.0033463
- Chan, D. D., Neu, C. P., & Hull, M. L. (2009a). Articular cartilage deformation determined in an intact tibiofemoral joint by displacement-encoded imaging. *Magnetic Resonance in Medicine*, 61(4), 989-993. doi:10.1002/mrm.21927
- Chan, D. D., Neu, C. P., & Hull, M. L. (2009b). In situ deformation of cartilage in cyclically loaded tibiofemoral joints by displacement-encoded MRI. *Osteoarthritis Cartilage*, 17(11), 1461-1468. doi:10.1016/j.joca.2009.04.021
- Chen, A. C., Bae, W. C., Schinagl, R. M., & Sah, R. L. (2001). Depth- and strain-dependent mechanical and electromechanical properties of full-thickness bovine articular cartilage in confined compression. *Journal of Biomechanics*, 34(1), 1-12.
- Chung, C. Y., Heebner, J., Baskaran, H., Welter, J. F., & Mansour, J. M. (2015). Ultrasound elastography for estimation of regional strain of multilayered hydrogels and tissue-engineered cartilage. *Annual Review of Biomedical Engineering*, 43(12), 2991-3003. doi:10.1007/s10439-015-1356-x
- Crawford, D. C., DeBerardino, T. M., & Williams, R. J. (2012). NeoCart, an autologous cartilage tissue implant, compared with microfracture for treatment of distal femoral cartilage lesions: an FDA phase-II prospective, randomized clinical trial after two years. *Journal of Bone and Joint Surgery*, 94(11), 979-989. doi:10.2106/JBJS.K.00533
- Dale, M. R. T. (1999). *Spatial pattern analysis in plant ecology*. Cambridge: Cambridge University Press.
- Dale, M. R. T., Dixon, P., Fortin, M.-J., Legendre, P., Myers, D. E., & Rosenberg, M. S. (2002). Conceptual and mathematical relationships among methods for spatial analysis. *Ecography*, 25(5), 558-577. doi:10.1034/j.1600-0587.2002.250506.x
- Delaunay, B. (1934). Sur la sphère vide. *Bulletin de l'Académie des Sciences de l'URSS, Classe des Sciences Mathématiques et Na*(6), 793-800.
- Desrochers, J., Amrein, M. W., & Matyas, J. R. (2012). Viscoelasticity of the articular cartilage surface in early osteoarthritis. *Osteoarthritis and Cartilage*, 20(5), 413-421. doi:10.1016/j.joca.2012.01.011
- DiDomenico, C. D., & Bonassar, L. J. (2018). The effect of charge and mechanical loading on antibody diffusion through the articular surface of cartilage. *Journal of Biomechanical Engineering*, 141(1), 5. doi:10.1115/1.4041768
- Dimicco, M. A., & Sah, R. L. (2001). Integrative cartilage repair: adhesive strength is correlated with collagen deposition. *Journal of Orthopaedic Research*, 19(6), 1105-1112. doi:doi.org/10.1016/S0736-0266(01)00037-7
- Dong, Y.-f., Hu, G.-h., Zhang, L.-l., Hu, Y., Dong, Y.-h., & Xu, Q.-r. (2011). Accurate 3D reconstruction of subject-specific knee finite element model to simulate the articular cartilage defects. *Journal of Shanghai Jiaotong University (Science)*, 16(5), 620. doi:10.1007/s12204-011-1199-z

- Eckstein, F., Tieschky, M., Faber, S., Englmeier, K. H., & Reiser, M. (1999). Functional analysis of articular cartilage deformation, recovery, and fluid flow following dynamic exercise in vivo. *Anatomy and Embryology (Berl)*, 200(4), 419-424. doi:10.1007/s004290050291
- Erne, O. K., Reid, J. B., Ehmke, L. W., Sommers, M. B., Madey, S. M., & Bottlang, M. (2005). Depth-dependent strain of patellofemoral articular cartilage in unconfined compression. *Journal of Biomechanics*, 38(4), 667-672. doi:doi.org/10.1016/j.jbiomech.2004.04.005
- Eskelinen, A. S. A., Mononen, M. E., Venäläinen, M. S., Korhonen, R. K., & Tanska, P. (2019). Maximum shear strain-based algorithm can predict proteoglycan loss in damaged articular cartilage. *Biomechanics and Modeling in Mechanobiology*, 18(3), 753-778. doi:10.1007/s10237-018-01113-1
- Ferizi, U., Rossi, I., Lee, Y., Lendhey, M., Teplensky, J., Kennedy, O. D., . . . Raya, J. G. (2017). Diffusion tensor imaging of articular cartilage at 3T correlates with histology and biomechanics in a mechanical injury model. *Magnetic Resonance in Medicine*, 78(1), 69-78. doi:10.1002/mrm.26336
- Fisher, M. B., Henning, E. A., Söegaard, N. B., Dodge, G. R., Steinberg, D. R., & Mauck, R. L. (2014). Maximizing cartilage formation and integration via a trajectory-based tissue engineering approach. *Biomaterials*, 35(7), 2140-2148. doi:10.1016/j.biomaterials.2013.11.031
- Fox, S. A. J., Bedi, A., & Rodeo, S. A. (2009). The basic science of articular cartilage: structure, composition, and function. *Sports Health*, 1(6), 461-468. doi:10.1177/1941738109350438
- Fung, Y. C. (1993). *Biomechanics: mechanical properties of living tissues*. New York: Springer.
- Geers, M. G. D., De Borst, R., & Brekelmans, W. A. M. (1996). Computing strain fields from discrete displacement fields in 2D-solids. *International Journal of Solids and Structures*, 33(29), 4293-4307. doi:10.1016/0020-7683(95)00240-5
- Gilchrist, C. L., Witvoet-Braam, S. W., Guilak, F., & Setton, L. A. (2007). Measurement of intracellular strain on deformable substrates with texture correlation. *Journal of Biomechanics*, 40(4), 786-794. doi:10.1016/j.jbiomech.2006.03.013
- Gobbi, A., Karnatzikos, G., & Kumar, A. (2014). Long-term results after microfracture treatment for full-thickness knee chondral lesions in athletes. *Knee Surg Sports Traumatol Arthrosc*, 22(9), 1986-1996. doi:10.1007/s00167-013-2676-8
- Griebel, A. J., Khoshgoftar, M., Novak, T., van Donkelaar, C. C., & Neu, C. P. (2014). Direct noninvasive measurement and numerical modeling of depth-dependent strains in layered agarose constructs. *Journal of Biomechanics*, 47(9), 2149-2156. doi:10.1016/j.jbiomech.2013.09.025
- Griffin, D. J., Vicari, J., Buckley, M. R., Silverberg, J. L., Cohen, I., & Bonassar, L. J. (2014). Effects of enzymatic treatments on the depth-dependent viscoelastic shear properties of articular cartilage. *Journal of Orthopaedic Research*, 32(12), 1652-1657. doi:doi.org/10.1002/jor.22713
- Guan, P.-P., Guo, J.-W., Yu, X., Wang, Y., Wang, T., Konstantopoulos, K., . . . Wang, P. (2015). The role of cyclooxygenase-2, interleukin-1 $\beta$  and fibroblast growth factor-2 in the activation of matrix metalloproteinase-1 in sheared-chondrocytes and articular cartilage. *Scientific Reports*, 5(2015), 10412-10412. doi:10.1038/srep10412
- Guermazi, A., Niu, J., Hayashi, D., Roemer, F. W., Englund, M., Neogi, T., . . . Felson, D. T. (2012). Prevalence of abnormalities in knees detected by MRI in adults without knee

- osteoarthritis: population based observational study (Framingham Osteoarthritis Study). *BMJ : British Medical Journal*, 345, e5339. doi:10.1136/bmj.e5339
- Halonen, K. S., Mononen, M. E., Jurvelin, J. S., Töyräs, J., & Korhonen, R. K. (2013). Importance of depth-wise distribution of collagen and proteoglycans in articular cartilage—A 3D finite element study of stresses and strains in human knee joint. *Journal of Biomechanics*, 46(6), 1184-1192. doi:10.1016/j.jbiomech.2012.12.025
- Halonen, K. S., Mononen, M. E., Jurvelin, J. S., Töyräs, J., Salo, J., & Korhonen, R. K. (2014). Deformation of articular cartilage during static loading of a knee joint – Experimental and finite element analysis. *Journal of Biomechanics*, 47(10), 2467-2474. doi:10.1016/j.jbiomech.2014.04.013
- Hayashi, D., Li, X., Murakami, A. M., Roemer, F. W., Trattng, S., & Guermazi, A. (2018). Understanding magnetic resonance imaging of knee cartilage repair: a focus on clinical relevance. *Cartilage*, 9(3), 223-236. doi:10.1177/1947603517710309
- Hayes, W. C., & Bodine, A. J. (1978). Flow-independent viscoelastic properties of articular cartilage matrix. *Journal of Biomechanics*, 11(8), 407-419. doi:doi.org/10.1016/0021-9290(78)90075-1
- Houck, D. A., Kraeutler, M. J., Belk, J. W., Frank, R. M., McCarty, E. C., & Bravman, J. T. (2018). Do focal chondral defects of the knee increase the risk for progression to Osteoarthritis? A review of the literature. *Orthopaedic Journal of Sports Medicine*, 6(10). doi:10.1177/2325967118801931
- Howard, D., Buttery, L. D., Shakesheff, K. M., & Roberts, S. J. (2008). Tissue engineering: strategies, stem cells and scaffolds. *Journal of Anatomy*, 213(1), 66-72. doi:10.1111/j.1469-7580.2008.00878.x
- Huang, C.-Y., Mow, V. C., & Ateshian, G. A. (2001). The role of flow-independent viscoelasticity in the biphasic tensile and compressive responses of articular cartilage. *Journal of Biomechanical Engineering*, 123(5), 410-417. doi:10.1115/1.1392316
- Huang, C. Y., Soltz, M. A., Kopacz, M., Mow, V. C., & Ateshian, G. A. (2003). Experimental verification of the roles of intrinsic matrix viscoelasticity and tension-compression nonlinearity in the biphasic response of cartilage. *Journal of Biomechanical Engineering*, 125(1), 84-93. doi:10.1115/1.1531656
- Hunold, P., Maderwald, S., Ladd, M. E., Jellus, V., & Barkhausen, J. (2004). Parallel acquisition techniques in cardiac cine magnetic resonance imaging using TrueFISP sequences: Comparison of image quality and artifacts. *Journal of Magnetic Resonance Imaging*, 20(3), 506-511. doi:10.1002/jmri.20125
- Hunter, D. J., Guermazi, A., Lo, G. H., Grainger, A. J., Conaghan, P. G., Boudreau, R. M., & Roemer, F. W. (2011). Evolution of semi-quantitative whole joint assessment of knee OA: MOAKS (MRI Osteoarthritis Knee Score). *Osteoarthritis Cartilage*, 19(8), 990-1002. doi:10.1016/j.joca.2011.05.004
- Im, H.-J., Muddasani, P., Natarajan, V., Schmid, T. M., Block, J. A., Davis, F., . . . Loeser, R. F. (2007). Basic fibroblast growth factor stimulates matrix metalloproteinase-13 via the molecular cross-talk between the mitogen-activated protein kinases and protein kinase Cdelta pathways in human adult articular chondrocytes. *The Journal of Biological Chemistry*, 282(15), 11110-11121. doi:10.1074/jbc.M609040200
- Irwin, R. M., Gao, T., Boys, A. J., Ortved, K., Cohen, I., & Bonassar, L. J. (2021). Microscale strain mapping demonstrates the importance of interface slope in the mechanics of

- cartilage repair. *Journal of Biomechanics*, 114, Article 110159. doi:10.1016/j.jbiomech.2020.110159
- Jeffrey, J. E., Gregory, D. W., & Aspden, R. M. (1995). Matrix damage and chondrocyte viability following a single impact load on articular-cartilage. *Archives of Biochemistry and Biophysics*, 322(1), 87-96. doi:doi.org/10.1006/abbi.1995.1439
- June, R. K., & Fyhrie, D. P. (2013). A comparison of cartilage stress-relaxation models in unconfined compression: QLV and stretched exponential in combination with fluid flow. *Computer Methods in Biomechanics and Biomedical Engineering*, 16(5), 565-576. doi:10.1080/10255842.2011.629612
- Karataglis, D., Green, M. A., & Learmonth, D. J. (2006). Autologous osteochondral transplantation for the treatment of chondral defects of the knee. *Knee*, 13(1), 32-35. doi:10.1016/j.knee.2005.05.006
- Kellgren, J. H., & Lawrence, J. S. (1957). Radiological assessment of osteo-arthritis. *Annals of the Rheumatic Diseases*, 16(4), 494-502.
- Khan, I. M., Gilbert, S. J., Singhrao, S. K., Duance, V. C., & Archer, C. W. (2008). Cartilage integration: evaluation of the reasons for failure of integration during cartilage repair. A review. *European Cells and Materials*, 16, 26-39. doi:10.22203/ecm.v016a04
- Kim, H. J., Lee, Y. H., & Kim, C. K. (2007). Biomarkers of muscle and cartilage damage and inflammation during a 200 km run. *European Journal of Applied Physiology*, 99(4), 443-447. doi:10.1007/s00421-006-0362-y
- Kiviranta, P., Rieppo, J., Korhonen, R. K., Julkunen, P., Töyräs, J., & Jurvelin, J. S. (2006). Collagen network primarily controls Poisson's ratio of bovine articular cartilage in compression. *Journal of Orthopaedic Research*, 24(4), 690-699. doi:10.1002/jor.20107
- Kleemann, R. U., Krocker, D., Cedraro, A., Tuischer, J., & Duda, G. N. (2005). Altered cartilage mechanics and histology in knee osteoarthritis: relation to clinical assessment (ICRS Grade). *Osteoarthritis Cartilage*, 13(11), 958-963. doi:10.1016/j.joca.2005.06.008
- Klein, T. J., Chaudhry, M., Bae, W. C., & Sah, R. L. (2007). Depth-dependent biomechanical and biochemical properties of fetal, newborn, and tissue-engineered articular cartilage. *Journal of Biomechanics*, 40(1), 182-190. doi:10.1016/j.jbiomech.2005.11.002
- Komeili, A., Abusara, Z., Federico, S., & Herzog, W. (2018). A compression system for studying depth-dependent mechanical properties of articular cartilage under dynamic loading conditions. *Medical Engineering & Physics*, 60, 103-108. doi:10.1016/j.medengphy.2018.07.004
- Kumar, R., Grønhaug, K. M., Afseth, N. K., Isaksen, V., de Lange Davies, C., Drogset, J. O., & Lilledahl, M. B. (2015). Optical investigation of osteoarthritic human cartilage (ICRS grade) by confocal Raman spectroscopy: a pilot study. *Analytical and Bioanalytical Chemistry*, 407(26), 8067-8077. doi:10.1007/s00216-015-8979-5
- Lad, N. K., Liu, B., Ganapathy, P. K., Utturkar, G. M., Sutter, E. G., Moorman, C. T., . . . DeFrate, L. E. (2016). Effect of normal gait on in vivo tibiofemoral cartilage strains. *Journal of Biomechanics*, 49(13), 2870-2876. doi:10.1016/j.jbiomech.2016.06.025
- Li, X., Martin, S., Pitris, C., Ghanta, R., Stamper, D. L., Harman, M., . . . Brezinski, M. E. (2005). High-resolution optical coherence tomographic imaging of osteoarthritic cartilage during open knee surgery. *Arthritis Research & Therapy*, 7(2), R318-R323. doi:10.1186/ar1491

- Little, C. J., Bawolin, N. K., & Chen, X. (2011). Mechanical properties of natural cartilage and tissue-engineered constructs. *Tissue Engineering Part B: Reviews*, 17(4), 213-227. doi:10.1089/ten.teb.2010.0572
- Mak, A. F. (1986). The apparent viscoelastic behavior of articular cartilage—the contributions from the intrinsic matrix viscoelasticity and interstitial fluid flows. *Journal of Biomechanical Engineering*, 108(2), 123-130. doi:10.1115/1.3138591
- Martin, K. J., Neu, C. P., & Hull, M. L. (2009). Quasi-steady-state displacement response of whole human cadaveric knees in a MRI scanner. *Journal of Biomechanical Engineering*, 131(8), 7. doi:10.1115/1.2978986
- McDermott, I. D., & Amis, A. A. (2006). The consequences of meniscectomy. *The Journal of Bone and Joint Surgery. British volume*, 88-B(12), 1549-1556. doi:10.1302/0301-620X.88B12.18140
- Milano, G., Sanna Passino, E., Deriu, L., Careddu, G., Manunta, L., Manunta, A., . . . Fabbriani, C. (2010). The effect of platelet rich plasma combined with microfractures on the treatment of chondral defects: an experimental study in a sheep model. *Osteoarthritis and Cartilage*, 18(7), 971-980. doi:doi.org/10.1016/j.joca.2010.03.013
- Mobasheri, A., & Batt, M. (2016). An update on the pathophysiology of osteoarthritis. *Annals of Physical and Rehabilitation Medicine*, 59(5), 333-339. doi:10.1016/j.rehab.2016.07.004
- Moger, C. J., Arkill, K. P., Barrett, R., Bleuet, P., Ellis, R. E., Green, E. M., & Winlove, C. P. (2009). Cartilage collagen matrix reorientation and displacement in response to surface loading. *Journal of Biomechanical Engineering*, 131(3). doi:10.1115/1.3049478
- Moretti, M., Wendt, D., Schaefer, D., Jakob, M., Hunziker, E. B., Heberer, M., & Martin, I. (2005). Structural characterization and reliable biomechanical assessment of integrative cartilage repair. *Journal of Biomechanics*, 38(9), 1846-1854. doi:10.1016/j.jbiomech.2004.08.021
- Mow, V. C., & Guo, X. E. (2002). Mechano-electrochemical properties of articular cartilage: their inhomogeneities and anisotropies. *Annual Review of Biomedical Engineering*, 4(1), 175-209. doi:10.1146/annurev.bioeng.4.110701.120309
- Nebelung, S., Brill, N., Marx, U., Quack, V., Tingart, M., Schmitt, R., . . . Jahr, H. (2015). Three-dimensional imaging and analysis of human cartilage degeneration using Optical Coherence Tomography. *Journal of Orthopaedic Research*, 33(5), 651-659. doi:10.1002/jor.22828
- Neu, C. P., & Hull, M. L. (2003). Toward an MRI-based method to measure non-uniform cartilage deformation: an MRI-cyclic loading apparatus system and steady-state cyclic displacement of articular cartilage under compressive loading. *Journal of Biomechanical Engineering*, 125(2), 180-188.
- Neu, C. P., Hull, M. L., Walton, J. H., & Buonocore, M. H. (2005). MRI-based technique for determining nonuniform deformations throughout the volume of articular cartilage explants. *Magnetic Resonance in Medicine*, 53(2), 321-328. doi:10.1002/mrm.20343
- Oloyede, A., Flachsmann, R., & Broom, N. D. (1992). The dramatic influence of loading velocity on the compressive response of articular cartilage. *Connective Tissue Research*, 27(4), 211-224. doi:10.3109/03008209209006997
- Olvera, D., Daly, A., & Kelly, D. J. (2015). Mechanical testing of cartilage constructs. In P. M. Doran (Ed.), *Cartilage tissue engineering: methods and protocols* (pp. 279-287). New York, NY: Springer New York.

- Ossendorff, R., Franke, K., Erdle, B., Uhl, M., Südkamp, N. P., & Salzmann, G. M. (2019). Clinical and radiographical ten years long-term outcome of microfracture vs. autologous chondrocyte implantation: a matched-pair analysis. *International Orthopaedics*, 43(3), 553-559. doi:10.1007/s00264-018-4025-5
- Palchesko, R. N., Zhang, L., Sun, Y., & Feinberg, A. W. (2012). Development of polydimethylsiloxane substrates with tunable elastic modulus to study cell mechanobiology in muscle and nerve. *PLoS One*, 7(12), e51499. doi:10.1371/journal.pone.0051499
- Plotnick, R. E., Gardner, R. H., Hargrove, W. W., Prestegard, K., & Perlmutter, M. (1996). Lacunarity analysis: A general technique for the analysis of spatial patterns. *Physical Review E*, 53(5), 5461-5468. doi:10.1103/PhysRevE.53.5461
- Plotnick, R. E., Gardner, R. H., & O'Neill, R. V. (1993). Lacunarity indices as measures of landscape texture. *Landscape Ecology*, 8(3), 201-211. doi:10.1007/BF00125351
- Pritchard, H. W. (2001). Spatial pattern analysis in plant ecology. *Annals of Botany*, 87(2), 283-284. doi:10.1006/anbo.2000.1304
- Pritzker, K. P., Gay, S., Jimenez, S. A., Ostergaard, K., Pelletier, J. P., Revell, P. A., . . . van den Berg, W. B. (2006). Osteoarthritis cartilage histopathology: grading and staging. *Osteoarthritis Cartilage*, 14(1), 13-29. doi:10.1016/j.joca.2005.07.014
- Puig-Junoy, J., & Ruiz Zamora, A. (2015). Socio-economic costs of osteoarthritis: a systematic review of cost-of-illness studies. *Seminars in Arthritis and Rheumatism*, 44(5), 531-541. doi:10.1016/j.semarthrit.2014.10.012
- Raghunath, J., Rollo, J., Sales, K. M., Butler, P. E., & Seifalian, A. M. (2007). Biomaterials and scaffold design: key to tissue-engineering cartilage. *Biotechnology and Applied Biochemistry*, 46(2), 73-84. doi:10.1042/BA20060134
- Redler, I., Mow, V. C., Zimny, M. L., & Mansell, J. (1975). The ultrastructure and biomechanical significance of the tidemark of articular cartilage. *Clinical Orthopaedics and Related Research*(112), 357-362.
- Reichenbach, S., Yang, M., Eckstein, F., Niu, J., Hunter, D. J., McLennan, C. E., . . . Felson, D. T. (2010). Does cartilage volume or thickness distinguish knees with and without mild radiographic osteoarthritis? The Framingham Study. *Annals of the Rheumatic Diseases*, 69(1), 143-149. doi:10.1136/ard.2008.099200
- Rodriguez-Vila, B., Sánchez-González, P., Oropesa, I., Gomez, E. J., & Pierce, D. M. (2017). Automated hexahedral meshing of knee cartilage structures – application to data from the osteoarthritis initiative. *Computer Methods in Biomechanics and Biomedical Engineering*, 20(14), 1543-1553. doi:10.1080/10255842.2017.1383984
- Roemer, F. W., Guermazi, A., Trattnig, S., Apprich, S., Marlovits, S., Niu, J., . . . Welsch, G. H. (2014). Whole joint MRI assessment of surgical cartilage repair of the knee: cartilage repair osteoarthritis knee score (CROAKS). *Osteoarthritis Cartilage*, 22(6), 779-799. doi:10.1016/j.joca.2014.03.014
- Rolauffs, B., Muehleman, C., Li, J., Kurz, B., Kuettner, K. E., Frank, E., & Grodzinsky, A. J. (2010). Vulnerability of the superficial zone of immature articular cartilage to compressive injury. *Arthritis & Rheumatism*, 62(10), 3016-3027. doi:10.1002/art.27610
- Roughley, P. J., & Mort, J. S. (2014). The role of aggrecan in normal and osteoarthritic cartilage. *Journal of Experimental Orthopaedics*, 1(1), 8. doi:10.1186/s40634-014-0008-7

- Sajid, S., & Chan, D. D. (2019). *Differentiation of cartilage culture conditions by depth-wise statistical analysis of MRI-based strain fields*. Paper presented at the Computer Methods in Biomechanics and Biomedical Engineering, New York, NY.
- Schinagl Robert, M., Gurskis, D., Chen Albert, C., & Sah Robert, L. (2005). Depth-dependent confined compression modulus of full-thickness bovine articular cartilage. *Journal of Orthopaedic Research*, *15*(4), 499-506. doi:10.1002/jor.1100150404
- Schumacher, B. L., Block, J. A., Schmid, T. M., Aydelotte, M. B., & Kuettner, K. E. (1994). A novel proteoglycan synthesized and secreted by chondrocytes of the superficial zone of articular cartilage. *Archives of Biochemistry and Biophysics*, *311*(1), 144-152. doi:doi.org/10.1006/abbi.1994.1219
- Selyutina, N. S., Argatov, I. I., & Mishuris, G. S. (2015). On application of Fung's quasi-linear viscoelastic model to modeling of impact experiment for articular cartilage. *Mechanics Research Communications*, *67*, 24-30. doi:10.1016/j.mechrescom.2015.04.003
- Sennett, M. L., Meloni, G. R., Farran, A. J. E., Guehring, H., Mauck, R. L., & Dodge, G. R. (2018). Sprifermin treatment enhances cartilage integration in an in vitro repair model. *Journal of Orthopaedic Research*, *36*(10), 2648-2656. doi:10.1002/jor.24048
- Shapiro, F., Koide, S., & Glimcher, M. (1993). Cell origin and differentiation in the repair of full-thickness defects of articular cartilage. *Journal of Bone and Joint Surgery*, *75*(4), 532-553.
- Simo, S., Shu-Zhe, W., Yan-Ping, H., & Yong-Ping, Z. (2009). Quantification of the optical surface reflection and surface roughness of articular cartilage using optical coherence tomography. *Physics in Medicine & Biology*, *54*(22), 6837.
- Spahn, G., & Hofmann, G. O. (2014). [Focal cartilage defects within the medial knee compartment. predictors for osteoarthritis progression]. *Zeitschrift fur Orthopadie und Unfallchirurgie*, *152*(5), 480-488. doi:10.1055/s-0034-1383081
- Szarko, M., Muldrew, K., & Bertram, J. E. A. (2010). Freeze-thaw treatment effects on the dynamic mechanical properties of articular cartilage. *BMC Musculoskeletal Disorders*, *11*(1), 231. doi:10.1186/1471-2474-11-231
- Taylor, D. W., C Bohm, K., Taylor, J. E., & Gross, A. E. (2011). Use of fresh osteochondral allograft in repair of distal femur after trauma. *McGill Journal of Medicine*, *13*(1), 22.
- Tew, S., Redman, S., Kwan, A., Walker, E., Khan, I., Dowthwaite, G., . . . Archer, C. W. (2001). Differences in repair responses between immature and mature cartilage. *Clinical Orthopaedics and Related Research*, *391*(Supplement), S142-152.
- Theodoropoulos, J. S., DeCroos, A. J. N., Petrera, M., Park, S., & Kandel, R. A. (2016). Mechanical stimulation enhances integration in an in vitro model of cartilage repair. *Knee Surgery, Sports Traumatology, Arthroscopy*, *24*(6), 2055-2064. doi:10.1007/s00167-014-3250-8
- Tripathy, S., & Berger, E. J. (2012). Quasi-linear viscoelastic properties of costal cartilage using atomic force microscopy. *Computer Methods in Biomechanics and Biomedical Engineering*, *15*(5), 475-486. doi:10.1080/10255842.2010.545820
- Ulrich-Vinther, M., Maloney, M. D., Schwarz, E. M., Rosier, R., & O'Keefe, R. J. (2003). Articular Cartilage Biology. *JAAOS - Journal of the American Academy of Orthopaedic Surgeons*, *11*(6), 421-430.
- van Haften, E. E., Ito, K., & van Donkelaar, C. C. (2017). The initial repair response of articular cartilage after mechanically induced damage. *Journal of Orthopaedic Research*, *35*(6), 1265-1273. doi:10.1002/jor.23382

- Vasara, A. I., Nieminen, M. T., Jurvelin, J. S., Peterson, L., Lindahl, A., & Kiviranta, I. (2005). Indentation stiffness of repair tissue after autologous chondrocyte transplantation. *Clinical Orthopaedics and Related Research*<sup>®</sup>, 433.
- Vaziri, A., Nayeb-Hashemi, H., Singh, A., & Tafti, B. A. (2008). Influence of meniscectomy and meniscus replacement on the stress distribution in human knee joint. *Annals of Biomedical Engineering*, 36(8), 1335-1344. doi:10.1007/s10439-008-9515-y
- Vinardell, T., Thorpe, S. D., Buckley, C. T., & Kelly, D. J. (2009). Chondrogenesis and integration of mesenchymal stem cells within an in vitro cartilage defect repair model. *Annals of Biomedical Engineering*, 37(12), 2556-2565. doi:10.1007/s10439-009-9791-1
- Wang, S., Bao, Y., Guan, Y., Zhang, C., Liu, H., Yang, X., . . . Chen, Q. (2018). Strain distribution of repaired articular cartilage defects by tissue engineering under compression loading. *Journal of Orthopaedic Surgery and Research*, 13(1), 19-26. doi:10.1186/s13018-018-0726-0
- Welsch, G. H., Zak, L., Mamisch, T. C., Paul, D., Lauer, L., Mauerer, A., . . . Trattnig, S. (2011). Advanced morphological 3D magnetic resonance observation of cartilage repair tissue (MOCART) scoring using a new isotropic 3D proton-density, turbo spin echo sequence with variable flip angle distribution (PD-SPACE) compared to an isotropic 3D steady-state free precession sequence (True-FISP) and standard 2D sequences. *Journal of Magnetic Resonance Imaging*, 33(1), 180-188. doi:10.1002/jmri.22399
- Willett, M., Duda, J., Fenton, S., Gautrey, C., Greig, C., & Rushton, A. (2019). Effectiveness of behaviour change techniques in physiotherapy interventions to promote physical activity adherence in lower limb osteoarthritis patients: A systematic review. *PLoS One*, 14(7), e0219482. doi:10.1371/journal.pone.0219482
- Woodfield, T. B., Malda, J., de Wijn, J., Péters, F., Riesle, J., & van Blitterswijk, C. A. (2004). Design of porous scaffolds for cartilage tissue engineering using a three-dimensional fiber-deposition technique. *Biomaterials*, 25(18), 4149-4161. doi:10.1016/j.biomaterials.2003.10.056
- Xu, Y., Guo, X., Yang, S., Li, L., Zhang, P., Sun, W., . . . Mi, S. (2018). Construction of bionic tissue engineering cartilage scaffold based on three-dimensional printing and oriented frozen technology. *Journal of Biomedical Materials Research Part A*, 106(6), 1664-1676. doi:10.1002/jbm.a.36368
- Yin, Z. (2014). Magnetic resonance characterization of tissue engineered cartilage via changes in relaxation times, diffusion coefficient, and shear modulus. *Critical Reviews in Biomedical Engineering*, 42(2), 137-191.
- Zevenbergen, L., Gsell, W., Cai, L., Chan, D. D., Famaey, N., Vander Sloten, J., . . . Jonkers, I. (2018). Cartilage-on-cartilage contact: effect of compressive loading on tissue deformations and structural integrity of bovine articular cartilage. *Osteoarthritis and Cartilage*, 26(12), 1710-1721. doi:10.1016/j.joca.2018.08.009

## APPENDICES

### Appendix A Process Verification

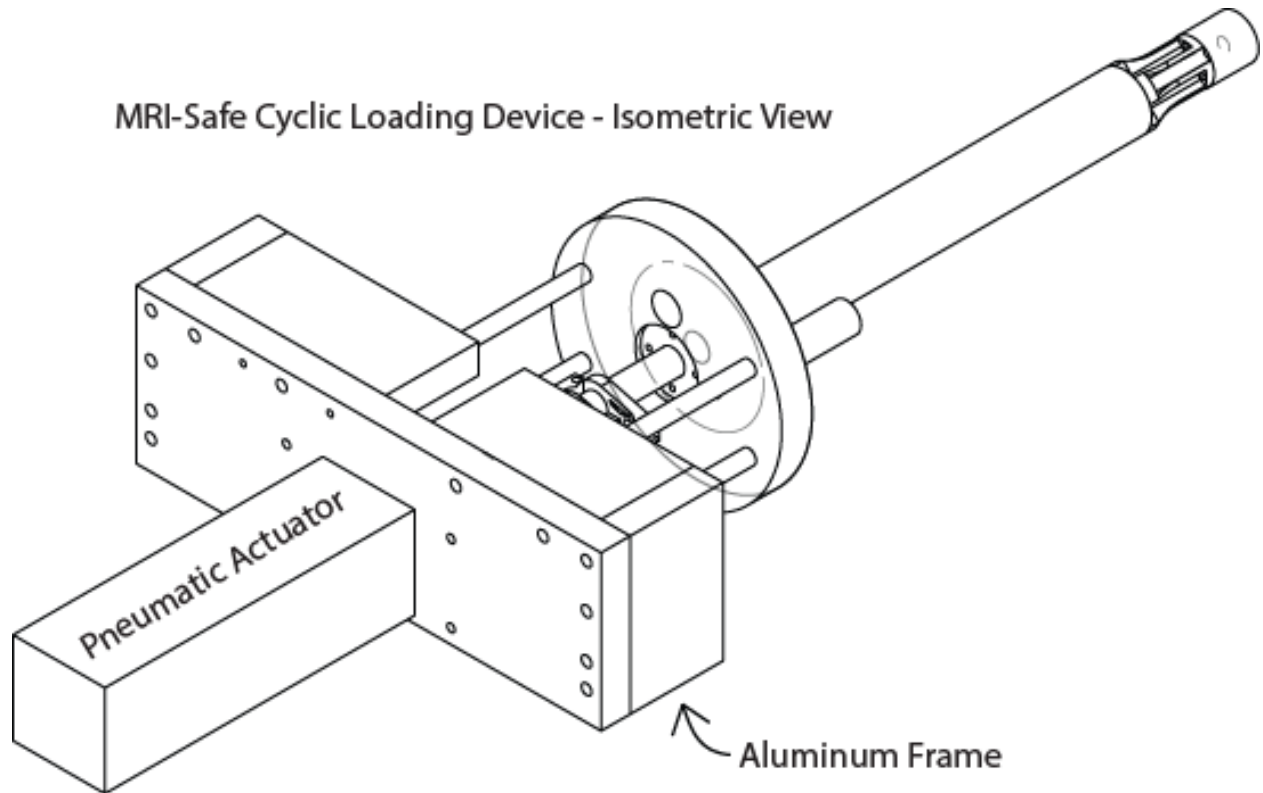


Figure A.1: Isometric view of the MRI-safe cyclic loading device. The entire device bolts to the front of an MRI scanner through the aluminum frame. The plastic components extend into the magnet where a sample holder lies at isocenter.

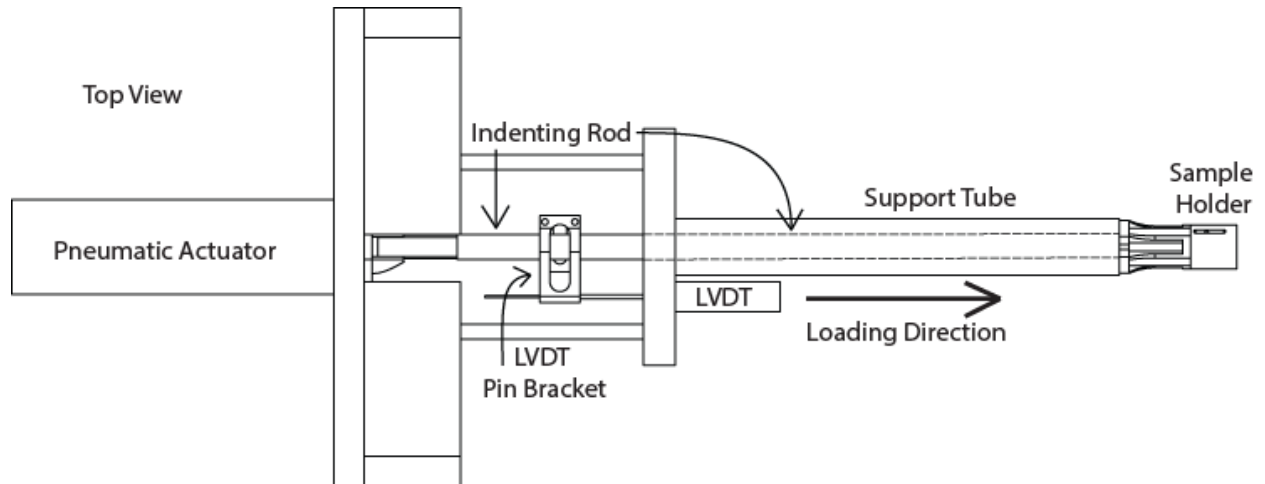


Figure A.2: Top view of the cyclic loading device. The location of the LVDT and accessories is shown, and were used during system validation. The load from the device is applied from an indenting rod, which extends through the hollow support tube, and applies a compressive load to a sample inside the sample holder.

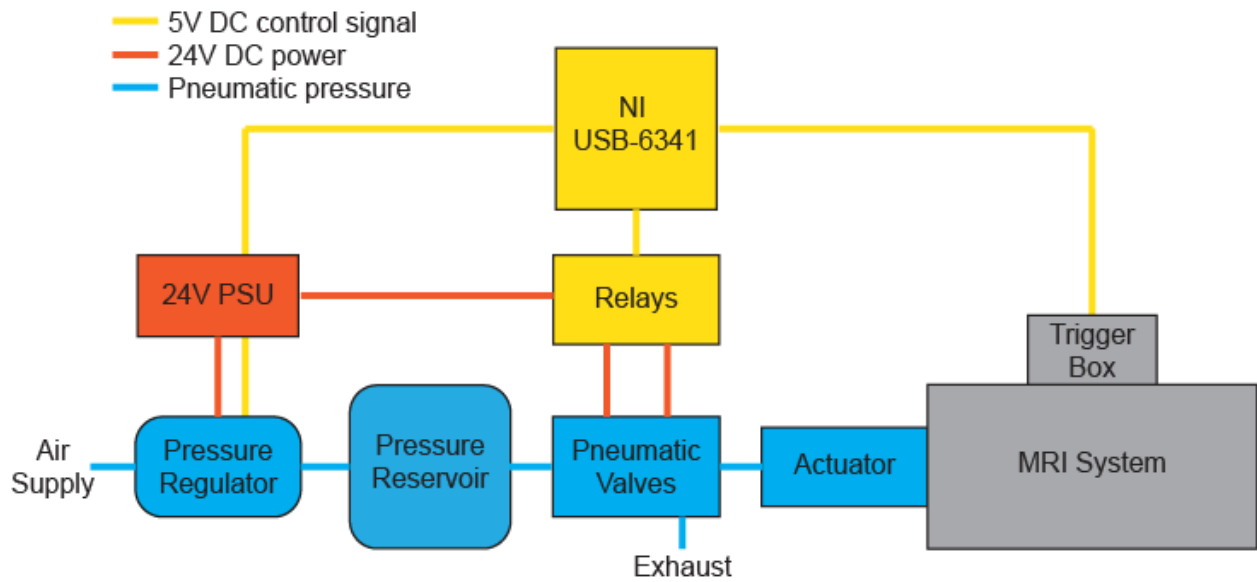
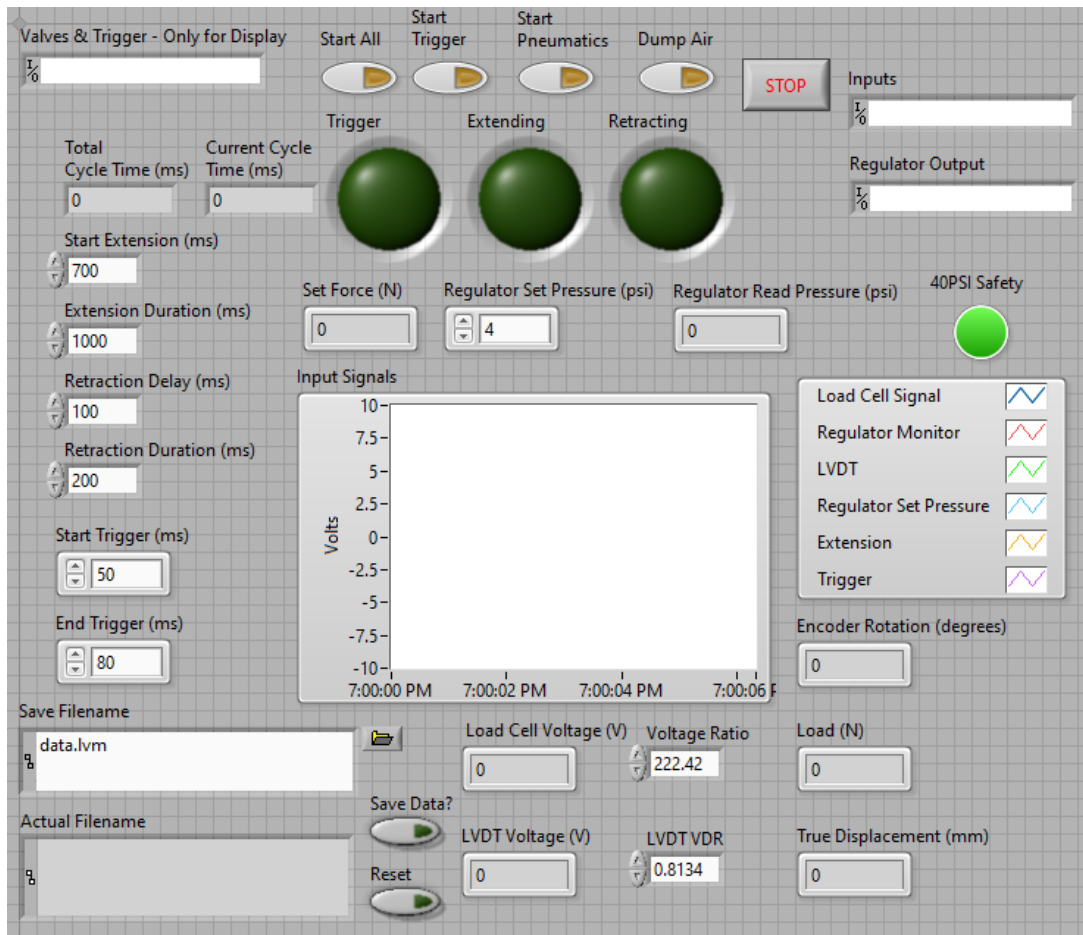
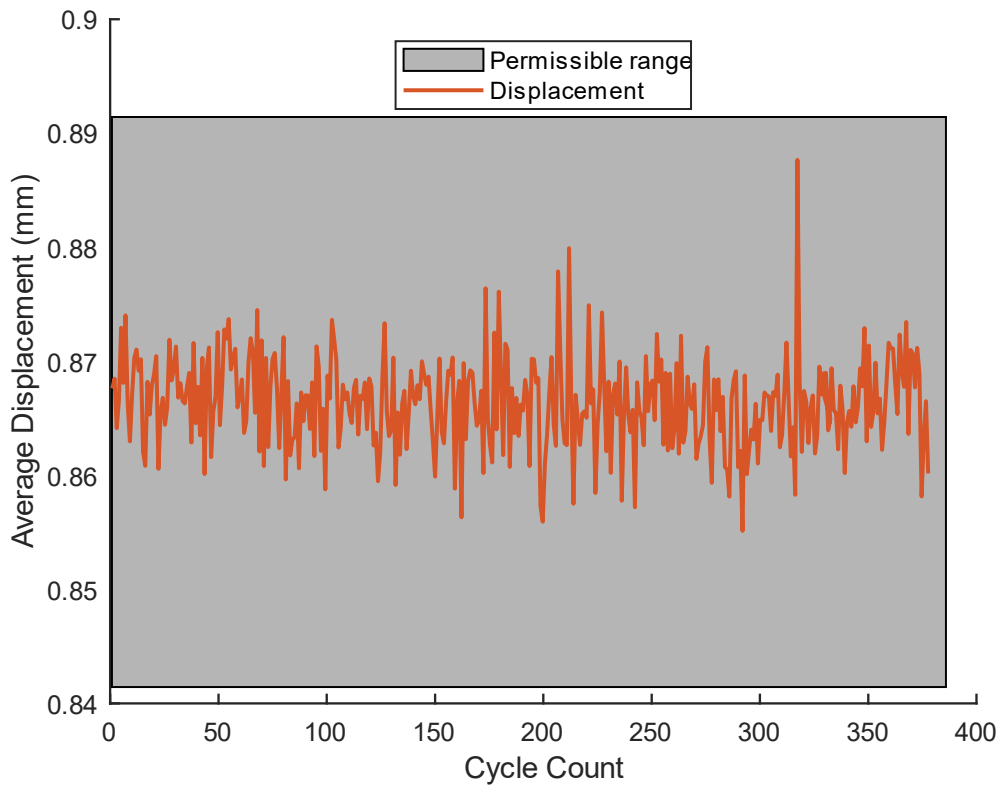


Figure A.3: System controls. The NI DAQ and VI control the entire system through the pressure regulator, relays for the pneumatic valves, and the trigger box for the MRI system.



**Figure A.4: Virtual instrument (VI) used to operate the system. The VI controls the loading cycles through the four parameters on the left side- "Start Extension", "Extension Duration", "Retraction Delay", "Retraction Duration". The applied load is controlled through the "Regulator Set Pressure" parameter. The remaining controls and readouts are used for data logging and ensuring the system is working correctly.**



**Figure A.5: Loading plateau average movement, cycle-to-cycle variation over 384 loading cycles. System movement was within one-half pixel width (50 $\mu$ m), the acceptable limit of movement.**

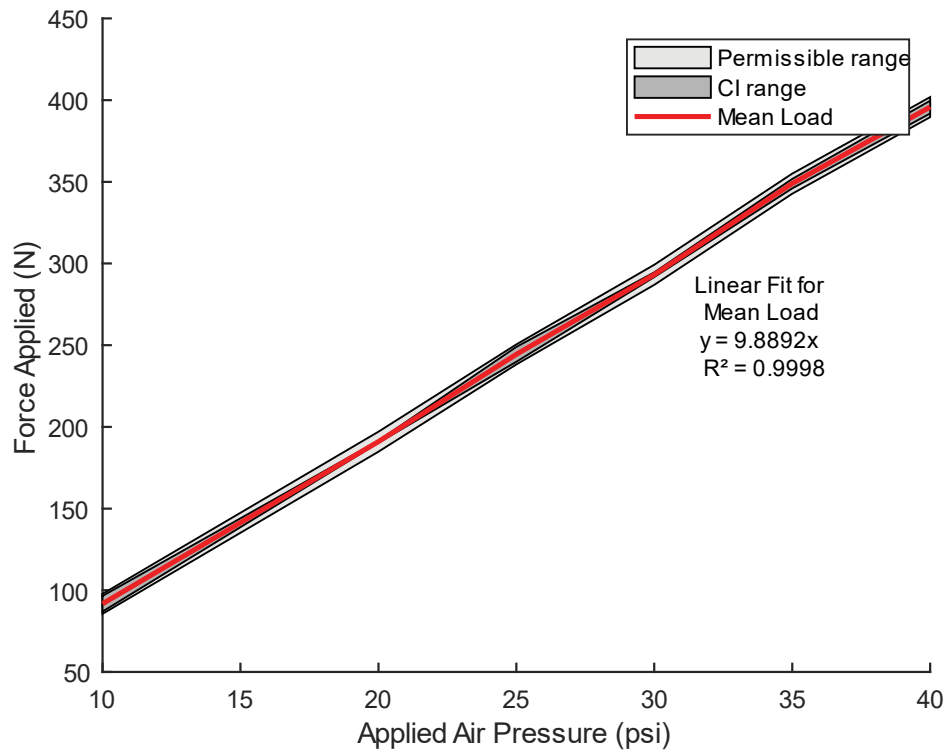


**Figure A.6: Pressure-load linearity diagram for the cyclic loading device. Confidence intervals of the applied force during the load plateaus were computed, and shown to be within the permissible range with an excellent fit for linearity.**

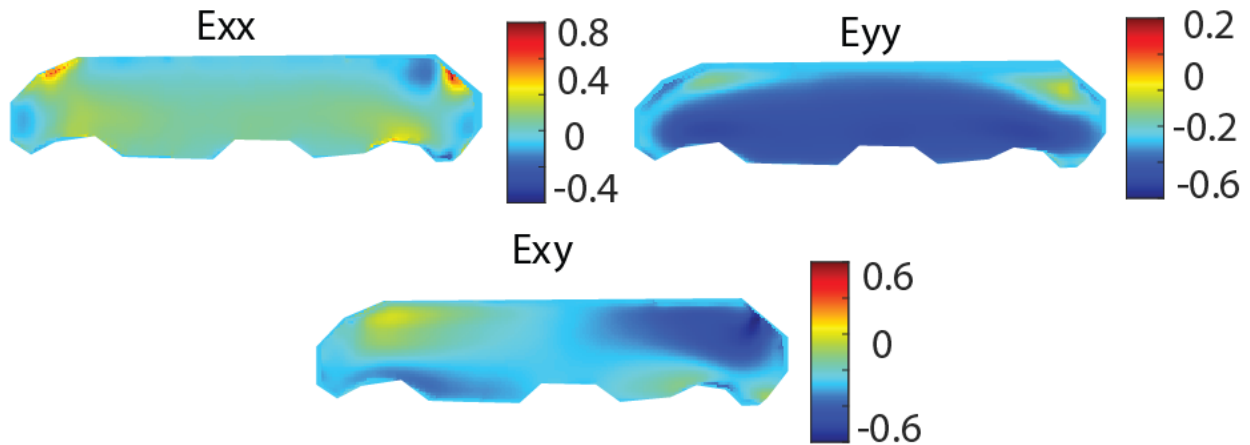


**Figure A.7: Principal strains computed for the Sylgard 527 phantom using 50 cycles of a 5x5 Gaussian filter. Parts of the phantom surface were not analyzed due to pockets of air creating signal voids, hence the irregular shape. Phantom scans were repeated 9 times. Unsmoothed displacement data was used to analyze scanner noise. Pooled standard deviation of the noise equaled 0.0061mm, and was used to inject noise into simulated displacement maps.**

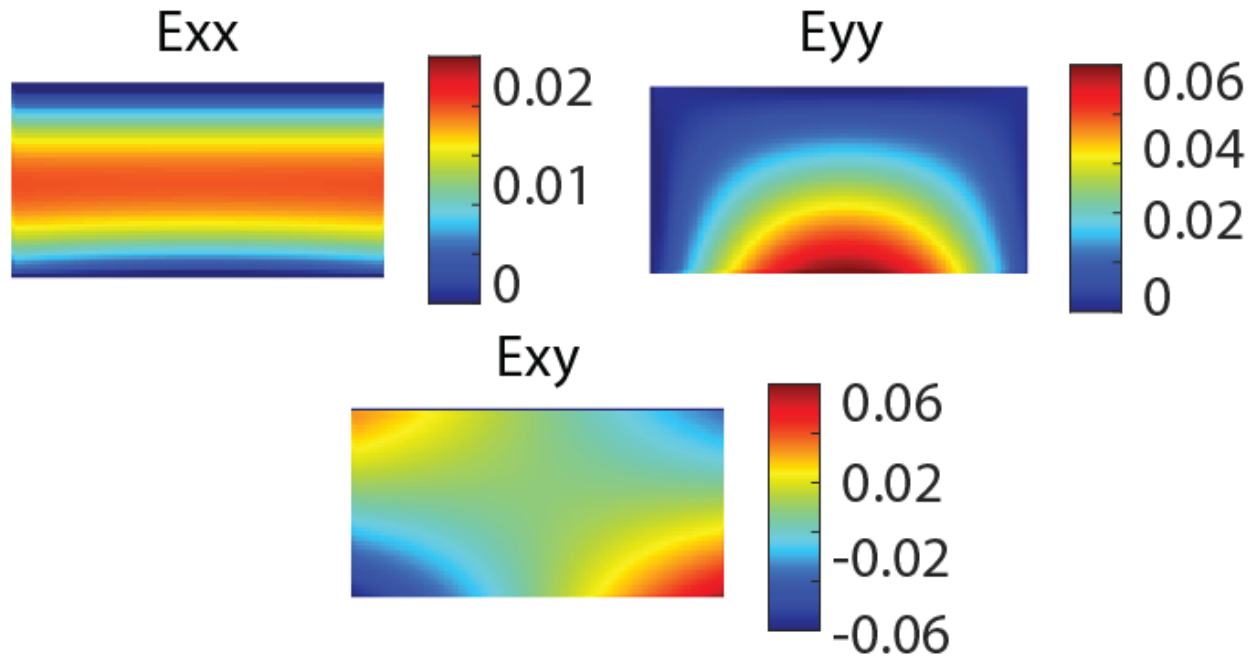
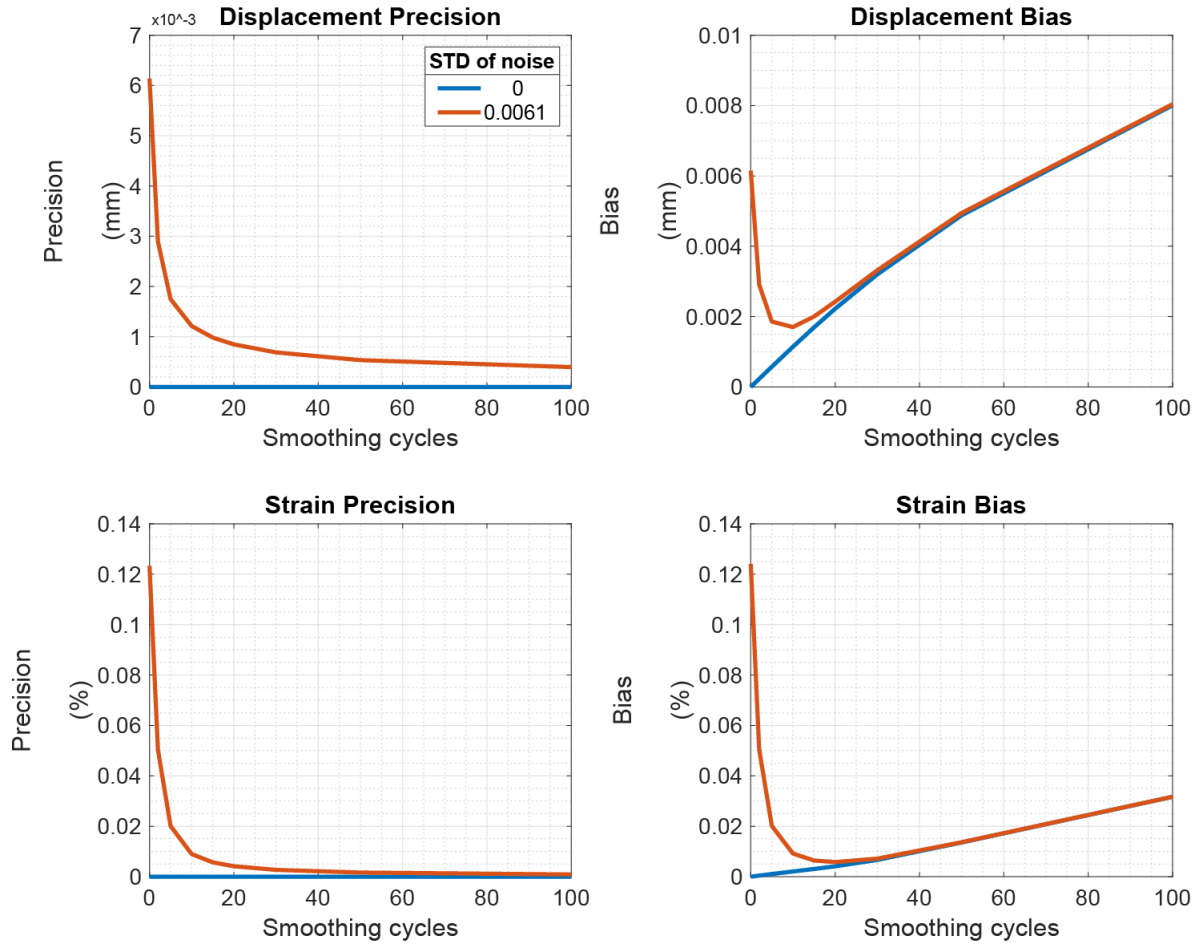
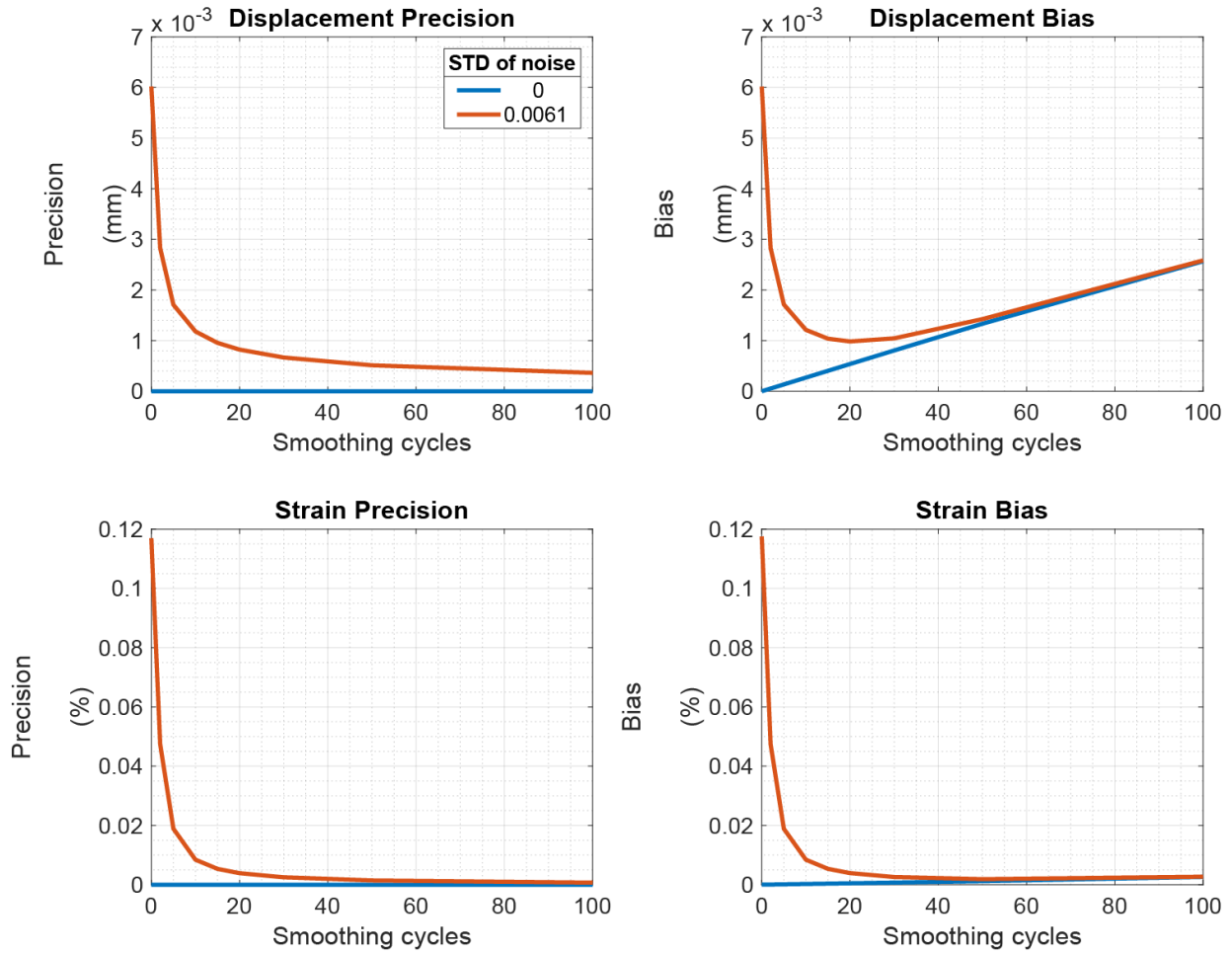


Figure A.8: Idealized Green-Lagrange strains for simulated data, for a 256x256 pixel image. Data shown are true strains.



**Figure A.9: Precision and bias of 64-pixel image.** Precision and bias strain were for displacements and strains using simulated displacement maps injected with Gaussian noise through 100 Monte Carlo iterations (Deva D. Chan, Toribio, & Neu). Standard deviation was 0mm for perfect strain maps (no added noise), and 0.0061mm for simulated scanner noise (Figure A.7). Minimum bias for the noisy image was observed at 10 cycles for displacements, but 20 cycles for strains.



**Figure A.10: Precision and bias of 128-pixel images. Minimum bias of the noisy image was observed at 20 cycles for displacements and 50 cycles for strains.**

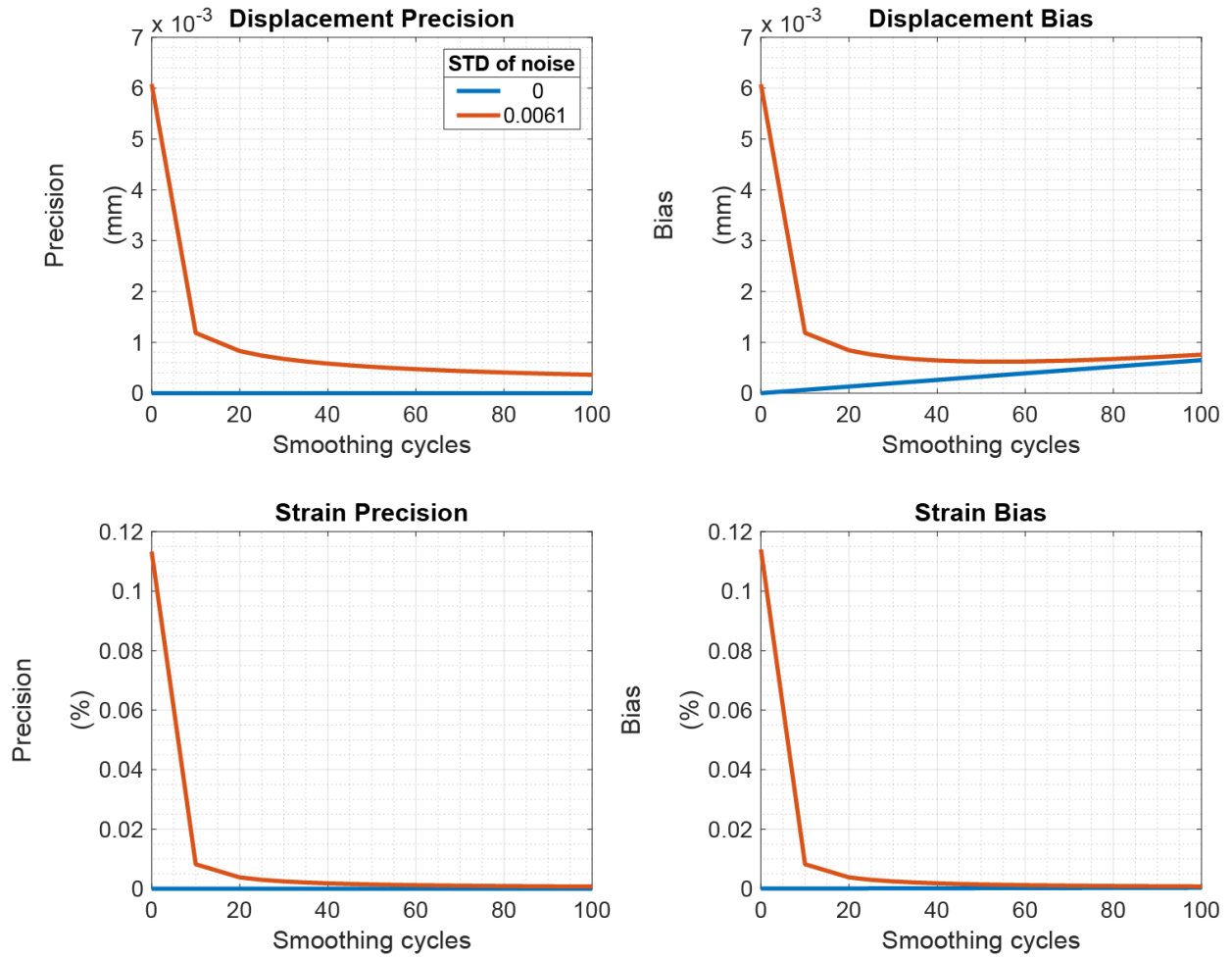
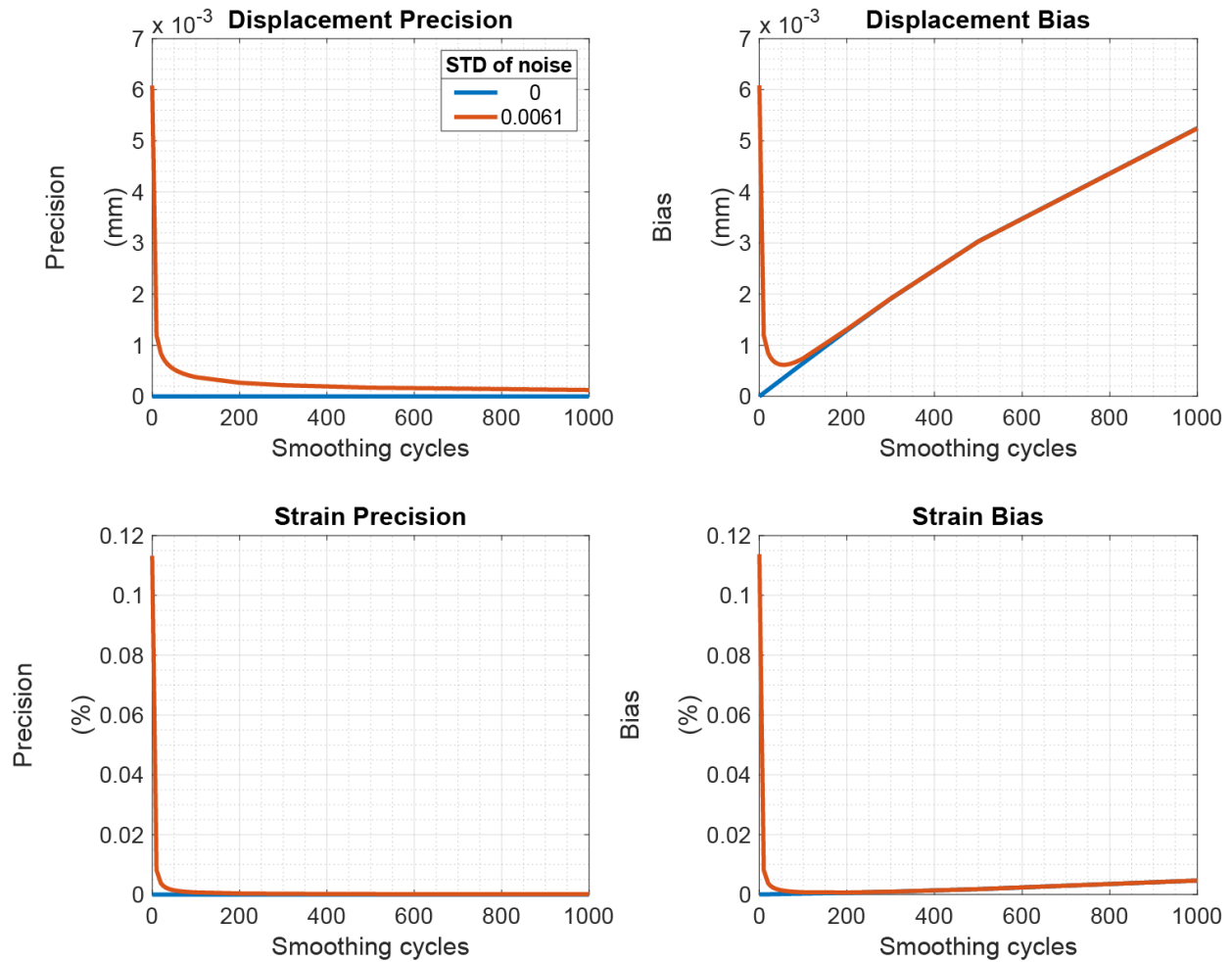


Figure A.11: Precision and bias of the 256-pixel images. Minimum displacement bias of the noisy image was at 50 cycles for displacements, with no clear minimum for strain.



**Figure A.12: Precision and bias of the 256-pixel images, extended up to 1000 smoothing cycles. Minimum bias of the noisy image was at 50 cycles for displacements, and 200 cycles for strains. 200 smoothing cycles will smooth the pixel impulse response across the entire ROI. While this minimizes overall strain, it may over smooth important features where local bias is more important. Thus, we limit smoothing for 256x256 images to 50 cycles.**

## **Appendix B Supplemental Files**

### **B.1 Permissions for Section 1.1**

This file contains license details and terms and conditions for the reproduction of material used in Section 1.1 of this dissertation.

**File name:** 20210223\_SS\_Shutterstock\_StandardLicense.pdf

**File type:** Portable Document Format (PDF)

**File size:** 60 KB

**Required application software:** Adobe Acrobat or any standard PDF viewer

**Special hardware requirements:** None

### **B.2 Permissions for Section 1.1.1**

This file contains license details and terms and conditions for the reproduction of material used in Section 1.1.1 of this dissertation.

**File name:** 20201125\_SS\_WoltersKluwer\_Permission.pdf

**File type:** Portable Document Format (PDF)

**File size:** 174 KB

**Required application software:** Adobe Acrobat or any standard PDF viewer

**Special hardware requirements:** None

### **B.3 Permissions for Section 1.2.1**

This file contains license details and terms and conditions for the reproduction of material used in Section 4.3 of this dissertation.

**File name:** 20210223\_SS\_Elsevier\_Permission.pdf

**File type:** Portable Document Format (PDF)

**File size:** 177 KB

**Required application software:** Adobe Acrobat or any standard PDF viewer

**Special hardware requirements:** None